博士論文

Optically induced modulation of insulator-metal transition materials in thin-films and plasmonic nanostructures

（金属・絶縁体転移マテリアルの薄膜及びプラズモニック構造の光誘起変調）

クラーク　ジョン　健志

Abstract

The demand for higher speed and larger volume telecommunications networks and higher speed computing devices is expected to increase significantly in coming years. The reliance of modern devices on electrical signals for all data processing and manipulation, however, represents a significant hurdle that must be overcome to meet this demand. Electrical signals suffer from resistive losses that make electrically based devices inefficient and demand large amounts of power. Furthermore, the operating frequency of electrical devices is limited by the excessive heat generated from the resistive losses, along with other fundamental phenomena affecting electrical signals, such as inductance and capacitance.

The replacement of electrical signals with optical signals, which have much lower propagation losses than electrical signals and don't suffer from inductance and capacitance related signal distortion, is the most promising way to meet the demands for more efficient and higher speed telecommunications and computing devices. Optical signals, transmitted by fibre optic cables, are already widely used for high-efficiency and high-speed data transmission in large scale telecommunications networks and server interconnects in data centres; however, the modulation and processing of these signals requires electro-optic devices, such as electro-optic modulators, photodetectors and photo-diodes. This adds significant inefficiency due to the frequent need to convert optical signals to electrical signals and back, and limits the maximum modulation speed that can be achieved.

For these reasons, the development of all-optical modulators that modulate optical signals using other optical signals is of great interest. All-optical modulators have been widely studied for many years, with silicon photonic based all-optic modulators with modulation frequencies nearing THz speeds having been demonstrated; however, the vast majority of devices studied thus far have relied on weak non-linear phenomena. This reliance on weak non-linear phenomena has necessitated large microscale sizes and has resulted in modulation depths that are insufficient for use as all-optical switches in all-optical computers. For all-optical computing and all-optical telecommunications devices to be a viable alternative to electrical computing and electro-optical devices, all-optical modulators with nanoscale sizes and strong modulation depths must be developed.

Insulator-metal transition materials, such as VO_2 and NbO_2, are of particular interest for the development of all-optical modulators. Insulator-metal transition materials undergo a

transition from an insulating state to a metallic state upon reaching a specific insulator-metal transition temperature, and as a result of the transition their optical properties change drastically. In the case of VO_2 this has been used to develop nanoscale thermo-optic and electro-optic modulators with large modulation depths. When it was demonstrated that the insulator-metal transition of VO_2 can be induced through optical excitation, the potential for VO_2 to be used in an all-optical modulator was realized; however, thus far, all-optical modulators using VO_2 have been limited to low MHz speeds and the insulator-metal transition was induced photo-thermally. Although the initial dynamics of the photo-induced insulator-metal transition of VO_2 has been widely studied, the recovery of VO_2 from this photo-induced state and whether insulator-metal transition materials can recover at sub-ns speeds to achieve ultrafast all-optical modulation has yet to be studied.

In this thesis, the optically induced modulation of two insulator-metal transition materials, VO_2 and NbO_2 is studied, with a focus on the dynamics of the recovery from the photo-induced state after excitation by a femtosecond laser pulse. The effect of nano-structuring on the recovery dynamics is then investigated, followed by a demonstration of strong modulation and sub-ns recovery using a plasmonic nanohole array structure. Finally, a waveguide-integrated all-optical modulator using VO_2 as an active material with a nanoscale size, extremely high modulation extinction ratio and low switching threshold is designed to demonstrate the potential of these insulator-metal transition materials for all-optical modulation in integrated photonic devices.

In the initial study of the recovery dynamics of the optically induced modulation of VO_2 and NbO_2 thin-films, three main conclusions are drawn. First, the optically induced modulations of VO_2 and NbO_2 at low pump fluences are found, contrary to the consensus in the literature, to be a purely linear process, unrelated to the insulator-metal transition and with recovery dynamics determined by the thermal dissipation of the thin-films. In a mid-fluence region, evidence of the recently discovered monoclinic metal state of VO_2 is found, and for the first time, it is demonstrated that VO_2 can recover from this monoclinic metal on an ultrafast, sub-ns timescale. This represents the first demonstration of the full recovery of VO_2 on a sub-ns timescale after optical excitation, and the first evidence of a non-thermal recovery process for the monoclinic metal state of VO_2.

In order to determine the maximum potential modulation speed of a VO_2 based all-optical modulator, the effect of film thickness and nano-structuring on the recovery dynamics

of VO_2 and NbO_2 are studied. It is found that the monoclinic metal state of VO_2 has a minimum lifetime of 10s of ps and that thermal dissipation does not represent a bottleneck in the recovery of VO_2 to its equilibrium optical properties after undergoing an optically induced insulator-metal transition. Through the use of ultra-thin thin-films, full recovery of VO_2 in as little as 100 ps and NbO_2 in as little as 200 ps after optical excitation was demonstrated and full recovery of VO_2 after a photo-induced insulator-metal transition to the monoclinic metal phase in as little as 600 ps was demonstrated.

Strong modulation with a low pump fluence and fast recovery is demonstrated using a Au/VO_2 plasmonic nanohole array. The plasmonic nanohole array allows for a small volume of VO_2 to enable ultrafast recovery of the VO_2 for high-speed modulation while maintaining a strong modulation. The periodic plasmonic structure is also designed to concentrate the pump light that induces the insulator-metal transition in VO_2. The structure is fabricated using nanofabrication techniques and then the optically induced modulation of the structure is characterized. A reduced threshold, compared to a VO_2 thin-film, for the monoclinic metal state is found and a strong modulation intensity is obtained, despite the low volume fraction of VO_2 in the structure. In the mid-fluence region, the structure was found to have a strong modulation after undergoing an insulator-metal transition to the monoclinic metal state while recovering on a sub-ns timescale, representing the first demonstration of a VO_2 based all-optical modulator with sub-ns recovery.

To demonstrate the potential of all-optical modulators using insulator-metal transition materials, a waveguide-integrated all-optical modulator incorporating VO_2 with a nanoscale size is designed. A sub-wavelength Au/VO_2 nanostructure is used to take advantage of the concentrating effects of the plasmonic modes supported by the Au in order to enable low threshold switching of the all-optical modulator. The Au/VO_2 nanostructure is further found to behave as an effective medium, whose dimensions can be optimized to enhance the transmittance of the device when VO_2 is in its insulating state and minimize the transmittance of the device when VO_2 is in its metallic state, thus achieving strong modulation while maintaining a nanoscale size. A 550 nm long, 320 nm wide and 300 nm tall all-optical modulator with an extinction ratio of 26.85 dB/μm, the highest yet reported for a VO_2 based optical modulator, is designed.

The demonstration of the optically induced modulation of insulator-metal transition materials with full recovery of the modulation in as little as 600 ps, and the VO_2 based

nanoscale all-optical modulator with extremely strong modulations detailed in this thesis shows the potential for insulator-metal transition materials to enable high-speed integrated all-optical modulators. The discovery of a ps-scale bottleneck in the recovery of the optically induced monoclinic metal state precludes the possibility of THz speed all-optical modulators as had been hoped for all-optical computing; however, GHz speeds all-optical modulators have the potential to revolutionize optical signal processing in telecommunications networks. Furthermore, the ability to control the length of the induced modulation using pump fluence is a unique feature unseen in electrical modulator devices that may see practical use in new burgeoning fields such as neuromorphic computing and memristors.

Acknowledgements

I would like to take this opportunity to give my heartfelt thanks to all those who have supported me through my academic studies, guided me in my academic career and motivated me to pursue my goals in life.

First and foremost, I would like to thank my beautiful and loving wife, Ayumi Clark. Without her, I would never have been able to complete my Ph.D. studies. After a long day doing experiments in the lab, I could always look forward to coming home to a welcoming smile to help me forget the stresses and worries of my research. I could never hope for a better life partner, and I want to sincerely thank my wife for supporting me and cheering me on over the last three years.

I would also like to thank my father-in-law Mr. Shigeki Yamamoto, my mother-in-law Mrs. Keiko Yamamoto and my brother-in-law Mr. Yuki Yamamoto. Since before I even set foot in Japan and before I joined their family, Mr. and Mrs. Yamamoto have acted as my surrogate parents in Japan. From the bottom of my heart, I would like to thank them sincerely for always making me feel at home and at ease here in Japan. I would also like to thank my brother-in-law Yuki for his invaluable help during my job search in the final year of my studies, without which I don't think I would have been able to stay in Japan to work after graduation.

Of course, I can't forget my family, who has always supported me and pushed me to achieve greater and greater feats throughout my entire life. I would like to thank my father James Hugh Clark. Without my father's financial and moral support, studying overseas could not have been possible. To my mother, Glenda Lorraine Farstad, I would like to say thank you for always believing in me and always having a smile on your face every day. During the more trying times of my studies, speaking to you has always lifted my heart back up and given me the motivation to keep on working. The academic and career advice from my elder brother, James Michio Hjalmar Clark, has been invaluable in my studies. Throughout my entire life, Michio has helped guide me with his experience, and my academic studies were no exception. I would also like to acknowledge my younger brother William Tomio Duncan Clark, who has always been willing to chat about just about anything when I need a break from thinking about research.

My Ph.D. studies could never have been possible without the support, guidance and kindness of my supervisor, Prof. Jean Jacques Delaunay. I would like to thank Prof. Delaunay

for allowing me to join his wonderful research group, where I was able to conduct exciting research in a welcoming and friendly environment. I would also like to thank Prof. Delaunay for the academic funding he provided me to conduct my research.

In addition to the support from my supervisor, I would also like to acknowledge the many other individuals at the University of Tokyo that have made my studies and research possible. I would like to acknowledge the guidance of Prof. Hiroaki Matsui, who acted very much as a secondary supervisor to me throughout my studies, and whose invaluable knowledge of materials science made my research on insulator-metal transition materials possible. The support provided by Dr. Makoto Fujiwara and Dr. Eric Lebrasseur from the University of Tokyo Nanofab Platform has also been vital to my research. I would also like to give a special thanks to Prof. Ya-Lun Ho, who has not only been an excellent academic colleague always eager to hear my ideas and discuss difficulties in my research with me, but who has also helped me in many aspects of adjusting to life in Japan. I would also like to thank Dr. Li-Chung Huang, Dr. Jun Yu and Mr. Zhiyu Wang for their assistance in learning how to use various pieces of experimental equipment during my studies.

I would also like to thank the University of Tokyo International Multidisciplinary Engineering program for providing me with the opportunity to study at the University of Tokyo in an English language program. In particular, I would like to thank Ms. Yukimi Umeda, Ms. Yoshie Minigeshi and Ms. Rika Sakai from the IME program for their help before and throughout my studies.

Finally, I would like to thank the institutions that have financially supported by studies. For the SEUT Grant for International Students that supported me during the first two years of my studies, I would like to thank the School of Engineering at the University of Tokyo. Lastly, I would like to thank the Japan Society for the Promotion of Science for providing me with a JSPS Special Researchers Grant to support me during the final year of my Ph.D., and which allowed me to attend an international conference at the end of my studies.

Contents

List of Figures

List of Tables

List of Acronyms and Symbols

CMOS	complementary metal-oxide semiconductor
CPT	crystal phase transition
IMT	insulator-metal transition
PIC	photonic integrated circuits
PLD	pulsed laser deposition
XPS	x-ray photoelectron spectroscopy
XRD	x-ray diffraction
XRR	x-ray reflectance
T_{IMT}	insulator-metal transition temperature
c	speed of light
E	energy
E_G	band gap energy
E_{ph}	photon energy
f	lens focal length
$\hbar$	reduced Planck's constant
I_{probe}	light intensity
k_B	Boltzmann constant
m^*	effective mass
m_e^*	electron effective mass
m_h^*	hole effective mass
N	photo-excited carrier concentration
n	complex refractive index
n'	real part of refractive index
n''	imaginary part of refractive index
N_0	intrinsic carrier concentration
N_{passes}	number of delay line passes
q_e	elementary electron charge
R	reflectance
T	transmittance
ΔT	change in transmittance
ΔR	change in reflectance

A	absorptance
α	absorption coefficient
γ	damping coefficient
Δd_{delay}	spatial pump-probe delay
Δt_{delay}	temporal pump-probe delay
$\Delta Temp$	change in temperature
ϵ	permittivity
ϵ_0	vacuum permittivity
ϵ_r	relative permittivity
ϵ_s	static relative permittivity
Θ	phonon temperature
λ	wavelength
σ	standard deviation
Φ	laser fluence
ω	radial frequency
ω_0	oscillator resonant frequency
ω_p	plasma frequency

Chapter 1 : Introduction

The digital revolution that made the modern world was supported by two key technologies, computing and telecommunications. With extremely powerful computational devices that can perform complex logical operations in fractions of a second, we have enabled a whole host of electronic devices that have made our lives easier, more enjoyable, more efficient and safer. The advent of vast telecommunication networks has also made our lives more interconnected by making it possible to communicate with people on the other side of the globe with next to no delay. As these technologies have become more and more widespread and essential to our everyday lives, however, the demand on them has increased drastically.

Despite the constant exponential growth in the processing power of computing devices that has been seen each year, as captured by the well-known Moore's Law, the demand for more powerful computing devices has never ceased. Every year new simulation techniques, computer games, optimization algorithms and many other software technologies demand more powerful computing devices. As computationally intensive AI technologies currently being developed are implemented in next generation devices, this demand for more powerful computing devices is only expected to continue to grow.

For many years, the demand for faster and more powerful computing devices was met as the number of transistors in processors and their frequency of operation increased exponentially each year, as described by Moore's Law [1]. In recent years, however, this exponential increase has begun to trail off. The clock frequency of processors in computing devices has already hit a limit of several GHz due to thermal limitations [1]. Although semiconductor transistors can theoretically, and have been shown experimentally, to be able to operate at frequencies on the order of hundreds of GHz [2], in the processors of computing devices, thermal limitations prevent transistors from being operated at high frequencies in high density devices such as processors [3]. As electrical signals propagate through transistor devices, they lose energy due to resistive losses, and this energy is converted to heat which has the potential to damage the processor if it becomes excessive. In devices with a low transistor density, this heat can be sufficiently dissipated within one period even for operation frequencies on the order of hundreds of GHz; however, when the density of transistors increases drastically as is the case for processors, the maximum achievable frequency is on the order of several GHz. The overall performance of computing devices continued to improve despite the thermal limitation on their clock frequencies, because the density of transistors in processors continued to increase; however, with current CMOS transistor devices approaching the theoretical limit

of their minimum size, further improvements in computing device performance will require new approaches in the coming years.

In addition to the limitation on the computing power of transistor-based computing devices, the power consumed by them is a major problem that must be overcome. Along with the steadily increasing processor performance seen year-by-year, the power consumed by processors, and computing devices in general has increased steadily. The percentage of the power generated in the world consumed by computing devices has already been shown to be as high as 2.9% [4]. If we are to meet the growing demand, not only for more powerful computing devices and computing power in more devices, but also the world's growing demand for energy, more energy efficient computing devices must be developed.

In the field of telecommunications as well, demand is expected to grow. Along with the AI technologies mentioned previously, which rely on large amounts of data to learn, upcoming IoT technologies will also demand access to large amounts of bandwidth in our telecommunications networks as they transmit and receive information from large data centres [5]. Furthermore, data centres are comprised of large servers that consume vast amounts of power as a result of the inefficiencies of transistor-based devices, as discussed above.

Large range telecommunications rely on optical signals transmitted through fibre optic cables to transmit data at the speed of light with low loss and high bandwidth [6]. Advances in this field, such as wavelength division multiplexing and coherent optics for signal processing have helped meet the growing demand, and new technologies such as multicore optical fibres and all-optical signal amplification promise to further improve bandwidth and energy efficiency of telecommunications systems. However, the reliance on electro-optic modulators to modulate the optical signals and encode data into them, places limitations on their ultimate speed and efficiency. Signal processing in particular requires the conversion of the optical signals to electrical signals so that they can be processed in electrical circuits using transistor devices and then their reconversion back to optical signals. This creates a time delay that limits the speed of telecommunications networks and also increases the energy losses of these systems [3]. Another consequence of electrical signals being required for the modulation of optical signals is that when noise builds up in signals being transmitted over long distances, such as in undersea fibre optic cables, the signal regeneration must be performed electrically [7]. This necessitates electrical power being transmitted along with the optical signals in undersea cables and due to the large losses seen when electrical power is transmitted over long distances,

this results in a drastic increase in the power consumption of long-distance telecommunications networks [7].

In order to overcome the limitations of modern computing devices and telecommunications systems, a new class of devices must be developed, and all-optical devices are a promising avenue. As already mentioned in the discussion of modern telecommunications networks, optical signals can propagate long distances with minimal losses in optical fibres and waveguides. This not only results in all-optical devices having high energy efficiency, but also allows optical signals to be modulated with high frequencies unlike electrical signals.

In any device that deals with data transmission or processing, whether a computing device or a telecommunications device, an essential functionality is the ability to modulate signals. In electrical devices, an electrical modulator, which usually takes the form of a semiconductor transistor is used. In optical telecommunications devices, optical signals are modulated by means of electro-optic modulators stimulated by electrical signals. In the case of all-optical devices, all-optical modulators are necessary.

1.1 All-Optical Modulators

All-optical modulators are devices that modulate an optical signal based on a stimulus from another optical signal [8]. This modulation can take a variety of forms. For example, amplitude modulation can be performed, where the intensity of the optical signal is modulated. Alternatively, the phase of a coherent optical signal can be modulated, or even the frequency of the optical signal can be modulated. In any of these cases, a control optical signal, or pump signal, must interact with a device and modify its properties such that it induces a modulation in a probe signal.

The ability to directly modulate optical signals using other optical signals has significant advantages compared to electrical based transistors and electro-optic modulators. One of the major advantages of all-optical modulators is the bosonic nature of photons, the quantum particle of light [3]. Unlike fermions, of which electrons are one example, bosons do not interact with each other directly and can occupy the same quantum state as each other [9]. This has several important consequences. The first is that when an optical signal propagates in a material, the loss and degradation of the signal is entirely determined by the interaction of the signal with the material and can be made nearly non-existent when the signal propagate in a non-absorbing dielectric medium, allowing them to propagate large distances with minimal need for regeneration or amplification [3]. The lack of loss further means that very little heat

is generated as they propagate through a medium, making them highly energy-efficient. Another consequence of the lack of interaction is that multiple optical signals carrying different information can propagate through the same medium without altering each other [10]. This is usually performed by encoding information on signals with different wavelengths of light and then propagating them through the same medium – commonly known as wavelength division multiplexing [11]. It is also possible to use the different modes of an optical waveguide/fibre to encode different signals, known as mode-division multiplexing, but this suffers from issues related to dispersion and is not used in practical devices [11]. This gives all-optical modulators the potential to do parallel processing where multiple signals are modulated at the same time without the need for additional power or space.

1.1.1 Non-Linear Optical Responses

Although the non-interacting nature of photons makes all-optical modulators highly promising, it also has a significant downside, and that is that it is very difficult to make one optical signal influence another, which is essential for an optical signal to actually modulate another. Since the photons cannot interact directly, an interaction with a material must be used to mediate the modulation of one signal by another. Although in a classical picture of electrodynamics light matter interactions are purely linear, in reality, when light passes through a medium, the electromagnetic fields of the light interact with the structure of the material, and this results in small disturbances in the material that alters how light propagates through it. This is described by the non-linear response of the material, and constitutes an entire sub-field of photonics, non-linear optics [12].

Non-linear responses are classified into two types, parametric and non-parametric non-linearities. Parametric non-linearities are a result of the deviation of the true band structure of materials from the idealized parabolic structure, and are instantaneous phenomena in which the quantum state of the material is unchanged. Non-parametric non-linearities on the other hand are a result of the material changing its quantum state in response to the light passing through it, where the new quantum state has different optical properties than the original state [13].

The most common example of a parametric non-linearity used in all-optical modulators is the optical Kerr effect. In a simple model of light-matter interactions, the polarization induced in a material by incident light is modeled by a simple harmonic oscillator, where mobile electrons are displaced from a stationary lattice of nuclei. In this model, the potential energy of the electrons is described by a parabolic function of displacement, and this yields a

linear optical response where the optical properties of the material are independent of the intensity of the incident light [12]. For low intensity light, where the electromagnetic fields are weak, and the electrons are not significantly displaced from their equilibrium positions, this is accurate; however, at high light intensities, the deviation of the potential energy surface from this idealized parabolic shape becomes important, and results in the refractive index changing with changing light intensity [13]. This phenomenon is known as the optical Kerr effect, and the changing refractive index of the material will not only affect the propagation of the light that induces the refractive index change itself, but also any other light passing through the material at the same time, enabling the propagation of one signal to be altered by another high-intensity signal [8].

Non-parametric non-linearities happen when the material that light is passing through undergoes a change that alters its optical properties. This change is caused by the material absorbing energy from the light passing through it, whether through the absorption of a photon and the excitation of an electron in an interband or intraband transition, from the excitation of phonons, the scattering of free-electrons oscillating with the electric field of the light, or any other non-conservative process. These processes will cause changes in the excited material, such as changes in its electronic band structure, free-carrier concentration and temperatures and thus alter its optical properties [14]. Unlike parametric non-linearities, non-parametric non-linearities are not instantaneous and the changes induced by the incident light have a recovery time associated with how long it takes the material to relax back to its equilibrium state [13].

Both parametric and non-parametric non-linearities are in general very weak, and therefore, the change in the refractive index induced by an optical signal is small [13].

1.1.1 Fibre Optic All-optic Modulators

With the advent of fibre optic telecommunications networks in the late 1980s and 1990s, the telecommunications industry was revolutionized, enabling high-speed and high-fidelity communication between locations vastly separated on the globe. The use of low-loss optical signals for data transmission meant that much larger amounts of data could be transmitted across the world at higher speeds and with much lower power demands. However, the need for electro-optic modulators to encode information into optical signals and route them through large interconnected telecommunications networks was recognized early on as a major limitation to their potential. This drove researches in the telecommunications industry very

early on to investigate fibre-integrated all-optical modulators that could be integrated into their new fibre optic telecommunications networks [3].

The first all-optical modulators were demonstrated using erbium doped fibre optic cables. Erbium doped fibres have a small parametric non-linearity as a result of the optical Kerr-effect, meaning that their refractive index will change by an amount proportional to the intensity of an optical signal that is passed through them. This will in turn alter the propagation constant of the optical signal and result in the phase accumulated by the optical signal after propagation for a certain distance being dependent on the intensity of the signal. By incorporating these fibres into interferometric devices, an intensity dependent response that can be used for switching or guiding the optical signal can be achieved [3].

One such interferometric device is a fibre Mach-Zender interferometer, as pictured in Figure 1.1 below. In a fibre optic Mach-Zender interferometer, an optical signal propagating in one fibre is split into two separate fibres by means of a coupler. The optical signal then propagates in the two separate fibres, accumulating a phase. The two fibres are then recombined into one optical path by means of another fibre coupler before separating again. At the second coupler, the optical signals in the two fibres will interfere with each other. The intensity of the signal out-coupled from the two output fibres will depend on the relative phase of the two optical signals. When a non-linear optical fibre is used, the relative phase of the two optical signals will depend on the intensity of the original signal, and this allows one to control which output fibre the optical signal is coupled to simply by controlling its intensity [3].

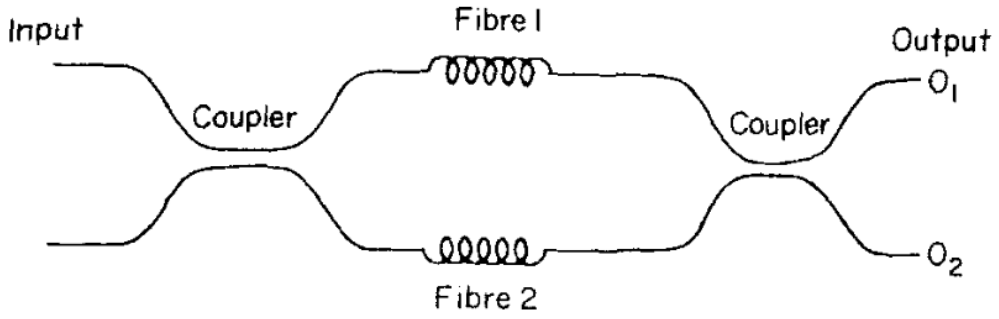

Figure 1.1: Schematic of a fibre optic Mach-Zender interferometer. Depending on the phase difference of the light propagating through Fibre 1 and Fibre 2 at the second coupler, the light will either be coupled to output O1 or O2. Reproduced from [3].

Although all-optical modulation was possible with fiber optic cable based all-optical modulators, the very small non-linearities exhibited by erbium doped fibres made them unsuitable for practical devices. Firstly, the weak non-linearity meant that the devices had to be very large in size, using long segments of fibre optic cable in order to achieve appreciable

changes in the phase and resonance of the optical signals. This caused further issues with practicality, as the large size also made them extremely sensitive to environmental disturbances, such as temperature fluctuations and vibrations.

1.1.2 All-optical Modulators in Photonic Integrated Circuits

With the advent of integrated photonics and microfabrication, and in particular silicon photonics, the idea of using these new technologies to develop photonic analogues of electronic integrated circuits began to grow in popularity, and it wasn't long before people began developing all-optical modulators in photonic integrated circuits (PIC). Photonic integrated circuits are optical circuits that guide light on the surface of semiconductor or dielectric chips, in the same way that optical fibres confine light in the core of an optical fibre. The amplification, modulation, generation and detection of optical signals can all be performed on these millimetre scale PICs, allowing for far more compact devices than are possible with fibre optics [8].

In the last three decades, a large number of different all-optical modulator designs have been proposed and demonstrated using a vast array of different integrated photonics technologies, such as integrated waveguide interferometers [6], waveguide ring resonators [15] and even photonic crystal defects [16].

Similar to the all-optical modulators demonstrated using fibre optics, several interferometers based all-optical modulators have been demonstrated in PICs. These devices rely on the parametric non-linear response of the waveguide material to create a difference in phase between the two paths of the interferometers and in doing so achieve an intensity dependent transmittance. Because of the large confinement as compared to fibre optic devices, the intensity of the optical signal is larger, making the non-linear response of waveguide interferometers stronger and allowing for smaller device sizes relative to fibre optic interferometers. However, in order to accumulate a sufficient phase difference for an intensity dependent transmittance to be achieved, long arm lengths in the interferometers are still needed, and device sizes are still on the order of several mm [6].

In order to reduce the size of all-optical modulators, researches began to investigate resonant structures, such as ring resonators and photonic crystal defects. Resonant structures trap specific modes of light, and this allows them to increase the non-linear response experienced by an optical signal trapped in them.

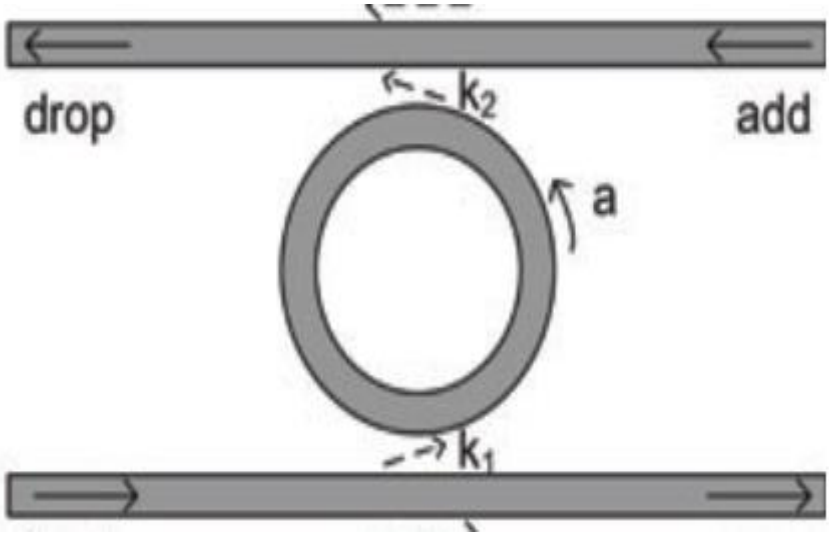

Figure 1.2: Operating principle of a photonic ring resonator. Light passing through the lower waveguide can couple to the ring resonator if it satisfies the resonance condition of the resonator, otherwise it passes by the waveguide. A second waveguide placed on the other side of the ring resonator can capture the light coupled to the resonator. Modified from [17].

The most common resonant structure used in all-optical modulators is the ring resonator. Ring resonators are simply photonic waveguides formed into a continuous ring shape, as illustrated in Figure 1.2. Because of the continuous nature of the ring, light completing one round trip around the ring will interfere with itself, and this results in the ring only supporting specific wavelengths of light for which the optical path length of the ring corresponds to a multiple of the wavelength of the light. When a waveguide is in close proximity to a ring resonator, light propagating through the waveguide whose wavelength satisfies the resonance condition of the ring resonator will couple to the ring resonator and be trapped temporarily in the resonator [17]. Several different varieties of all-optical modulators have been demonstrated using ring resonators. In one type, a second waveguide on the other side of the resonator can out-couple light coupled to the resonator. This causes the transmittance of an optical signal passing through the first waveguide to be zero when the ring resonator's resonance condition is satisfied. By relying on the intrinsic non-linearity of the waveguide material or by coating a portion of the ring resonator with a material that has a strong non-linearity, the resonant condition of the ring resonator can be modified using a high intensity signal and the transmittance of the first waveguide can be modified [18]. Another class of ring-resonator all-optical modulator relies on coating the ring resonator with an absorbing material. An optical signal coupled to the ring resonator resonance will be absorbed and show a very low transmittance [15]. Although the performance of ring resonator based all-optical modulators is promising, the quality factor of ring resonators is directly proportional to their radius of curvature, and therefore, even the smallest devices have sizes of 10s of μm.

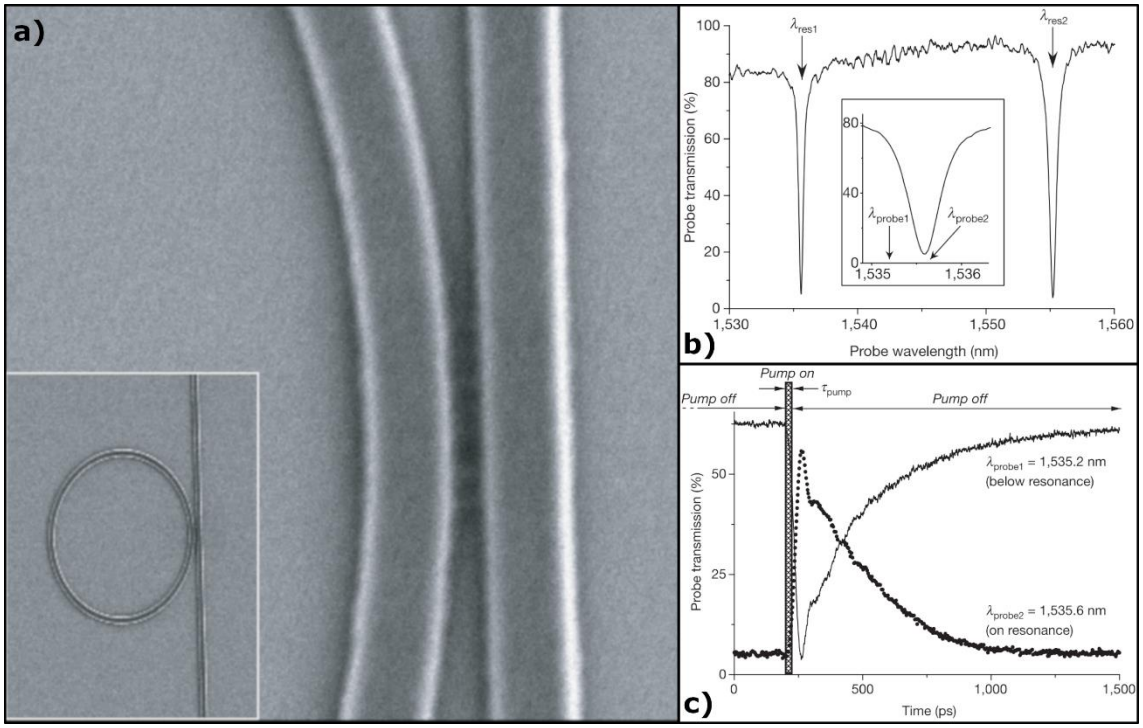

Figure 1.3: Ring resonator based all-optical modulator. a) SEM image of the coupling region between a waveguide and the ring resonator (inset) image of the full ring resonator and coupled waveguide. b) The initial transmittance of the modulator plotted against wavelength showing clear resonances where light is coupled to the ring resonator and absorbed. c) time-resolved change in transmittance through the waveguide for on-resonance and off-resonance wavelengths after an excitation by an ultrashort laser pulse that alters the resonance of the ring resonator. Modified from [15].

Another photonic architecture that was explored for the purpose of all-optical modulators is photonic crystal defects. Photonic crystals are structures with a periodic variation in their refractive index. By virtue of this periodicity and the interference between the reflected light from the different refractive index interfaces in the crystal, light with a wavelength in a range known as the stop band is incapable of propagating through the crystal. Photonic crystals can exist in 1, 2 and 3 dimensions. When the periodicity of the crystal is disrupted, a defect is formed. Within the defect, highly confined modes exist for specific wavelengths in the stop band. The introduction of non-linear materials into photonic crystal defects has been used to enable the control of the defect modes through a high intensity control signal or an optical signal itself [8,16].

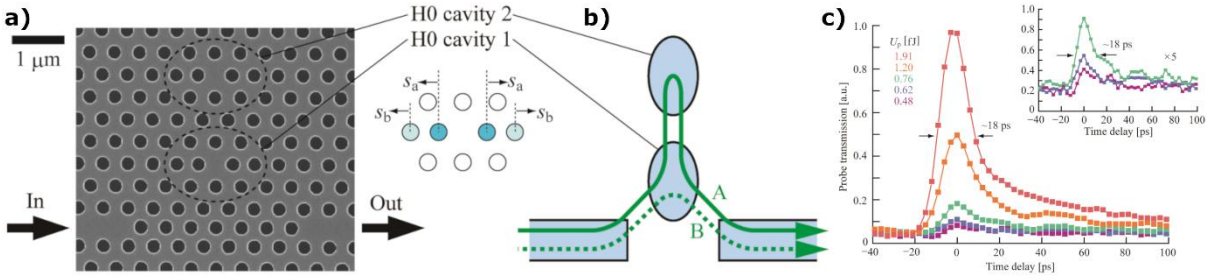

Figure 1.4: Photonic crystal defect based all-optical modulator. a) SEM image of the modulator. Photonic crystal waveguides at the bottom of the figure are used as the input and output waveguides. Two photonic crystal defects in the centre and top of the figure control the transmittance. b) Schematic of the components of the modulator showing the input waveguide, output waveguide and two cavities formed by the photonic crystal defects. c) Modulation of the transmittance from the input waveguide to the output waveguide after excitation of cavity 2 by an ultrafast laser pulse. Modified from [16].

1.1.3 All-optical Modulators and Novel Materials

Due to the limitations of traditional materials used in all-optical modulators, interest has recently grown in more exotic materials with unique properties and strong non-linear responses.

Graphene is one such material that has attracted interest for all-optical modulation. Graphene has the unique property that it has a nearly constant and strong absorption band over the entire near-IR and visible region, with the absorption being approximately 2.3% per monolayer of graphene. Because of this strong absorption, graphene exhibits a strong non-parametric non-linearity from band-filling – also known as Pauli blocking. When light with a short wavelength is absorbed by a layer of graphene, electrons are excited from the valence band of the graphene to the conduction band of the graphene. Shortly after, they relax to the bottom of the conduction band and fill the states there. This prevents longer wavelengths of light from exciting electrons, as there are no electrons in the valence band to excite, or the states they would be excited to are already filled. As a result, the absorption at longer wavelengths decreases. Using this phenomenon, it is possible to modulate the transmittance of light at a longer wavelength using a shorter wavelength pulse. Using this phenomenon, the modulation of a 1.55 μm laser signal by a 789 nm pump laser signal with a 2.2 ps recovery time has been shown in a graphene coated fibre optic cable configuration [19]. Despite this promising result, the difficulties associated with the nanofabrication of graphene makes it unlikely that it can be applied to make nanoscale all-optical modulators.

Another material class that has recently been explored for all-optical modulators is epsilon-near-zero materials. Epsilon-near-zero materials are materials whose real and imaginary refractive index are both very close to zero over a certain wavelength range.

Generally this behaviour is seen in transparent conducing materials in the near-IR region, as they do not have any interband transitions within this region, leading to a low imaginary permittivity, but they have a large concentration of free charge carries that give them a Drude-Lorentz response with a plasma frequency in the near-IR [20]. The Drude-Lorentz model, which can be used to model the effect free charge carriers have on the permittivity of a material is described by [12],

$$\epsilon(\omega) = 1 - \frac{{\omega_p}^2}{\omega^2 + i\omega\gamma_j}$$

where the plasma frequency, ω_p, is defined by [12],

$$\omega_p = \frac{N{q_e}^2}{\epsilon_0 m^*}$$

Here, N is the density of free charge carriers, q_e is the electron charge, ϵ_0 is the vacuum permittivity, m^* is the effective mass of the free carriers, and γ is the damping frequency that describes resistive loss. As can be seen, the real part of the permittivity approaches zero as the frequency of light reaches the plasma frequency, and for frequencies lower than the plasma frequency, it becomes negative. When a material has several dielectric responses, the total permittivity is described by [12],

$$\epsilon(\omega) = 1 + \sum_j \frac{{\omega_{pj}}^2}{{\omega_j}^2 - \omega^2 - i\omega\gamma_j}$$

where ω_{pj} and γ_j corresponds to the plasma frequency and damping frequency of an individual response. In this equation, ω_j is the resonant frequency of the response and has a value of 0 for a Drude-Lorentz response. From the above equation it is clear that for a material lacking absorption resonances in the near-IR but with free charge carriers, there will a certain range over which the real and imaginary components of the permittivity are both small. In metals the concentration of free charge carriers cannot be significantly altered by photo-excitation, but for transparent conductors, which are semiconductors, photo-excitation by light with an energy above the bandgap of the semiconductor can increase the free charge carrier concentration and alter the position of the epsilon-near-zero (ENZ) region.

This is an example of a non-linearity caused by a photo-induced change in the free carrier concentration, and the observed change in the refractive index is not particularly large; however, near the ENZ region, the initial refractive index is very small and as such the relative change in the refractive index observed in this region is very large. This has been used to show

large changes in the reflectance and transmittance of a slab of an ENZ material [21]. Unfortunately, there has yet to be a demonstration of such an effect in a waveguide-integrated device.

1.2 Insulator-Metal Transition Materials

All of the all-optical modulators discussed above suffer from one key limitation; because the non-linear response of most materials is weak and the refractive index of a material can only be slightly perturbed by light, long interaction lengths or large resonant structures are needed to achieve appreciable modulations in an optical signal with another optical signal. If all-optical modulators are to be used in making the next generation of all-optical computing and telecommunications devices, however, they must be competitive with electronic and electro-optic devices, and this necessitates that they be reduced to nanoscale sizes comparable to electronic semiconductor devices. For this to be possible, materials with a strong non-linear response that can undergo a large change in their optical properties must be used. One class of materials that exhibits this property is insulator-metal transition materials (IMT).

IMT materials are materials that exhibit an insulating behaviour at low temperatures, but when heated above a certain critical temperature, known as the insulator-metal transition temperature (T_{IMT}), they become metallic in nature [22]. Below the T_{IMT}, the fermi level of IMT materials sits within a small semiconductor bandgap or a large insulator bandgap depending on the material. When their temperature is raised above T_{IMT}, the band gap collapses and the band structure becomes that of a metallic conductor, with the fermi level lying within the conduction band. As expected, this transition from a semiconductor/insulator band structure a metallic band structure results in a large change in the resistivity of the material as the number of free charge carriers drastically increases. In addition to this direct change in the electrical properties of the material, the large increase in the number of free carriers also causes a large change in the optical properties of the material. With the high free charge carrier concentration, the material begins to exhibit a metallic Drude optical response. Depending on the exact carrier concentration, the Drude response will be significant over a different frequency range; however, for most materials the plasma frequency lies in the visible range, and as such, for IR and longer wavelengths the material shows metallic behaviour with a high reflectance and absorption coefficient [23].

IMT materials were first discovered during early theoretical studies of the electronic band structure of semiconductors and metals. It was found that for many transition metal oxides

a simple band structure model where electrons are non-interacting predicted the materials would have partially filled conduction bands and would behave as conducting metals, but in experiment they were found to be insulating [23]. Furthermore, the materials were found to transition from this insulating behaviour to the theoretically predicted conducting behaviour above a critical transition temperature. To properly predict the behaviour of these materials, the electron-electron interactions within the materials had to also be accounted for [22].

The exact mechanism of the insulator-metal transitions observed in strongly-correlated transition metal oxide materials has been widely debated for many years, but the general consensus is that they follow either one of, or a combination of, a Mott transition and a Peierls transition [23]. In a Mott transition, the insulating behaviour arises due to the coulomb repulsion of electrons from one another. In a material with a half filled valence band, the repulsion of electrons in an individual atom results in the splitting of the band into an upper and a lower band when the atomic spacing is above a certain value. If the carrier concentration is increased though, the electrons will begin to screen the nuclei of the material, and this will result in a collapse of the bandgap [24]. A Peierls transition on the other hand occurs because of the instability of certain crystal structures. For some crystal structures, individual lattice ions will pair to form dimers in a process that lowers the overall energy of the valence electrons. This pairing doubles the lattice constant of the crystal and opens a bandgap between a fully occupied lattice band and unoccupied conduction band. At a critical lattice temperature, excited electrons screen the lattice charge, and the pairing disappears. The structure therefore returns to its simple structure and the crystal becomes metallic [24]. For both of these transition types, the IMT is often accompanied by a change in the crystal structure as well, which is commonly referred to as a crystal phase transition (CPT).

Regardless of the mechanism of the transition, there are a wide variety of materials that exhibit an IMT. A large selection of such materials is shown in Figure 1.5, where the relative change in resistivity of the materials is plotted against the temperature at which they undergo an IMT. As the IMTs are first order transitions, they have a certain latent heat associated with them, and as such show a hysteresis when heated above and below T_{IMT}. The width of this hysteresis is shown by the horizontal bars in Figure 1.5. From Figure 1.5, it is clear that IMT materials exist with T_{IMT} over a very broad temperature range from cryogenic temperatures all the way to a thousand degrees K.

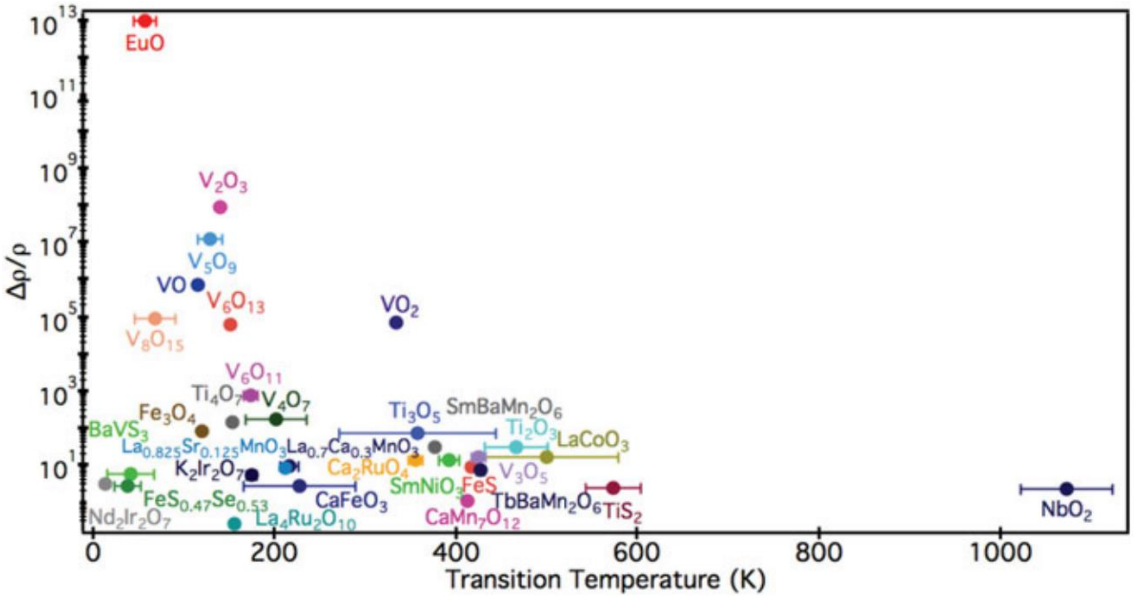

Figure 1.5: Insulator-metal transition for a variety of materials. The temperature of the IMT and corresponding change in the resistivity at the IMT for a variety of IMT materials is shown. Modified from [25].

One IMT material that is of particular interest is VO_2. VO_2 not only shows a very strong variation in its resistivity at its T_{IMT}, but also a near room temperature T_{IMT} of 67 ºC with a very narrow hysteresis. At low temperatures, VO_2 has a semiconducting electronic band structure with a band gap of 0.6 eV [26] and has a monoclinic crystal structure with tilted pairs of vanadium dimers. In the high temperature regime above its IMT, the band structure becomes metallic and the vanadium pairs relax causing the VO_2 to adopt a rutile structure. The vanadium pairing suggested that VO_2's insulator-metal transition was the result of a Peierls transition; however, failures of theoretical models based on the Peierls mechanism to reproduce the electronic properties of VO_2 has fueled near constant debate over the mechanism of the transition for the last three decades. This is discussed in more detail in section 1.2.2, where studies of the photo-induced IMT of VO_2 are discussed in detail. The readily accessible and strong IMT of VO_2 makes it readily accessible in practical devices for a wide variety of applications. It is also well known that the T_{IMT} can be further tuned by doping VO_2 with other atoms such as tungsten, fluorine [27] and titanium [28]. Among the many areas in which VO_2 has been used as an active material are thermo-chromic window coatings [29], optical memory [30], tunable optical filters [31] and RF switches [32].

Another material that has seen a lot of attention in recent years is NbO_2. Because of the much higher (1080 K) T_{IMT} of NbO_2, NbO_2 is far more resilient to ambient temperature fluctuations and device generated heat in device applications compared to VO_2. NbO_2 also shows a similar pairing of the Nb ions into a tilted dimer structure, but has a slightly different

body centred tetragonal structure in its low temperature phase. Above the transition temperature, the crystal structure becomes rutile and the band structure metallic. Because of the similarity between the IMTs of VO_2 and NbO_2, it has also been studied recently to help elucidate the IMT behaviour of VO_2. The higher temperature of the transition also makes it easier to distinguish thermal and non-thermal effects when trying to study the physical mechanism of the IMT process [33].

1.2.1 Electro-optic and Thermo-optic Modulators

Just as in the specific case of all-optical modulators, optical modulators in general rely on non-linear materials in order to modulate the transmission of an optical signal using some stimulus. The most common material used is $LiNbO_3$, which exhibits the Pockel's effect – a DC non-linear effect where the refractive index of a non-centrosymmetric crystal material is modified by the application of a strong DC electric field [34]. The Pockel's effect is significantly stronger than the optical Kerr effect used in all-optical modulators, but it still necessitates the used of large resonant structures in PICs [13].

One of the dreams of nanophotonics is to realize on-chip optical interconnects that can be integrated into semiconductor devices to achieve low-loss and high throughput data transmission between semiconductor transistors. For this to be possible though, it is essential that optical modulators with device sizes comparable to semiconductor transistors – that is 10s to 100s of nm – be developed. The large index contrast between the insulating state and the metallic state of IMT materials means that optical modulators using these materials have the potential to achieve large modulations without the need for long interaction lengths and large device sizes. This has spurred the investigation of a wide variety of nanoscale optical modulator devices using IMT materials.

The simplest optical modulators demonstrated using IMT materials are thermo-optic modulators. As the optical properties of IMT materials change at the T_{IMT}, simply heating a sample consisting of a waveguide coated with an IMT material above the T_{IMT} of the material will result in the material changing from its insulating state to its metallic state and cause a large change in the transmittance of the waveguide [35]. In one demonstration of a thermo-optic modulator, a short segment of a ring resonator was coated with VO_2. When the structure is heated above the 67 ^oC, both the absorption of the ring resonator and the resonant wavelength changes drastically. When the ring resonator is coupled to a waveguide, the transmittance of the waveguide at the ring resonator's resonance wavelength is drastically modified by the

IMT [36]. Another VO_2-based thermo-optic modulator replaced a nanoscale segment of a silicon waveguide with VO_2 to form a VO_2 optical waveguide segment. The large contrast in the absorption coefficient of the VO_2 between the insulating and metallic states resulted in a large modulation in the transmittance of the structure when the VO_2 was heated above 67 ^oC [37].

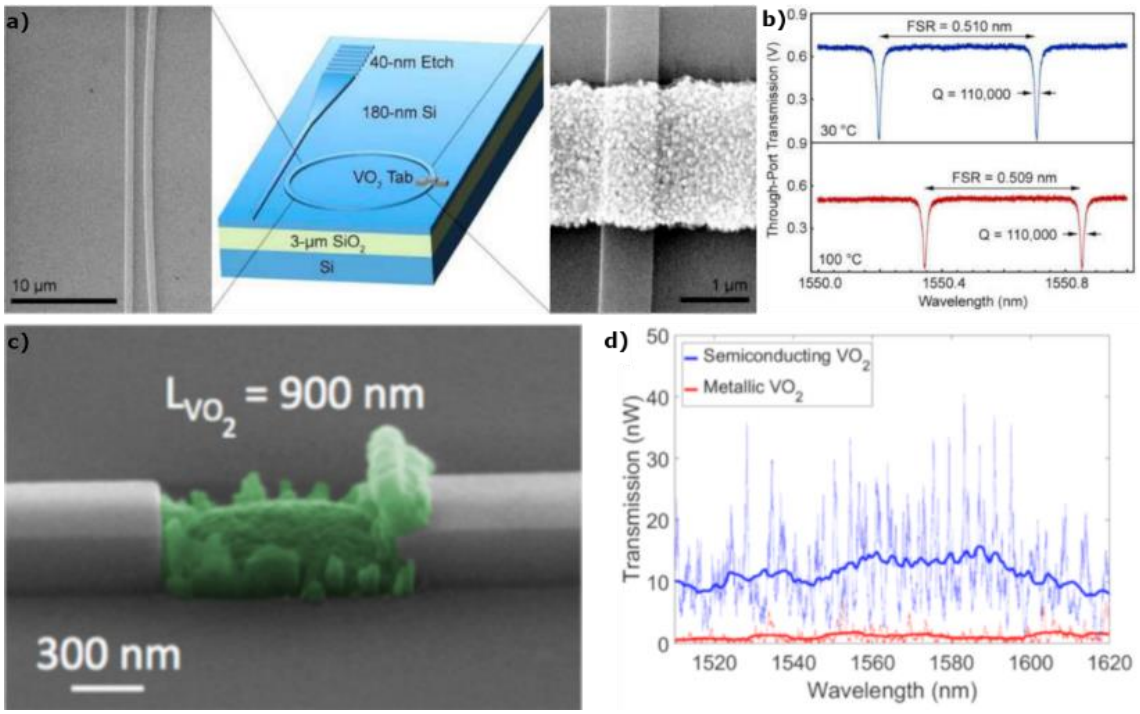

Figure 1.6: VO_2 based thermo-optic modulators. a) A ring resonator optical modulator using a small segment of VO_2 to induce a large change in the resonance of the ring resonator when VO_2 is heated above its T_{IMT}. b) Transmittance of the ring resonator coupled waveguide pictured in (a) below and above the T_{IMT}. c) Si waveguide integrated sub-wavelength thermo-optic modulator using a VO_2 waveguide section. d) Transmittance of the modulator pictured in (c) above and below VO_2 T_{IMT}. (a,b) are modified from [36] and (c,d) are modified from [37].

Although thermo-optic IMT-based modulators show promising performance, the inability to precisely control where the devices are heated makes them impractical for anything but simple demonstrations of a single modulator. For this reason, researches began to explore structures that would enable the local heating of IMT materials to trigger the IMT at specific locations [38]. In these devices, a bias is applied directly to the IMT material, and through Joule heating, the material is heated above the T_{IMT}, inducing the insulator-metal transition. A simple photonic waveguide coated with VO_2 biased by electrical contacts was demonstrated to have an extinction ratio (relative change in transmittance between the on and off state in dB) of 12 dB with small length of 1 μm [38]. In order to further reduce the size of these devices, plasmonic designs that incorporate noble metals to concentrate the propagating optical signal into the VO_2 were also demonstrated by several groups [39,40]. Due to the use of heating to

induce the IMT, the recovery of these devices was limited by heat dissipation, and the fastest modulation speeds that could be obtained were one the order of ns or even µs.

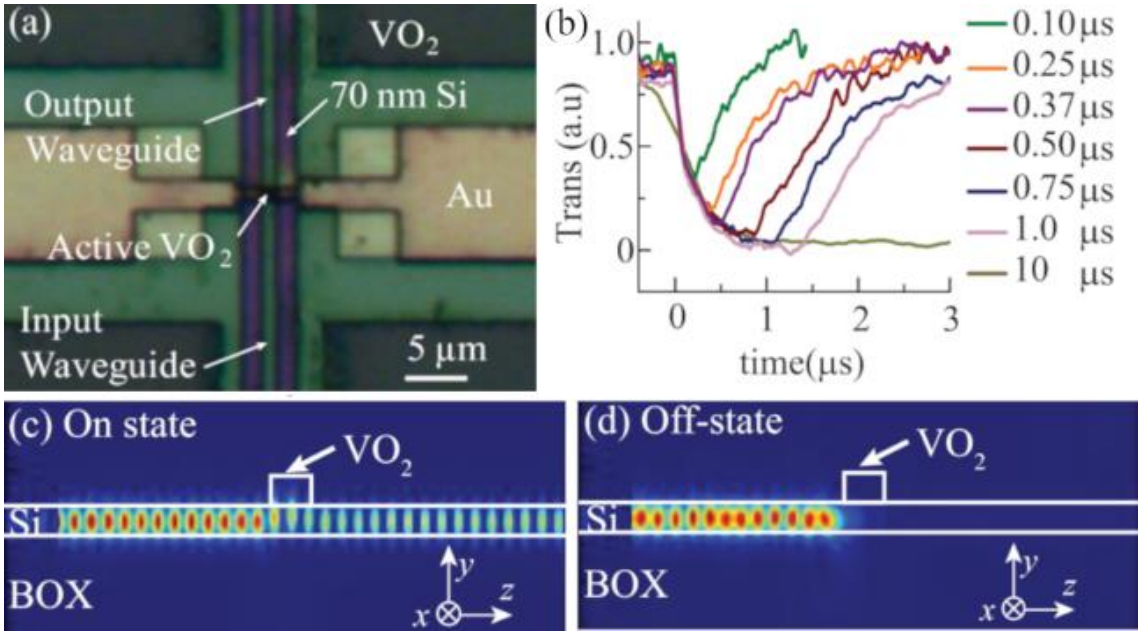

Figure 1.7: Electro-optic modulator based on resistive heating of VO_2. a) Microscope image of a Si waveguide integrated current switched modulator. b) Modulation in the transmittance of the modulator pictured in (a) after current pulse with varying widths. c,d) electric field distribution of light propagating through the Si waveguide when VO_2 is in its dielectric (c) or metallic (d) state. Modified from [41].

The discovery in recent years that the IMT of VO_2 can be triggered through electron injection by a strong electric field [42] in addition to thermally through Joule heating spurred further interest in developing electro-optic modulators using VO_2 in order to achieve higher speed modulations. Modulation of the THz transmissivity of a VO_2/Au metamaterial was performed using a strong AC field to act as a tunable optical filter [43]. A waveguide-integrated design based on applying a bias to Au nanodisks on top of a VO_2 coated waveguide in order to cause an electrically induced IMT has also been proposed [44].

1.2.2 Photo-induced Insulator-Metal Transition

Since the discovery of the IMT behaviour in VO_2 many years ago, there has been a constant debate about the mechanism of the IMT and whether the change in the electrical band structure of VO_2 is due to a Mott transition, a Peierls transition or some combination of the two. With the advent of ultrafast time-resolved spectroscopy techniques using pulsed lasers, it became possible to study the dynamics of physical processes, and the technique began to be applied to VO_2 in the hope of understanding the mechanism of the IMT better. With the first ultrafast time-resolved spectroscopy study of VO_2 in the 1970s by Roach and Balberg, it was found that the IMT could be induced through photo-excitation [45]. This launched a half-

century of studies of the photo-induced IMT of VO_2 in the hopes of developing a better understanding of the physics of VO_2 and IMT materials in general.

A vast literature of studies relating to the photo-induced IMT exists [46–51]; however, as the understanding of the photo-induced IMT has changed drastically over the last five decades, only the most relevant literature that provides a full description of the current understanding of the photo-induced IMT of VO_2 will be discussed here.

When VO_2 is excited by an ultrashort laser pulse, many different processes occur simultaneously, and as a result, the response is very complex and exhibits several regimes of behaviour depending on the fluence of the pump laser used to excite the VO_2 as well as the temperature of the VO_2. One very good overview of the different regimes and responses observed in the photo-induced response of VO_2 is provided by Cocker et al. [50]. In their study, Cocker et al. use a 100 fs laser pulse at 800 nm from a Ti-sapphire laser to excite a thin-film of VO_2 deposited on an Al_2O_3 and measure the time-resolved change in the THz transmittance of the film using pump-probe spectroscopy for a range pump fluences and sample temperatures. In these measurements, shown in Figure 1.8, they found four regimes of behaviour separated by threshold pump fluences where the dynamics of the response change.

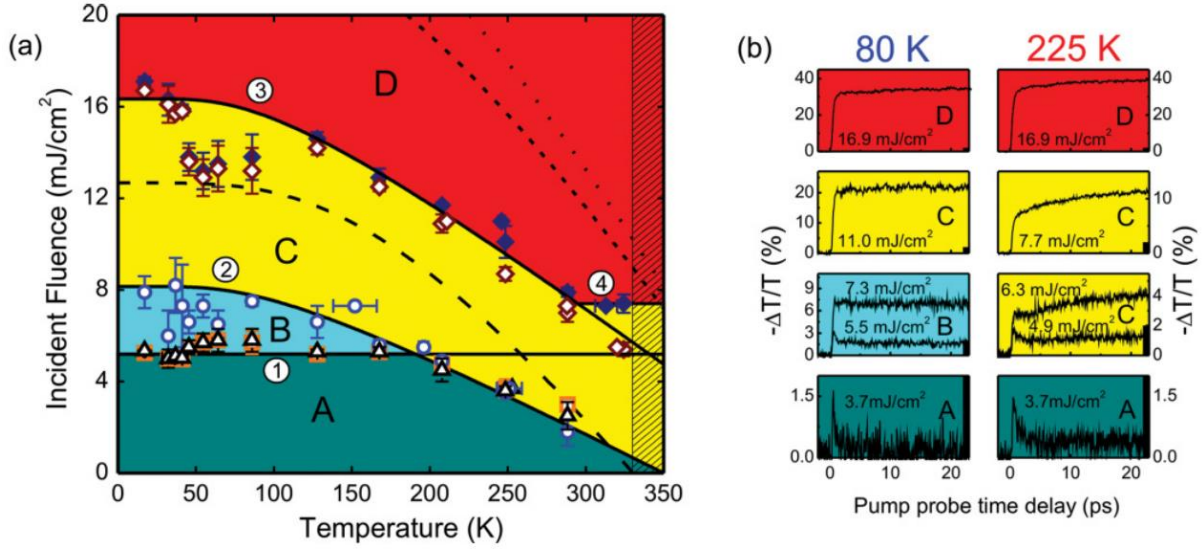

Figure 1.8: Phase diagram of the photo-induced response of VO_2. a) The phase diagram of the photo-induced modulation of VO_2 with the ranges of pump fluence and substrate temperatures of the four regimes of behaviour demarked. b) representative time-resolved differential transmittance for the four unique regions of behaviour for a substrate temperature of 80 K and 225 K. Reproduced from [50].

As seen in Figure 1.8a, the lowest fluence regime, regime A, is present at all temperatures and represents the low-fluence limit of the photo-induced response. In the bottom row of transient differential transmittance measurements shown in Figure 1.8b, the time-resolved response in regime A for a sample temperature of 80 K and 225 K can be seen. The

response consists of a sharp decrease in the transmittance that decays after several ps and a long-lived decrease in the transmittance, which the authors attribute to a semiconductor-like response without going into detail on the exact mechanism of the modulation observed. In a mid-fluence regime C, after the short-lived semiconductor-like peak, the modulation of the transmittance continues to increase for nearly 100 ps after the incident fs pump pulse. This increasing modulation is attributed to grains of the VO_2 undergoing an IMT through a Peierls transition triggered by 6 THz phonons that map the VO_2's initial insulating monoclinic structure to its metallic rutile structure. The 100 ps length of the increasing modulation to the was attributed to the lifetime of these phonons [50]. It was later found that these 6 THz do not map the monoclinic structure to the rutile structure [52]. It was also found that the IMT being driven in this regime C cannot be due to photothermal heating, as the pump fluence necessary to heat the sample to the IMT temperature, shown by the long dashed line in Figure 1.8a, is higher than the threshold seen for regime C. The onset of the IMT is therefore explained by the excitation of critical density of 6 THz phonons triggering an IMT in specific grains of VO_2. The phonons then diffuse to neighbouring grains of VO_2 triggering the IMT in these grains and leading to a steadily increasing modulation. As the phonons decay to lower energy phonons with a lifetime on the order of 100 ps, the increasing modulation ceases. Because the effective pump fluence is different at different depths of the film this phenomenon is observed. If the pump fluence is increased above a threshold where the entire film is excited to the critical phonon density, then the modulation reaches its maximum value instantly and does not increase further, as is the case for regime D [50].

Regime B is a special case only observed at low temperatures. In regime B, it is believed that a critical density of carriers sufficient to induce an IMT through a Mott transition is excited while the phonon density is not high enough to induce a phonon-driven CPT by the Peierls mechanism [50]. The authors propose that this represents a purely electronic IMT by means of a Mott transition to a monoclinic VO_2 state. As a whole, the article argues that both Mott and Peierls phenomenon are present in VO_2 and that for the full IMT and CPT to the high-temperature rutile structure, both a Mott and Peierls transition occur [50].

The interesting behaviour found in the mid-fluence region where VO_2 was proposed to undergo partial IMT that spreads to neighbouring grains inspired an investigation of the actual crystal structure of VO_2 in this mid-fluence regime. Morrison et al. harnessed the new technique of ultrafast electron diffraction to obtain a time-resolved picture of the evolution of the crystal structure of VO_2 after excitation by a femtosecond laser pulse [53]. In their time-

resolved differential transmittance measurements, they found a similar behaviour to that described by Cocker at al. with a non-linearity in the long-lived modulation of the differential transmittance appearing at a threshold fluence around 2 mJ/cm^2. In their time-resolved electron diffraction measurements, however, they found a very different behaviour. They focussed on two diffraction peaks of the low-temperature monoclinic phase of VO_2: the $30\bar{2}$ peak, which is related to the distorted monoclinic structure and disappears when the VO_2 changes to the high-temperature rutile phase; and the 220 peak, which changes intensity but do not disappear upon the CPT. As seen in Figure 1.9a, the 220 peak was found to continually increase in intensity for pump fluences above the optically measured threshold of 2 mJ/cm^2, while the $30\bar{2}$ peak remains constant and only decreases until a higher threshold of 9 mJ/cm^2. Furthermore, the timescales of the two peaks are significantly different, with the $30\bar{2}$ decreasing on a sub-ps timescale and the 220 peak increasing on a several ps timescale (Figure 1.9b). These results suggest that in the mid-fluence region, VO_2 transitions to a new crystal structure that is still monoclinic, while having metal-like optical properties, providing support for the idea that VO_2 undergoes a Mott transition triggered IMT before the CPT to the high-temperature rutile phase.

Although the presence of a metal-like optical response in the mid-fluence suggested the presence of an IMT to a monoclinic metal, a metal-like optical response can also be created by non-metallic electronic band structures, such as high-densities of photo-excited carriers or electron hole plasmas. For this reason, Wegkamp et al. used time-resolved photoelectron spectroscopy to probe the actual band structure of VO_2 after photoexcitation [54]. As can be seen in Figure 1.9c, upon excitation by a 6.7 mJ/cm^2 femtosecond laser pulse, the band structure collapses in less than 60 fs (duration of the pump pulse) and electrons are found at the fermi level, indicating a metallic band structure. Unfortunately, the pump fluence used in this experiment is very close to the threshold for the onset of the CPT measured by Morrison et al. (9 mJ/cm^2), and the differences between samples means that 6.7 mJ/cm^2 cannot be guaranteed to be below the CPT threshold of the samples measured by Wegkamp. These results do confirm that the photo-induced state at high pump fluences has a metallic band structure and that the collapse of the band gap occurs on a timescale faster than ionic movement can occur. Since a Peierls transitions requires the crystal structure to change first before the band gap collapses, the authors contend that this confirms that the IMT occurs through a photo-excited carrier triggered Mott-transition and that the new coulomb potential of the metallic band structure subsequently drives a CPT to the high-temperature rutile structure.

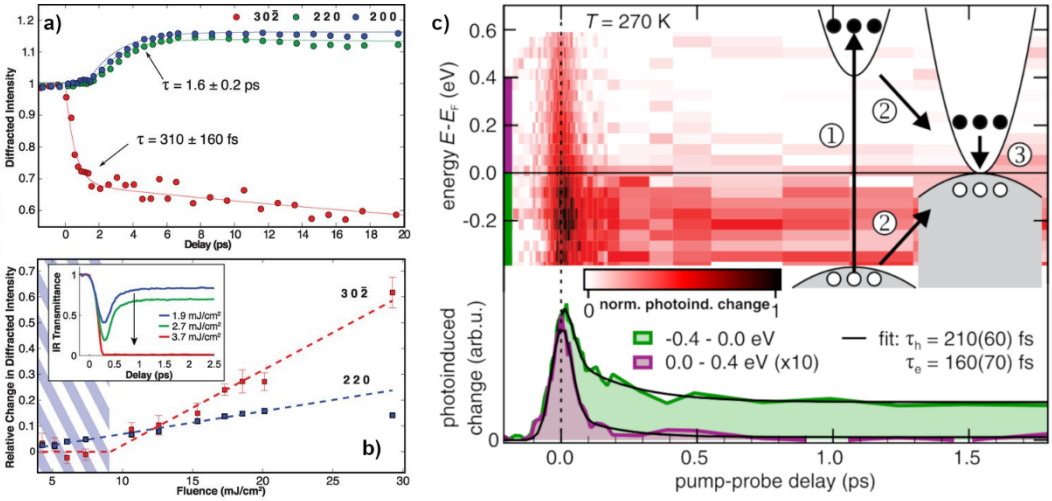

Figure 1.9: Evidence of the monoclinic metal phase of VO_2. a) time-resolved change in the diffraction intensity of the diffraction peaks associated with the monoclinic and rutile crystal phases of VO_2. b) Fluence dependence of the relative change in the diffraction intensity of the 302 and 220 peaks of VO_2. c) time-resolved photoelectron spectroscopy measurement of VO_2 after excitation by a 6.7 mJ/cm^2 femtosecond laser pulse, showing a clear collapse of the bandgap and the presence of electronic states within at the fermi-level. (a,b) are reproduced from [53] and (c) is reproduced from [54].

Following their ground breaking work on the photo-induced IMT of VO_2, Wegkamp et al. published a detailed review article where they gave a detailed overview of the photo-induced IMT and CPT of VO_2 [52]. They gave a pictorial representation of their proposed mechanism, which is shown in Figure 1.10. In their proposed mechanism for the IMT at high fluences, an ultrashort laser pulse first excites a large number of photo-excited carriers to the conduction band of the VO_2. This high density of photo-excited carriers screens the lattice charge and results in an IMT through a Mott transition mechanism within tens of fs. The new metallic band structure causes a change in the lattice potential which subsequently drives a CPT that occurs on the order of several ps. As the photo-excited carriers relax to the fermi level, they generate a significant amount of heat that stabilizes the rutile crystal structure, and the VO_2 does not recover its insulating monoclinic structure until this extra heat has been dissipated. Wegkamp et al. also suggested that for mid-fluences the monoclinic metal could be excited without triggering the CPT. Believing this would be a purely electronic process, they suggested that the recovery of the VO_2 back to its insulating state from this monoclinic metal could happen on a sub-ps timescale, allowing for sub-ps modulation of the optical properties of VO_2.

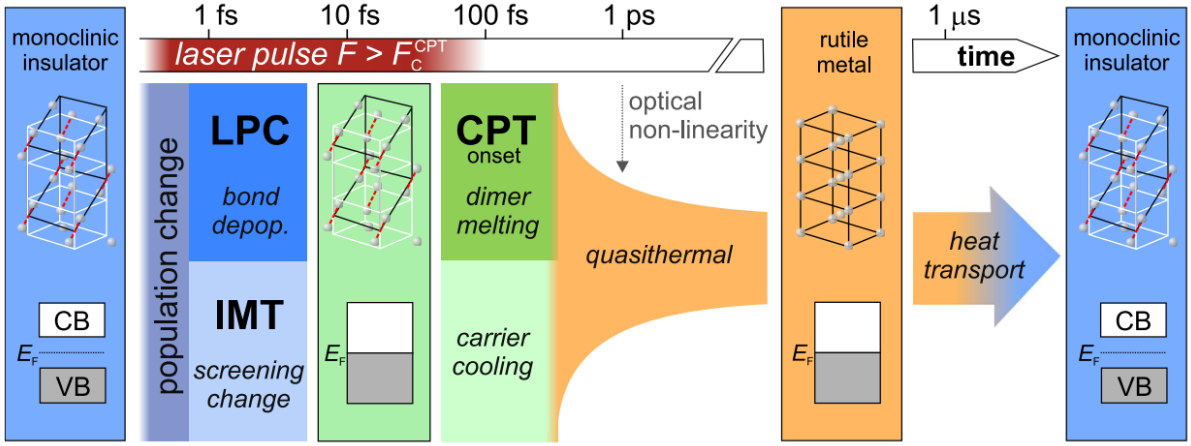

Figure 1.10: Pictorial representation of the dynamics of VO_2's photo-induced IMT.

Despite the large number of studies on the mechanism of the photo-induced IMT of VO_2 and the response of VO_2 in the initial several ps after photo-excitation, there have been very few studies of the recovery of VO_2 to its initial state after photo-excitation. This is especially important for applications of VO_2 as an all-optical modulator material, as a modulator device cannot be operated any faster than it takes the device to recover to its initial unmodulated state. It is also important to note that the recovery of the mid-fluence monoclinic metal state at sub-ps speeds as proposed by Wegkamp et al. has also yet to be confirmed. Two main studies have been performed on the recovery of VO_2 after a photo-induced IMT. In the first, varying thicknesses of VO_2 ranging from 20 to 500 nm deposited on various substrates were excited by a fs laser pulse, with the recovery of the film being found to be governed by thermal dissipation from through the substrate material, and the fastest recovery times on the order to several ns [55]. A further study studied the recovery of the time-resolved X-ray diffraction as well as the time-resolved differential reflectance of VO_2 after excitation by a high-fluence fs laser pulse, where the VO_2 was found to undergo a full IMT and CPT to a rutile structure and recovery of the low-temperature monoclinic phase was governed by the dissipation of heat to the substrate and limited to a recovery time of several ns [56]. As of the writing of this thesis, there has yet to be a demonstration of the recovery rate of VO_2 from the proposed mid-fluence monoclinic metal or with recovery times on a sub-ns timescale.

Because of the near room temperature T_{IMT} of VO_2, the photo-induced response and recovery afterwards of VO_2 is often complicated by photo-thermally triggered effects. For this reason, the photo-induced IMT of another IMT material, NbO_2, has also been investigated in recent years. The first investigation of the photo-induced modulation of NbO_2 was undertaken by Beebe et al [33]. In their study, they found that NbO_2 after excitation by a fs laser pulse,

NbO_2 had a response similar to VO_2 in the low-fluence regime. The reflectance at 800 nm of NbO_2 showed a sharp decrease to a minimum value on a timescale limited by the laser pulse width. There was then a partial recovery on an ultrafast fs timescale limited the laser pulse width, followed by another partial recovery on a timescale of several ps. Finally, the reflectance of the NbO_2 did not recovery to its initial value until several ns later. The authors attributed the fs recovery, ps recovery and ns recovery to relaxation of photo-excited carriers, the relaxation of grains of NbO2 that had undergone a purely electronic IMT to a short-lived metallic state with the same crystal structure as the low-temperature NbO_2 (body centred tetragonal), and the relaxation of grains of NbO_2 that had undergone a full IMT and CPT to the high-temperature rutile phase of NbO_2, respectively. A gradually increasing modulation in the long-lived response found at high pump-fluences was attributed to a thermally-induced IMT in additional NbO_2 grains fueled by heat generated by the relaxation of photo-excited carriers in NbO_2 grains that had undergone an IMT and CPT.

A later study by Rana et al. studied the change in the terahertz conductivity of NbO_2 after photo-excitation [57]. There, they found two non-linearities in the pump fluence vs. the long-lived THz conductivity modulation and found it could be modelled as a Drude-Lorentz response, suggesting the NbO_2 had undergone an IMT to a metallic state. The non-linearities were found at pump fluences of 10 mJ/cm^2 and 17 mJ/cm^2. The former corresponding to a pump fluence insufficient to photo-thermally heat the sample above NbO_2's T_{IMT} was proposed to represent a non-thermal IMT. Both the recovery rate of the long-lived modulation and the nature of the short-lived modulations have yet to be studied in detail.

1.2.3 Photo-thermal All-Optical Modulation

In the hopes of achieving the predicted sub-ps ultrafast all-optical modulation, Weiss et al., fabricated an all-optical modulator using a silicon micro ring resonator with a slab of VO_2 coating a portion of the VO_2 [58]. The structure fabricated by the group can be seen in Figure 1.11a below. By sending a femtosecond laser pulse with an energy above the bandgap of VO_2, they were able to excite a large number of photo-excited carriers in the VO_2 and optically induce the IMT. The transmittance of a CW 1.55 μm laser was found to be strongly modified by the IMT with a modulation as large as 10 dB measured for high pump intensities. However, when they monitored the recovery of the device, they found that the modulation was extremely long-lived and lasted for several μs. Though reducing the pump intensity saw a reduction in the recovery time, the modulation depth was also significantly decreased, and the

shortest recovery rate that could be achieved was on the order of hundreds of ns. Furthermore, the recovery was found to be governed by heat dissipation of the device, and it was concluded that the IMT was induced through a photo-thermal process where the VO_2 was heated above the T_{IMT} through the relaxation of photo-excited carriers as opposed to a purely electronic IMT induced by photo-excited carriers. Since this demonstration, there has still yet to be a demonstration of the photo-induced IMT of VO_2 with recovery on a sub-ns timescale.

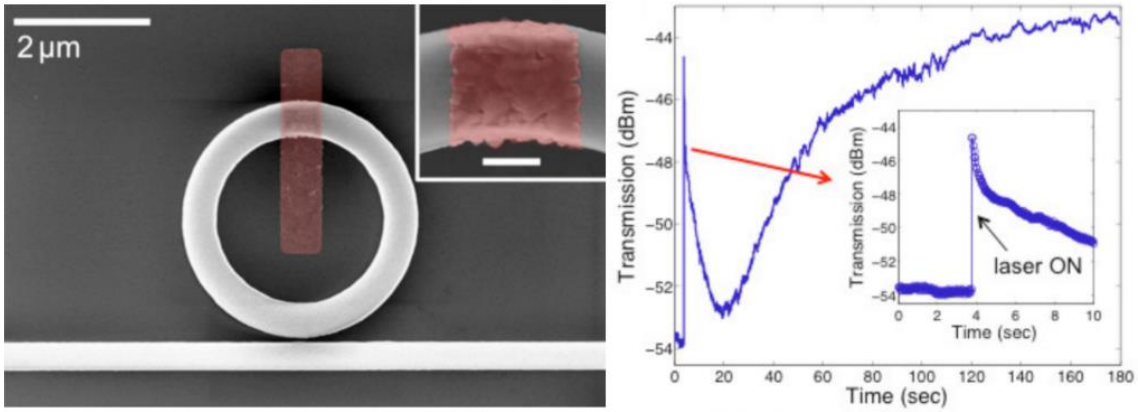

Figure 1.11: All-optical modulator using the photothermally induced IMT of VO_2. a) False coloured SEM of the VO_2 coated micro-ring resonator modulator. Using a pump pulse at one of the ring-resonator resonances, the VO_2 can be heated above the IMT through photothermal excitation. b) Measured modulation in the transmittance of a CW probe laser after photothermal excitation, showing very slow recovery on the order of hundreds of seconds. Modified from [36].

1.3 Ultrafast Time-Resolved Spectroscopy

The photo-induced metal-insulator transition, and many other optically induced physical phenomena have dynamics that occur on sub-picosecond timescales; however, detecting and measuring these dynamics is not a trivial matter. In the case of the insulator-metal transition, after excitation by an optical signal, a sub-picosecond modulation in the optical properties of the insulator-metal transition material is induced, and this modulation can be probed by shining another optical signal onto the material. The modulation and information about how it changes in time will be encoded onto the transmitted and reflected portions of the probing signal; however, for this information to be extracted, the probing signal must subsequently be detected and measured.

In order to detect the optical signal, opto-electronic photodetectors that convert the optical signal to an electrical signal must be used. Even if the optical signal has features with a sub-picosecond timescale, the best photodetectors are limited to response times on the order of tens of picoseconds, and this results in any signal features faster than tens of picosecond being smeared out in the outputted electrical signal, as shown in Figure 1.12 below. Following this, the electrical signal is then passed to an electrical device that can measure the signal, such as

an oscilloscope. Here, the inductance and capacitance of the electrical circuitry connecting the two devices and the limited response time of the measuring device further act to smear the electrical signal out in time. Because of these limitations, using standard electrical detection equipment, it is not possible to measure an optical signal modulation that is shorter than tens to hundreds of ps.

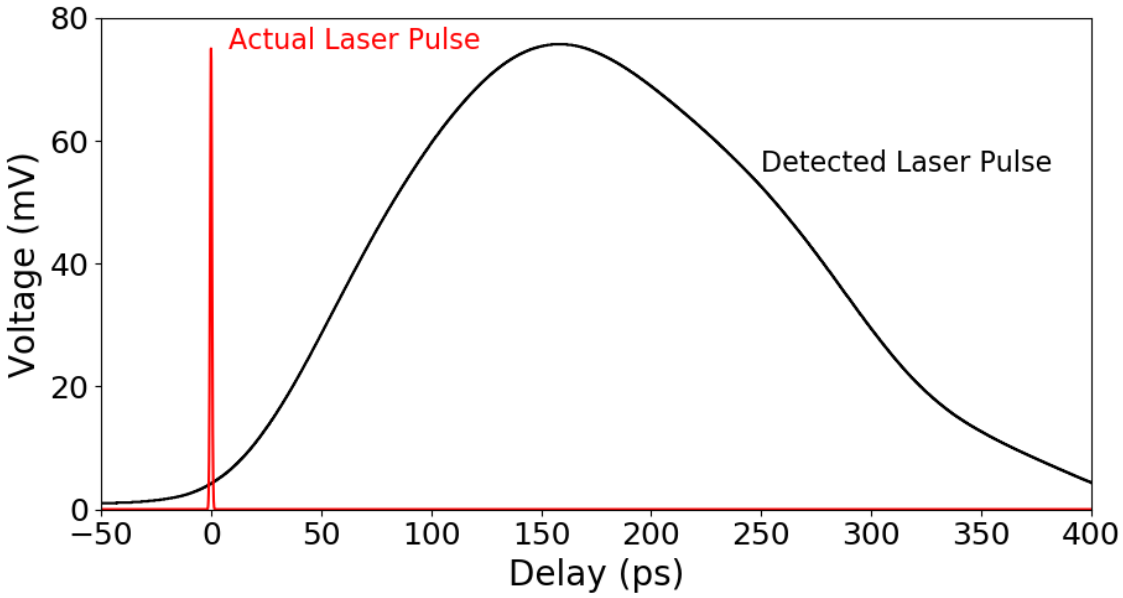

Figure 1.12: Temporal limitation of electrical detection. An ultrashort 350 fs femtosecond laser pulse (red) is distorted and elongated in time as it is detected by a photodetector and passed to an oscilloscope to produce a displayed pulse with a far longer pulse time (black).

In order to detect sub-picosecond modulations, such as the modulation caused by the photo-induced metal insulator transition, special methods are necessary. The two most common methods are using the technique of pump-probe spectroscopy and using a streak camera [59].

Pump-probe spectroscopy is the technique used in this thesis work, and measures the transient modulation caused by one ultrashort laser pulse by probing the modulation using another ultrashort laser pulse whose delay in time relative to the first pulse is varied. Pump-probe spectroscopy has been used to measure ultrafast physical phenomena down to attosecond time scales; however, it can only be used in cases where the stimulus of the modulation is a laser pulse [59]. A detailed description of this technique is given in the following subsection.

A streak camera is a specialized camera that translates an optical signals variation in time into a variation in space on a one-dimensional array of detectors. The streak camera is initially set up so that the incoming optical signal will impinge on one end of the array of detectors. After receiving a triggering signal, the streak camera begins to move the position at which the optical signal impinges on the array of detectors and this maps the optical signal measured by a detector

at a particular position on the array to a particular time after the triggering signal. Attosecond resolution detection has recently been achieved using a streak camera design [60]. However, due to the high cost and complexity of such systems, this method was no pursued in this work.

1.3.1 Pump-Probe Spectroscopy

Pump-probe spectroscopy is a technique that can be used to obtain time-resolved measurements of the variation in the optical properties of a material, structure or device at as high as attosecond resolutions. An object is excited by a pump laser pulse, and then the modulation in the optical properties at different points in time is probed by means of a probe laser pulse [59]. Figure 1.13 outlines a simple description of the basic principles of operation of pump-probe spectroscopy.

First, an ultrashort pump and ultrashort probe pulse that have a defined initial delay, Δt_0, are generated. The probe pulse is then passed through a delay line that consists of a series of optical mirrors that divert the probe light and increase the distance travelled the probe light. The distance between these mirrors, Δd_{delay}, can be varied by means of a mechanical stage, and this allows the probe pulse to be delayed by a specific amount of time, Δt_{delay}, defined by,

$$\Delta t_{delay} = 2N_{passes}\left(\frac{\Delta d_{\text{delay}}}{c}\right)$$

where N_{passes} is the number of times that the probe pulse passes through the delay line (1 in the example shown in Figure 1.13), and c is the speed of light in the ambient medium (in most cases air). The pump pulse then excites the object in question and induces a transient change in the optical properties of the object. When the probe pulse reaches the sample, it probes the optical properties of the object at the probe wavelength the instant in time it reaches the material. The signal obtained from this measurement is then the convolution of the optical property being probed and the probe pulse at the instant in time that the probe reaches the object. By scanning Δd_{delay}, the delay of the probe pulse can be varied, and the change in the optical property over time can be reproduced.

For example, in Figure 1.13, the pump pulse is shown inducing a transient decrease in the transmittance of a material at the probe wavelength. When the probe pulse reaches the sample, the percentage of the probe pulse transmitted depends on the transmittance of the material at the instant in time that the probe pulse reaches the sample. The transmitted probe, $I_{\text{probe}}(t)_{\text{f}}$, pulse is defined by the convolution of the function of the transmittance in time, $T(t)$, and the probe pulse intensity in time $I_{\text{probe}}(t)_{\text{i}}$,

$$I_{\text{probe}}(t)_{\text{f}} = I_{\text{probe}}(t)_{\text{i}} * T(t)$$

After passing through the material, the transmitted probe signal would be detected by a photodetector and measured using either an oscilloscope or a lock-in amplifier. By measuring the signal strength for different probe pulse delays, and then scaling the values by the signal strength when no pump-pulse is incident on the material, the change in the transmittance of the material with time *T(t)* can be reproduced.

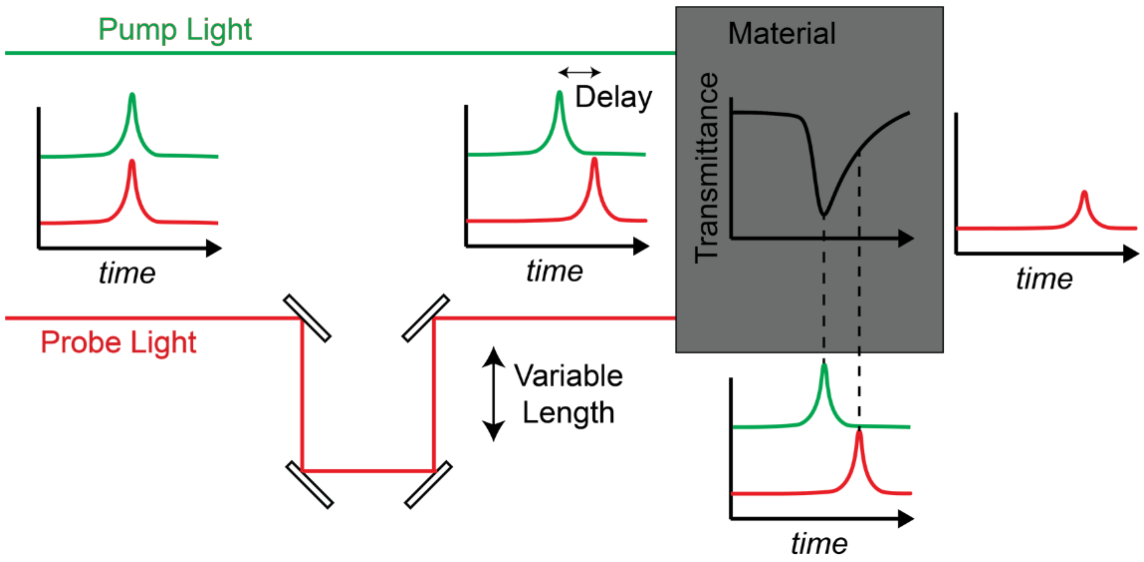

Figure 1.13: Time-resolved transmittance measurement with pump-probe spectroscopy.

Pump-probe spectroscopy has been used to study physical phenomena that occur at as fast as attosecond speeds, but there are two key considerations that must be made when determining the maximum temporal resolution of a pump-probe spectroscopy system. Most importantly, the physical length of the optical path is used to determine the delay in time of the probe pulse, and as such, the mechanical resolution of the delay line determines the minimum possible delay resolution. In addition to this, because the probe pulse has a finite temporal width, it will probe note only the properties of the object at the centre of the probe pulse, but along the entire duration of the probe pulse. For this reason, the resolution of optical property is also limited by the probe pulse duration, and any changes in the optical properties occurring on a timescale faster than the probe pulse duration will be smeared out in a similar way that ultrafast optical signals are smeared out when detected by electrical photodetectors.

1.4 Thesis Structure and Objectives

From the prior discussion in this chapter, it is clear that all-optical modulators have the potential to be a revolutionary technology in the telecommunications and computing industry.

Insulator-metal transition materials, and in particular VO_2 and NbO_2, have been shown to be promising materials for nanoscale and high-speed all-optical modulators with strong modulations; however, before all-optical modulators that boast these properties can be designed, several questions about the photo-induced IMT of VO_2 and NbO_2 must be answered. Among these are, what is the nature of the short-lived modulation seen when VO_2 and NbO_2 are excited at low fluences, how fast can these materials be modulated and can a strong modulation and fast recovery both be achieved, and can the IMT threshold be engineered to make lower power and more practical all-optical devices using these materials.

The following thesis provides an in depth study of the photo-induced modulation of VO_2 and NbO_2, with a focus on the dynamics of the recovery of VO_2 and NbO_2 after a photo-induced IMT, as well as a demonstration of how plasmonic nanostructures can be used to improve the efficiency and efficacy of the optical modulation of IMT materials after a photo-induced IMT. Chapter 1 provides a brief background of research on all-optical modulators, IMT materials and the techniques for measuring ultrafast optical phenomenon. Chapter 2 outlines the theory of the pump-probe spectroscopy technique used for measuring the ultrafast response of the materials and devices presented in this thesis, as well as a detailed overview of the experimental setup built for this work. In Chapter 3, the fabrication and characterization of the VO_2 and NbO_2 thin-films used in this work are discussed. Chapter 4 focusses on the photo-induced modulation of VO_2 and NbO_2 thin-films. The physical processes governing the photo-induced response as well as the dynamics of the recovery are discussed in detail, with a new mid-fluence region where VO_2 undergoes an IMT and shows fast recovery being discovered. Chapter 5 studies how the recovery dynamics can be engineered through the use of ultra-thin thin-films and nanostructuring. A plasmonic nanostructure incorporating VO_2 is demonstrated to be capable of concentrating light into VO_2 in order to reduce the threshold fluence needed to induce an IMT in VO_2 and enhance the modulation in the optical properties of the structure in Chapter 6. In Chapter 7, the potential of all-optical modulators designed using IMT materials and plasmonic nanostructured is shown through the design and optimization of a nanoscale hybrid plasmonic-photonic all-optical modulator. Finally, in Chapter 8, the key conclusions of this work are detailed, future avenues of potential research are discussed, and applications where the results of this work would be useful are proposed.

Chapter 2 : Micro Pump-Probe Spectroscopy Setup

As discussed in section 1.3, the high speed of the optically induced modulation of insulator-metal transition materials necessitates the use of a special measurement technique. In this work, I chose to use pump-probe spectroscopy, and as such, as a first step in my research, it was necessary to build a pump-probe spectroscopy setup. I built a unique micro pump-probe spectroscopy setup that allows the pump and probe pulses to be manipulated at the microscale.

In this chapter, I give a detailed overview of the pump-probe spectroscopy setup built for this work. A general outline of the pump and probe light paths and the individual components is first given. Following this, a discussion of the unique elements in this specific pump-probe spectroscopy setup, such as the sample imaging and signal injection components, the spatial filtering apparatus, and the repump section is provided. Finally, the key obstacles that were confronted during the assembly of the setup and how they were overcome is discussed.

2.1 Overview

In pump-probe spectroscopy, before any spectroscopy can be performed, it is necessary to produce an ultrashort pump and probe laser pulse that are synchronized in time and can be used to modulate and probe, respectively, the material or device under study. In this setup, a Light Conversion Orpheus-HP optical parametric amplifier (OPA) is used to produce the pump and probe pulse. A 515 nm laser pulse with a pulse width of 250 fs from a Light Conversion Pharos laser is first injected into the OPA. Using difference frequency generation, the OPA then splits the 515 nm laser pulse into a 766 nm signal pulse and a 1551 nm idler pulse that are synchronized in time and space.

Both laser pulses are then directed into the pump-probe spectroscopy setup detailed in Figure 2.1 below. As seen in the schematic diagram on the right side of Figure 2.1, the 766 nm signal pulse and 1551 nm idler pulse are injected into the setup on the left side. At the beginning of the setup, a shortpass filter splits the two laser pulses by reflecting the 1550 nm idler pulse, which is used as the probe light, and transmitting the 766 nm laser pulse, which is used as the pump light. After this point, the pump and probe light follow separate optical paths.

The probe light (solid black line) is redirected by a series of mirrors and directed towards a Newport optical delay line. In this setup, the probe light is reflected back and forth between the delay line and a series of mirrors a total of 4 times, resulting in the probe light traversing the distance between the mirrors and the delay line 8 times, which adds a significant

temporal delay to the probe pulse. The delay line is motorized with a range of movement of 32.5 cm and a translational resolution of 75 nm, making it possible to delay the probe pulse by up to 8.67 ns with a temporal resolution of 2 fs. After passing through the delay line, the probe light is directed towards the position of Chopper 1. When measuring the unmodulated transmittance or reflectance of the sample, Chopper 1 is placed in this position, and the probe pulse is periodically blocked at the frequency of chopper. When measuring the modulation, Chopper 1 is removed, and the probe pulse passes through unperturbed. A further discussion of how the choppers are used is given in section 2.2. Next, the probe light reaches the location of Shortpass Filter 2. For transmittance measurements, Shortpass Filter 2 reflects the probe light and directs it towards Lens 2 behind the sample, where it is then injected into the sample from the backside. In the case of a probe reflectance measurement, the probe Shortpass Filter 2 is instead removed, and the probe light is allowed to travel straight (dashed black line), where it is then injected into the sample from the front side through Lens 1. After injection into the sample, the transmitted or reflected probe light is collected through Lens 1, where it reflects off several beamsplitters and is directed towards the IR and Visbile Cameras and the fibre coupler. The probe light directed to the fibre coupler is coupled into a fibre optic cable and detected by a photodetector, while a microscope image of the probe pulse is created by the cameras.

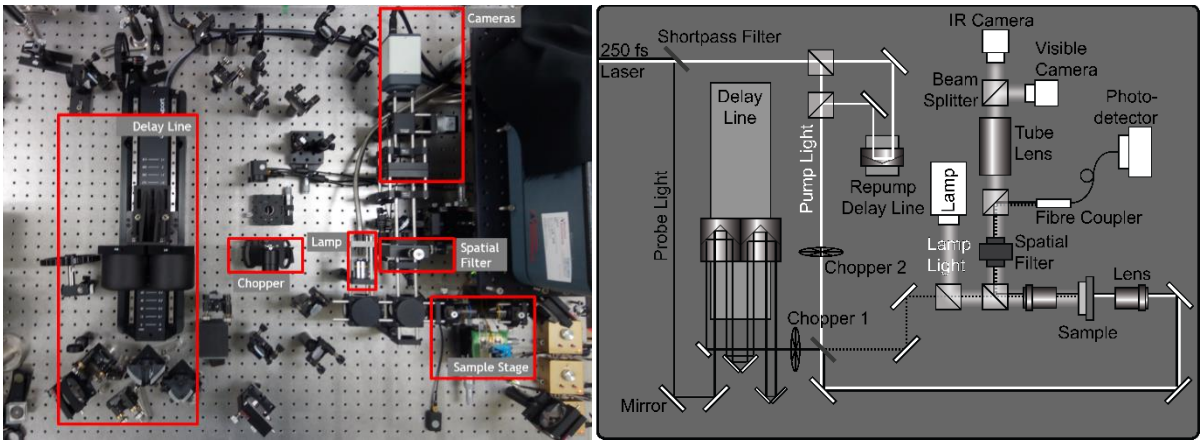

Figure 2.1: Micro-pump-probe spectroscopy setup. Image (left) and schematic diagram (right) of the pump-probe spectroscopy setup used in this work.

The pump pulse (solid white line) is first reflected several times to make the optical path length of the pump pulse similar to that of the probe pulse. For pump-repump-probe experiments, the pump pulse is then split in two with a beamsplitter and an additional delay is added to one of the pump pulses with a manual delay line. The two pump pulses are then recombined using a beamsplitter and directed towards Chopper 2. In the case of a normal pump-

probe measurement, the beamsplitters are removed, and the pump pulse is allowed to travel directly towards Chopper 2. After this, the pump pulse(s) is(are) directed towards Lens 2 and injected into the sample from the backside where they induce a modulation in the optical properties of the sample.

2.1.1 Signal Injection and Spatial Filtering

One unique aspect of this pump-probe spectroscopy setup is the ability to visualize and manipulate the pump and probe pulses on the microscale as well as the ability to isolate and collect only the probe light coming from a specific point in space.

On the left of Figure 2.2 an image of the sample stage area, where the microscale manipulation of the pump and probe pulses is achieved, is shown. The sample stage area consists of two objective lenses. One is located to the right of the sample, and is used to inject the pump light – and the probe light when measuring transmittance – into the sample. The other objective is located to the left of the sample, and is used to inject the probe light when measuring reflectance as well as collect the light that has been either reflected or transmitted by the sample. The light collected by the objective lens to the left of the sample is then directed to the visible and IR cameras where it can be visualized. Images of the probe spot and pump spot on a sample can be seen in the top right and the top bottom right of Figure 2.2, respectively. Here the pump pulse has a wavelength of 766 nm and is therefore imaged by the visible camera, whereas the probe pulse, which has a wavelength of 1551 nm is imaged by the IR camera.

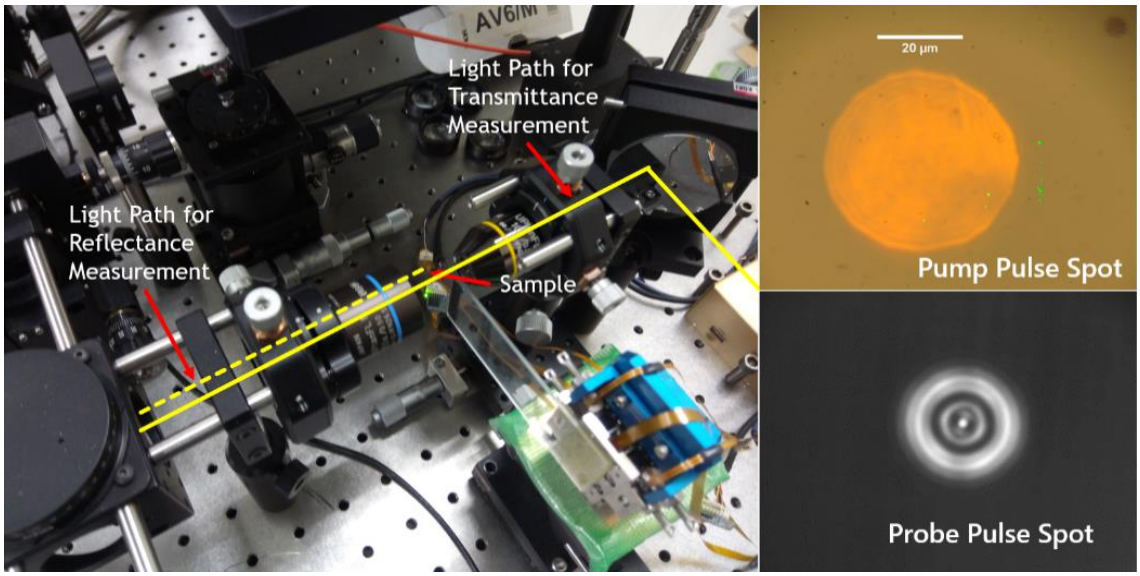

Figure 2.2: Sample stage and pump/probe spot images.

The position and angle at which the pump and probe pulses illuminate the sample can be easily controlled with microscale accuracy by adjusting the angle at which the pulses enter the objective lenses using the mirrors that reflect the pulses before the objective lenses. How this works can be easily explained by means of the 2D example given below.

Before the pump and probe pulses are injected into the objective lenses and focussed onto the sample, they travel as a collimated beam with a small beam waist. Simple ray transfer matrix analysis can therefore be used when calculating how they will be redirected by the objective lenses. Assuming that they enter an objective lens with a defined angle, θ_1 and displacement from the optical axis, x_1, then the displacement from the optical axis, x_2, and angle, θ_2, at which they leave the objective lens can be roughly approximated by multiplying a vector composed of the position an angle by the transfer matrix for a thin lens,

$$\begin{pmatrix} x_2 \\ \theta_2 \end{pmatrix} = \begin{pmatrix} 1 & 0 \\ -\frac{1}{f} & 1 \end{pmatrix} \begin{pmatrix} x_1 \\ \theta_1 \end{pmatrix},$$

where f is the focal length of the lens. At the focal distance of the lens, where the sample will be in focus, the displacement from the optical axis, x_f, and angle, θ_f, of the pulses can be calculated by multiplying the result from the above equation by the transfer matrix for free space propagation when the distance of propagation is the focal length, f.

$$\begin{pmatrix} x_f \\ \theta_f \end{pmatrix} = \begin{pmatrix} 1 & f \\ 0 & 1 \end{pmatrix} \begin{pmatrix} x_2 \\ \theta_2 \end{pmatrix}$$

$$\begin{pmatrix} x_f \\ \theta_f \end{pmatrix} = \begin{pmatrix} 1 & f \\ 0 & 1 \end{pmatrix} \begin{pmatrix} 1 & 0 \\ -\frac{1}{f} & 1 \end{pmatrix} \begin{pmatrix} x_1 \\ \theta_1 \end{pmatrix}$$

$$\begin{pmatrix} x_f \\ \theta_f \end{pmatrix} = \begin{pmatrix} 0 & f \\ -1/f & 1 \end{pmatrix} \begin{pmatrix} x_1 \\ \theta_1 \end{pmatrix}$$

From this, we find that x_f is given by,

$$x_f = \theta_1 f$$

and θ_f is given by,

$$\theta_f = \frac{-x_1}{f} + \theta_1$$

It is clear from this result that the position at which the pulses are focused onto the sample by the objective lens can easily be manipulated simply by changing the angle of the final mirror that reflects the pulse before it enters the objective lens. The angle at which the pulse illuminates the sample is slightly more difficult to control; however, it can also be

manipulated by changing the angle and position at which the pulse enters the objective lens, and this is possible by changing the angle of the mirror before the first mirror.

For simple transmittance and reflectance measurements on thin-films and periodic nanostructures, all of the light collected by the objective lens in front of the sample is relevant to the parameter being measured, and so it can be sent to the photodetector directly without the need for any filtering. When studying photonic integrated devices with photonic waveguides, however, it is necessary to filter the light collected by the objective lens to remove any irrelevant light that will interfere with the light you are trying to measure. For example, in order to measure the transmittance of a waveguide-integrated modulator, it is first necessary to couple the incident probe light into a photonic waveguide using a grating coupler. After the light passes through the modulator, it is then decoupled using another grating coupler and collected by the objective lens. However, because the coupling coefficient of the input grating coupler is not perfect, a large amount of the incident light is reflected at the input grating coupler and collected by the objective lens. This light will interfere with an accurate measurement of the light transmitted by the modulator and thus must be removed before the light is detected by the photodetector.

In order to measure this light, a special filtering system was devised. The spatial filtering system consists of a movable aperture placed between two lenses and is located just before the fibre coupler and the camera imaging system. A schematic diagram of how the spatial filtering system works is shown in Figure 2.3 below. First the probe light is injected into a photonic waveguide device by means of a grating coupler. All of the light collected from the sample, including the light reflected at the input coupler and the light that has passed through the photonic waveguide and been decoupled by the output coupler, is then collected by the objective lens and travels towards the spatial filtering system. The first lens of the spatial filtering system then focusses the light, creating an image plane where a magnified image of the sample is created. The movable aperture is aligned with the location of the output coupler in the image in order to block all of the light except the light emanating from the output coupler. This light can then be imaged by the cameras and detected by the photodetector.

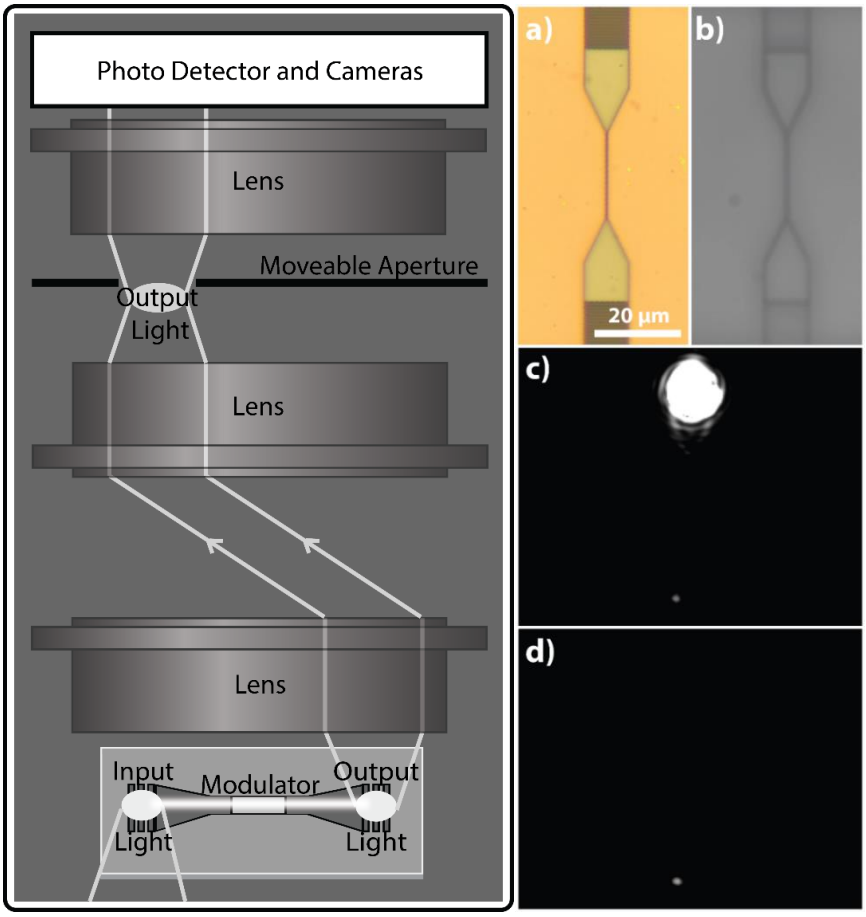

Figure 2.3: Theory and demonstration of spatial filtering. (left) Schematic of how spatial filtering works. (right) a,b) microscope image of a simple Si waveguide with two grating couplers on (a) CMOS camera, and (b) InGaAs NIR camera. c) IR image of 1550 nm light coupled into the structure shown in (a) and (b) from the upper grating coupler and out-coupled from the lower grating coupler. d) Spatially filtered image of c) with only the out-coupled light passing through the moveable aperture.

A demonstration of the spatial filtering process is given in Figure 2.3c and Figure 2.3d. An IR image of a 1550 nm light being coupled into a photonic waveguide through a waveguide coupler at the top and then decoupled through an output coupler at the bottom is provided in Figure 2.3. In Figure 2.3d, a movable aperture is placed in the image plane of the spatial filtering system to block all light except that coming from the output coupler and therefore only light coming from the location of the output coupler can be seen in the IR camera.

2.1.2 Pump-Repump-Probe Spectroscopy

In order to study how fast a material or device can be modulated and the linearity of the modulation response, a pump-repump system where a first pump pulse excites a sample and then a second pump pulse delayed by a specific amount of time then re-excites the sample was also devised. Figure 2.4 illustrates how the pump-repump is achieved.

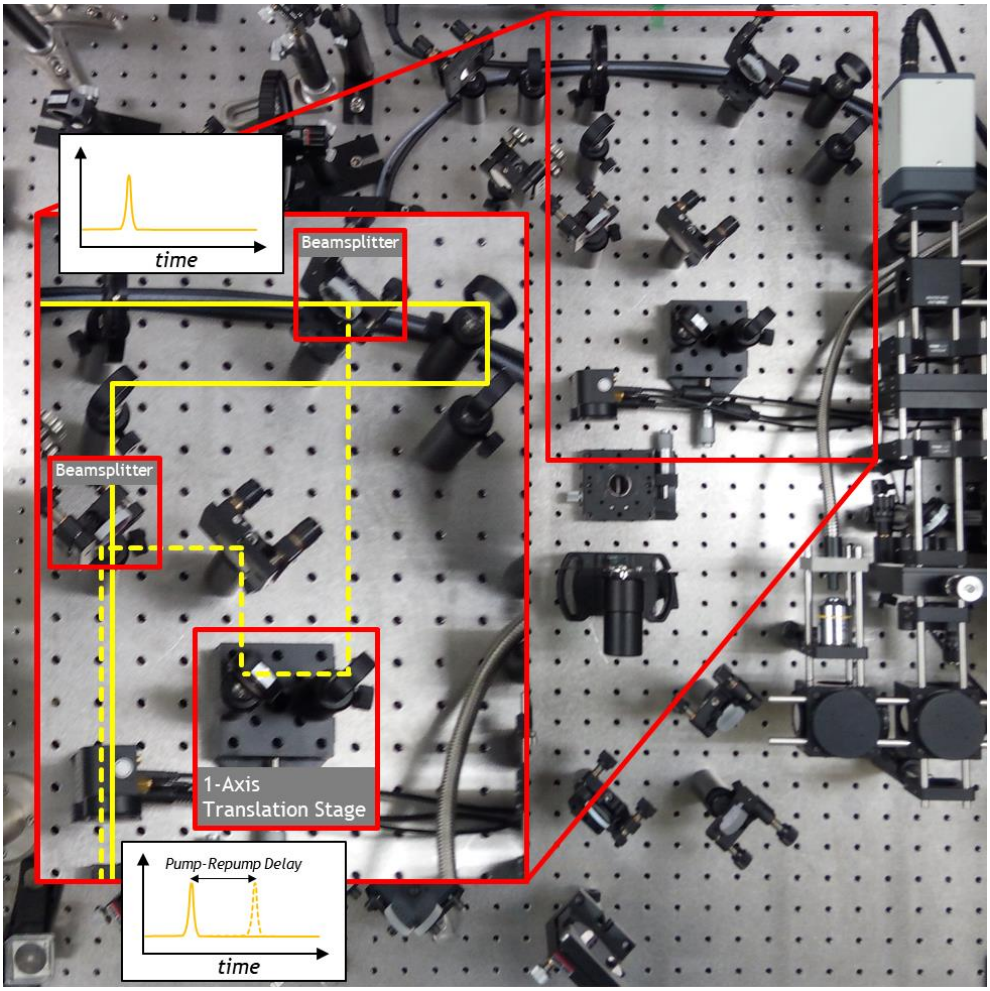

Figure 2.4: Optical setup for splitting off the repump pulse.

Initially, there is a single isolated pump pulse after it is split from the probe pulse by the initial Shortpass Filter seen in Figure 2.1. This pump pulse is split into two pump pulses with equal amplitudes using a 50/50 beam splitter. The primary pump pulse that travels through the beam splitter (solid yellow line) is reflected off of three mirrors and directed downwards towards a second beamsplitter that it is once again transmitted through. The secondary pump pulse that is reflected off the beamsplitter (dashed yellow line) is directed towards two mirrors arranged at 45º and mounted on an adjustable translation stage. By adjusting the position of the translation stage, the optical path travelled by this secondary pump pulse can be increased or decreased to increase or decrease the delay between it and the primary pump pulse without altering the alignment of the pulse in space. Finally, the secondary pump pulse is reflected off another mirror whose angle is adjusted to ensure that the primary and secondary pump pulses are realigned in space. The second beamsplitter then reflects the secondary pulse, and its angle is adjusted to make sure both pulses travel in the exact same direction. The two pump pulses then travel through the same optical path described in section 2.1.

The ability to do pump-repump spectroscopy is not only useful for studying high-speed modulations in all-optical modulator devices, but it can also be used to study the temporal dynamics of a wide variety of non-linear optical processes. For example, it has been demonstrated that pump-repump spectroscopy can be used to examine the photon lifetime of laser cavities based on the non-linear relation between the pump intensity and lasing intensity [61].

2.2 Signal-to-noise Improvement

Throughout the design and assembly of the micro pump-probe spectroscopy setup described in the previous sections, several issues with the setup were confronted. The most difficult issue was the initially extremely poor signal to noise ratio. Because the probe pulse has a duration of only 250 fs, yet the photodetector used to detect the laser pulse has a response time of 70 ps, the electrical signal produced by the detection of the probe pulse is extremely weak compared to the actual laser pulse intensity. This results in the signal to noise ratio of the detected probe signal being very poor.

2.2.1 Noise Propagation

The issue of the poor signal to noise ratio is further compounded by the fact that in this work, the modulation of the probe signal when a sample is excited by the pump pulse, rather than the signal amplitude itself, is of interest. When the probe signal is being measured directly, as seen in Figure 2.5, determining the modulation requires that two separate measurements be made.

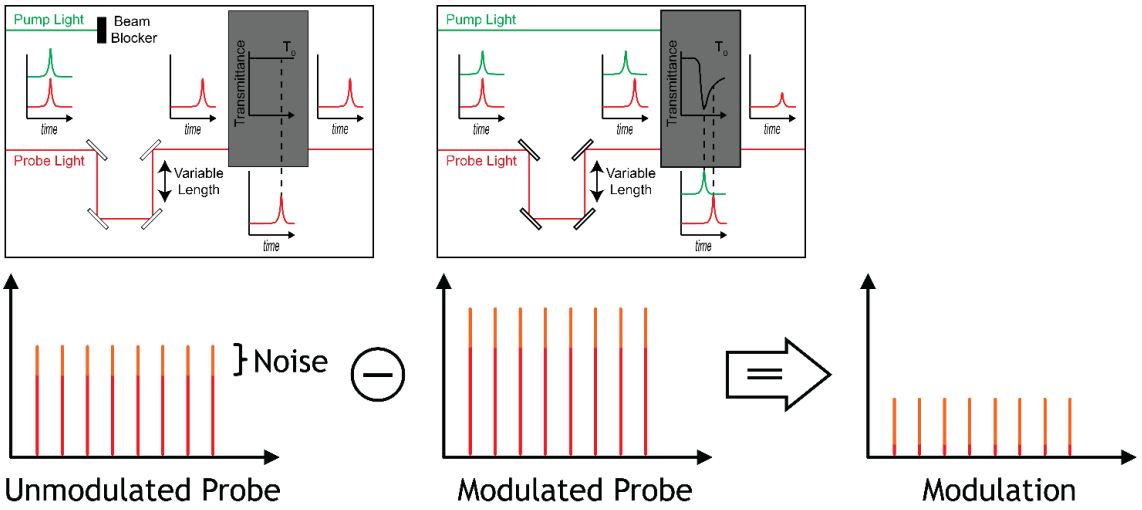

Figure 2.5: Noise propagation in modulation measurement.

First the pump signal is blocked, and the probe signal intensity at each delay is measured. Then, the pump signal is allowed to excite the sample, and the probe signal intensity at each delay is measured. In order to determine the final modulation intensity, the unmodulated signal intensity is subtracted from the modulated signal intensity, according to the following equation,

$$m = b - a$$

where *b* is the modulated probe signal intensity, *a* is the unmodulated probe signal intensity, and *m* is modulated signal intensity. The noise of this calculated modulation can then be determined by using the error propagation equation,

$$\sigma_f = \sqrt{(\frac{\partial m}{\partial a}\sigma_a)^2 + (\frac{\partial m}{\partial b}\sigma_b)^2}$$

$$\sigma_m = \sqrt{((-1)\sigma_a)^2 + ((1)\sigma_b)^2}$$

$$\sigma_m = \sqrt{{\sigma_a}^2 + {\sigma_b}^2}$$

where σ_b is the standard deviation of the modulated probe signal measurement, σ_b is the standard deviation of the unmodulated probe signal measurement, and σ_m is resulting standard deviation of the calculated modulation. From this equation, it is clear that the noise of the calculated modulation is always larger than the noise of both individual measurements, and when measuring extremely small modulations, such as the modulations of ultra-thin thin-films and nanostructures studied in this work, this error will mask the actual modulation being measured and make an accurate measurement impossible.

2.2.2 Differential Transmission Measurement

In order to improve the signal to noise ratio of the measurement, it is desirable to measure the modulation of the probe signal intensity directly rather than calculating it from the unmodulated and modulated probe signal intensities. This can be achieved through the use of an optical chopper and a lock-in amplifier.

An optical chopper is a simple mechanical device that consists of a circular blade with periodically spaced holes that spins at a high frequency. When this device is placed in the path of an optical beam, it will periodically block the beam path creating a chopped signal at the frequency that the optical chopper spins. If such an optical chopper is placed in the path of the pump pulse used in a pump-probe spectroscopy setup, then it will periodically block the pump

pulse, resulting in the probe signal collected from the sample being periodically modulated to produce a mixed signal composed of the unmodulated probe signal and the modulated probe signal, as seen in the bottom left of Figure 2.6. The difference in the intensity of the unmodulated and modulated signals corresponds to the modulation intensity, and therefore, the modulation can be directly measured by determining the intensity of the periodic modulation in the probe signal.

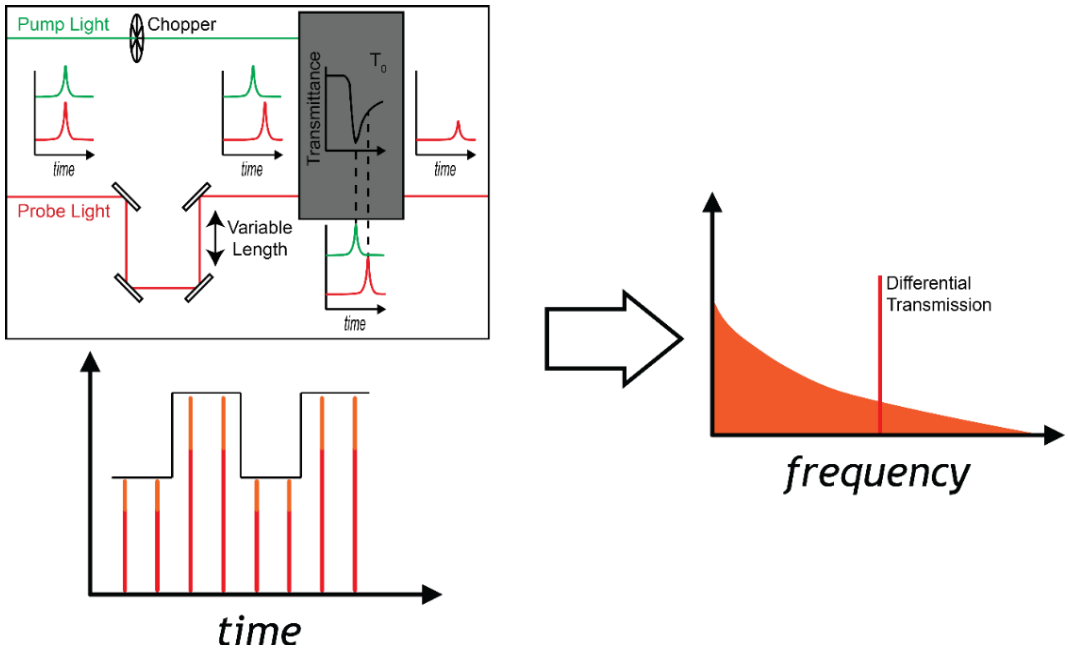

Figure 2.6: Differential transmission measurement using an optical chopper.

Although the periodic modulation has the same noise as the original probe signal, and therefore direct measurement of the modulation would still be difficult, in frequency space, the noise is spread over a large range of frequencies. The periodic modulation, on the other hand, has the same frequency as the chopper, allowing the periodic modulation to be easily isolated from the noise of the probe signal if it is measured in frequency space. By using a reference signal with the frequency of the chopper in a lock-in amplifier, it is possible to isolate the signal at the frequency of the chopper and thus measure the modulation with high precision even when the probe signal noise is comparable to the modulation intensity, as demonstrated in Figure 2.7.

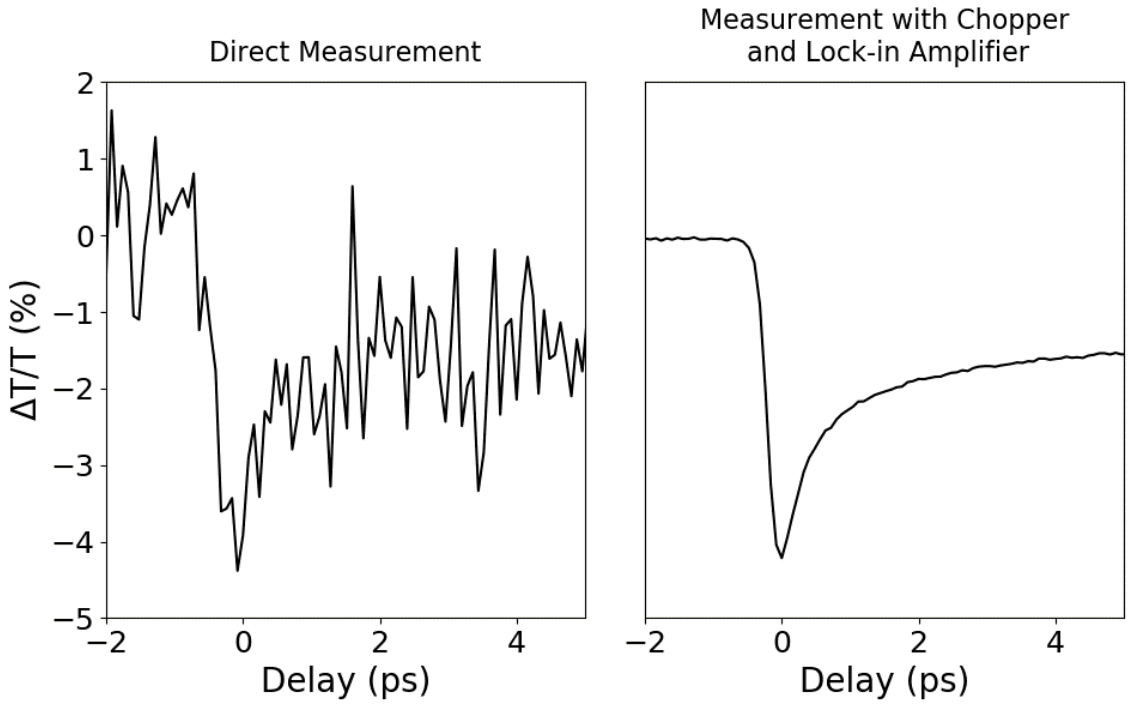

Figure 2.7: Signal-to-noise ratio improvement with chopper and lock-in amplifier. Differential transmission measurement when (left) measuring unmodulated and modulated signal individually, and (right) using a chopper and lock-in amplifier to directly measure the differential transmittance.

2.3 Secondary Reflections

Another difficulty encountered during the assembly of the pump-probe spectroscopy setup was secondary reflections from the optical parts in the setup interfering with the measurement of the femtosecond response of various materials.

In the pump-probe spectroscopy setup, there are a large number of beamsplitters, dichroic mirrors and lenses used. In ordinary uses, the slight imperfections of these components is not a major issue; however, for a very precise measurement such as pump-probe spectroscopy, where the exact timing of the probe pulse is very important, these imperfections can cause major difficulties. For example, beamsplitters are designed to reflect 50 % of an optical signal and transmit the other 50%. For this purpose, they usually consist of a thin metal film on one side of a glass slide that partially reflects light. The light transmitted through this thin metal film is also reflected by the back side of the glass slide. With the use of an anti-reflection coating the intensity of this reflection can be reduced such that it comprises less than 1% of the initial light intensity. This usually allows it to be neglected compared to the 50 % reflected light. When doing a pump-probe spectroscopy measurement, however, this seemingly negligible secondary measurement is a major obstacle.

Because of the additional distance travelled by the secondary reflection (approximately 2.8 times the thickness of the glass slide for a beamsplitter at a 45º angle), there is an additional delay added to the secondary probe pulse, and as such, when the pump-probe response is measured, it will probe the response of the material to a pump pulse even when the primary probe pulse arrives at the material before the pump pulse. For transient responses that last longer than the pump and probe pulses, this will then mask the initial response of the material to the pump pulse, as is demonstrated in Figure 2.8.

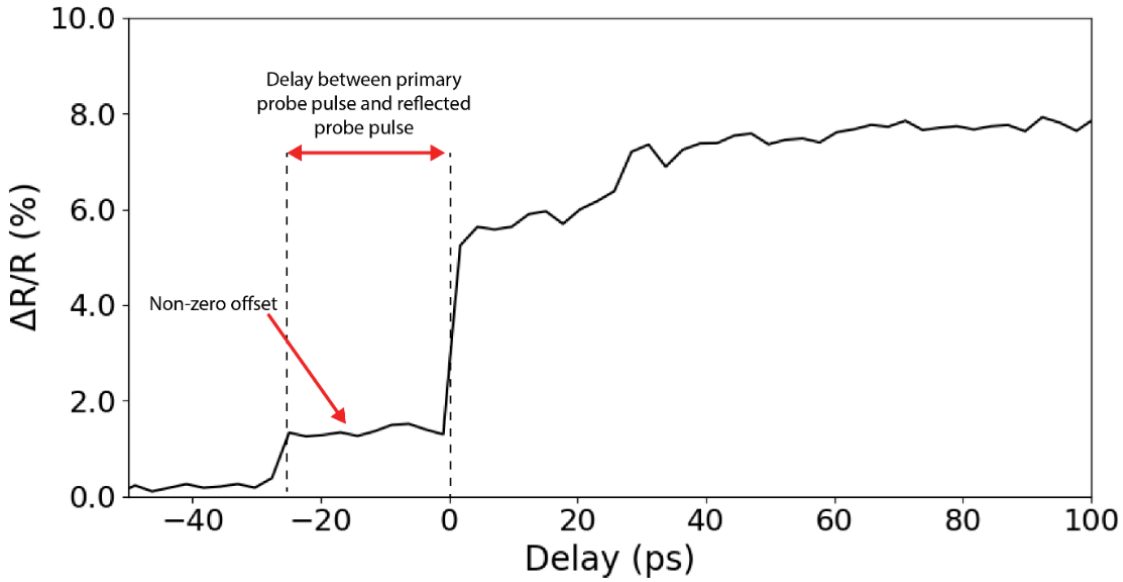

Figure 2.8: Artifacts created by secondary reflections in pump-probe spectroscopy. A secondary delayed probe signal causes a reproduction of the true time-resolved response at an earlier delay, masking any initial dynamics.

To prevent secondary reflections from interfering with the pump-probe spectroscopy measurements, the optical setup must be designed very carefully in order to either prevent the reflections entirely, or at least prevent the secondary reflections from affecting the measurement obtained. One example of such a design consideration was the alignment of the probe light injection for reflectance measurements. In Figure 2.9 two possible configurations of the probe light injection and camera setup are shown.

In the configuration on the left, the camera and detectors are aligned in a straight line with the sample stage, and the probe light is injected into the objective lens from the side using a beamsplitter. This results in both the main probe pulse (solid black line) and a secondary probe pulse (dashed black line) illuminating the sample. As seen in the inset, the two probe pulses will probe the sample at different points in time and probe a different point on the modulation vs. time curve of the material. This is undesirable and is what has happened in Figure 2.8 shown earlier.

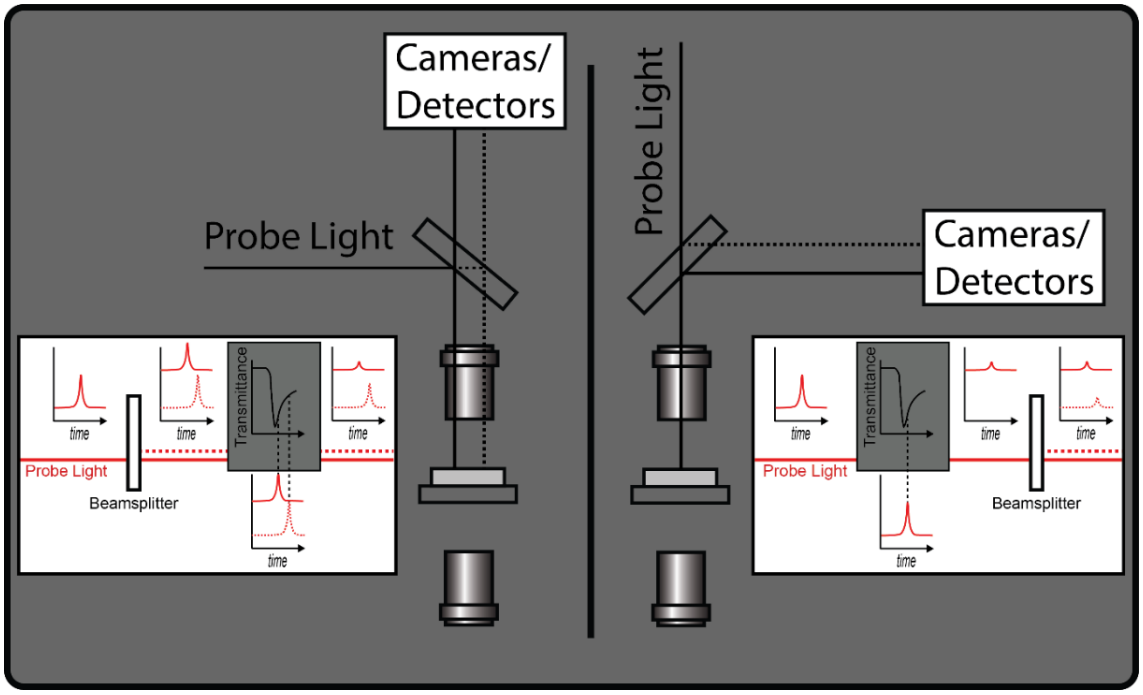

Figure 2.9: Effect of optical setup design on reflection artifacts. (left) the light path when the probe light path is at a 90 degree angle to the optical axis. (right) the light path when the probe light path is along the optical axis. The insets show the resulting signals that are detected by the pump-probe system.

The configuration on the right shows the other possibility, where the probe light is aligned on the same optical axis as the sample and therefore is transmitted through the beam splitter. In this configuration there is only one probe pulse that illuminates the sample, and it probes the modulation of the sample at a single point in time. After being reflected by the sample, it is collected through the objective lens, and then reflected off the beamsplitter towards the camera setup and the photodetector. A secondary reflection is once again created when the light is reflected by the beamsplitter; however, as shown in the inset, the probe pulse of this secondary reflection has the same modulation information encoded in it as the primary pulse, and therefore, it will not affect the measurement of the modulation. There will be a slight ghosting effect due to the secondary offset probe pulse when an image is captured by the camera setup that affects the clarity of the camera image; however, the much weaker intensity of this secondary reflection makes it a minor issue.

Chapter 3 : Fabrication and Characterization of VO_2 and NbO_2 Thin-films

Before any study of the photo-induced modulation of VO_2 and NbO_2 based thin-films, nanostructures or devices can be conducted, it is first essential that the materials can be fabricated with a high-quality and that their structural, chemical and optical properties can be characterized and properly understood. This Chapter provides an overview of the fabrication and characterization techniques used to fabricate, verify and characterize the VO_2 and NbO_2 thin-films used throughout the studies discussed in this thesis.

3.1 Pulsed Laser Deposition

Both Vanadium and Niobium are transition metals that have a large number of possible oxidation states. Because of this, they can form a large number of different oxide components, for example Vanadium can exist in VO, V_2O_3, VO_2, V_2O_5 and many other possible configurations [62]. Niobium can also exist with the same four oxidation states as NbO, Nb_2O_3, NbO_2, and Nb_2O_5 [63]. This large number of possible oxidation states, and the fact that the desired oxides of VO_2 and NbO_2 which exhibit an insulator-metal transition are metastable states at room temperature makes it very difficult to fabricate them using ordinary thin-film fabrication techniques, such as sputtering and e-beam evaporation.

One common technique for fabricating high-quality transition metal oxide thin-films in metastable states is pulsed laser deposition (PLD), a schematic of which is shown in Figure 3.1. In PLD, a target made of the material to be deposited is ablated by a pulsed laser, forming a plasma that is ejected from the target and deposited on a sample substrate held some distance away. When depositing oxides, such as VO_2 or NbO_2, the stoichiometry of the deposited oxide can be precisely controlled by introducing a partial pressure of oxygen gas and elevating the substrate to a precise temperature. This technique allows high-quality oxide films with very precise stoichiometry and has even been used to create epitaxial films under some conditions.

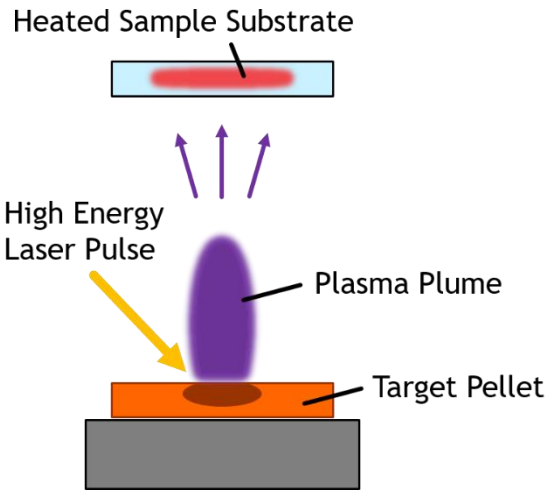

Figure 3.1: Operating principle of pulsed laser deposition.

Both the NbO_2 and VO_2 thin films were deposited on Al_2O_3 C-plane (0001) substrates due to the good crystal match between the NbO_2, VO_2 and Al_2O_3 making high-quality films with good stoichiometry easier to obtain. The PLD system used, pictured in Figure 3.2, uses an ArF laser to ablate targets made of V_2O_5 and Nb_2O_5 for the VO_2 and NbO_2 thin films, respectively. The V_2O_5 targets were made by sintering pellets made of V_2O_3 powder at 600 ºC for 12 hours under atmospheric pressure, while the Nb_2O_5 pellets were made by sintering pellets of Nb_2O_5 at 1200 ºC for 6 hours. The fabrication of both VO_2 and NbO_2 using PLD is well reported in the literature, and so the initial deposition parameters, such as the substrate temperature and oxygen gas pressure during deposition were extracted from literature and used in a first fabrication attempt of the two thin-film materials.

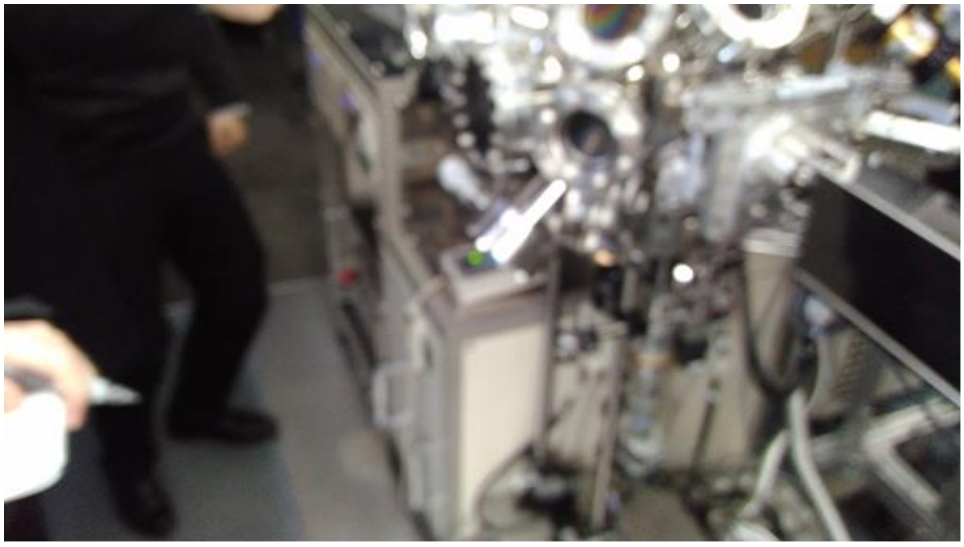

Figure 3.2: PLD system used for the fabriation of NbO_2 and VO_2 thin-films.

3.2 Film Characterization

3.2.1 X-ray Photoelectron Spectroscopy and X-Ray Diffraction

Based on values reported in the literature, an oxygen pressure of 2.5 Pa and a substrate temperature of 450 ºC was initially used to attempt to fabricate a VO_2 thin-film on Al_2O_3 [64]. To verify the stoichiometry of the deposited material, x-ray photoelectron spectroscopy (XPS) was then performed to probe the oxidation state of the vanadium ions in the material. In XPS, an X-Ray source is used to eject electrons from the orbitals of the constituent atoms in a material. The kinetic energy of the electrons is then measured and from this the energy level of the different atomic orbitals determined. Because of the different electrostatic interactions between atoms in oxides with different stoichiometries, the energy of the atomic orbitals can be used as a measure of the oxidation state of a given material. For example, the 2p2/3 orbital of vanadium has an energy of 513 eV [62]. This changes to 515.2 for V_2O_3, 515.6 for VO_2, and 516.9 for V_2O_5 [62].

When XPS was performed on the thin-film fabricated using deposition conditions found in the literature [64], it was found that the stoichiometry of the deposited film corresponded to V_2O_5, instead of VO_2 (Figure 3.3). From this, it was clear that the deposited thin-film was over-oxidized and the oxidation of the material needed to be decreased by varying the deposition parameters. It is well known that both a higher oxygen pressure and lower substrate temperature result in the deposited film being more oxidized, and therefore, these parameters were varied to reduce the oxidation state of the vanadium and obtain VO_2 [64]. Figure 3.3 shows a comparison of the XPS spectra for different deposition conditions. After optimization, a thin-film with a VO_2 stoichiometry was obtained for an oxygen pressure of 1.1 Pa and a substrate temperature of 500 ºC.

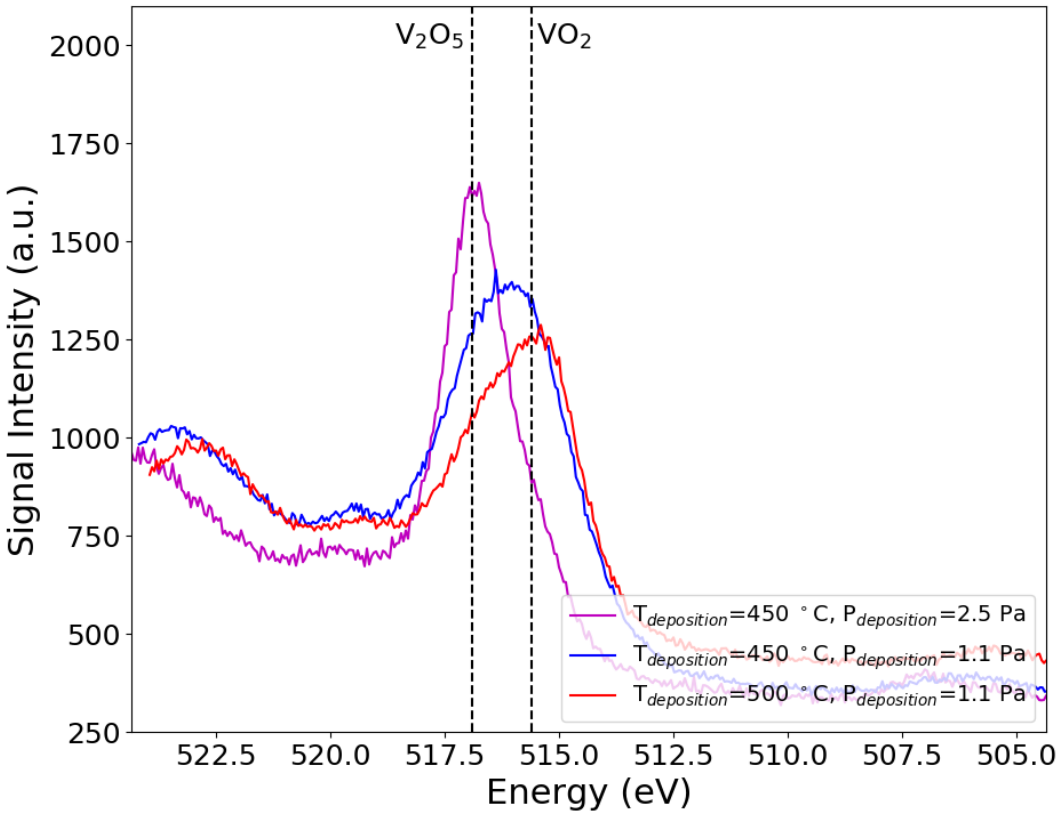

Figure 3.3: XPS spectra of PLD fabricated vanadium oxides.

It was later found that although a high-quality VO_2 thin-film could be obtained under these deposition conditions, due to the metastable nature of the VO_2 state, it would gradually oxidize over time to the thermodynamically stable V_2O_5. This can be clearly seen in Figure 3.4, where the XPS spectra of a freshly fabricated sample and a 2 month old sample are compared. From this it was understood that in a final device structure, the VO_2 would need to be protected by a capping layer such as Al_2O_3. For the thin-film study presented in this chapter, recently fabricated samples were used.

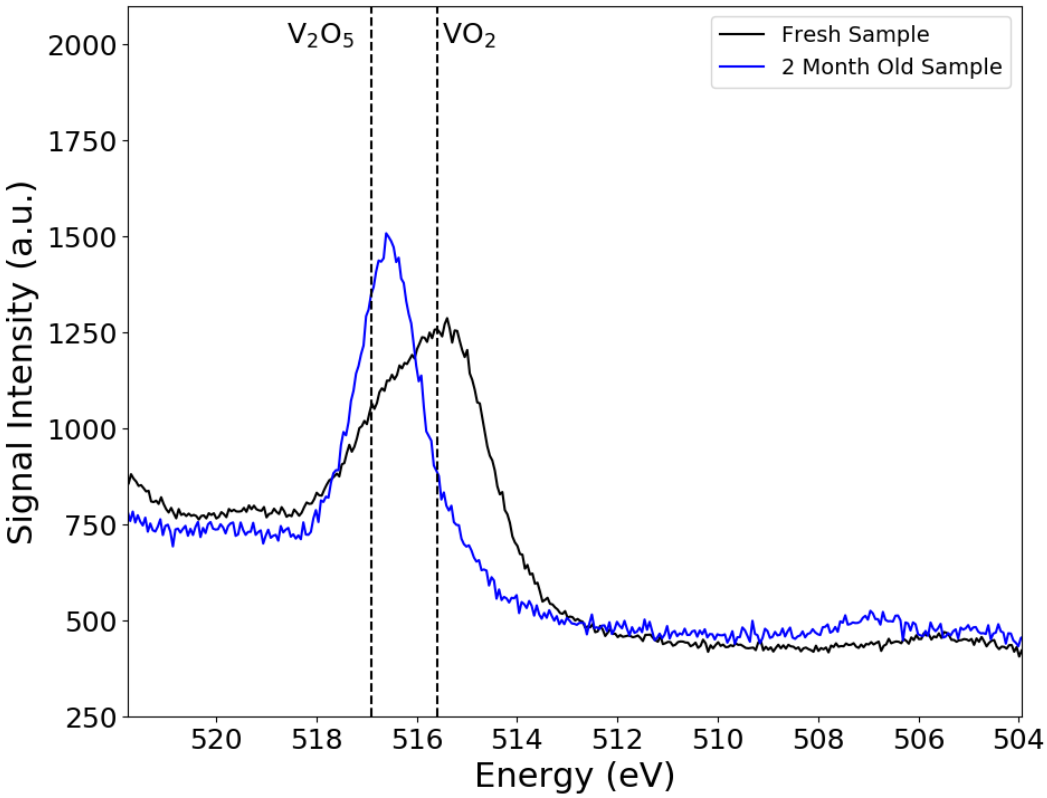

Figure 3.4: XPS Spectra of freshly fabricated VO_2 sample oxidized sample.

Because the insulator metal-transition of VO_2 is related to its semiconductor band structure, which is a result of its monoclinic crystal structure, in addition to verifying the stoichiometry of the VO_2 thin-film, it was also necessary to confirm that the deposited film had the crystal structure of the low-temperature monoclinic VO_2 phase. This was performed by using x-ray diffraction in the 2θ-ω mode of operation. A 40 nm VO_2 thin-film was fabricated on Al_2O_3, and the corresponding XPS spectrum for the $V_{2p2/3}$ orbital and the 2θ-ω spectrum of the sample are shown in Figure 3.5a and Figure 3.5b, respectively. The XPS spectrum shows a clear peak at 515.6 eV, [62] corresponding to VO_2, and the XRD spectrum shows peaks at 39.85º and 41.65º. The peak at 41.65º corresponds to the (0001) plane of the Al_2O_3 and is to be expected. The peak at 39.85º on the other hand corresponds to the (020) plane of the monoclinic phase of VO_2 [65]. It is important to note that no other monoclinic VO_2 peak is observed. This indicates that the growth of the VO_2 crystal is highly directional, and the (020) plane is the only one parallel to the sample surface, and thus able to reflect the incoming X-rays, across the entirety of the sample. Additionally, the VO_2 adjacent to the substrate will have its crystal phase locked as in an epitaxial film, and therefore the conclusions of this thesis should only be taken to relate to epitaxially deposited films.

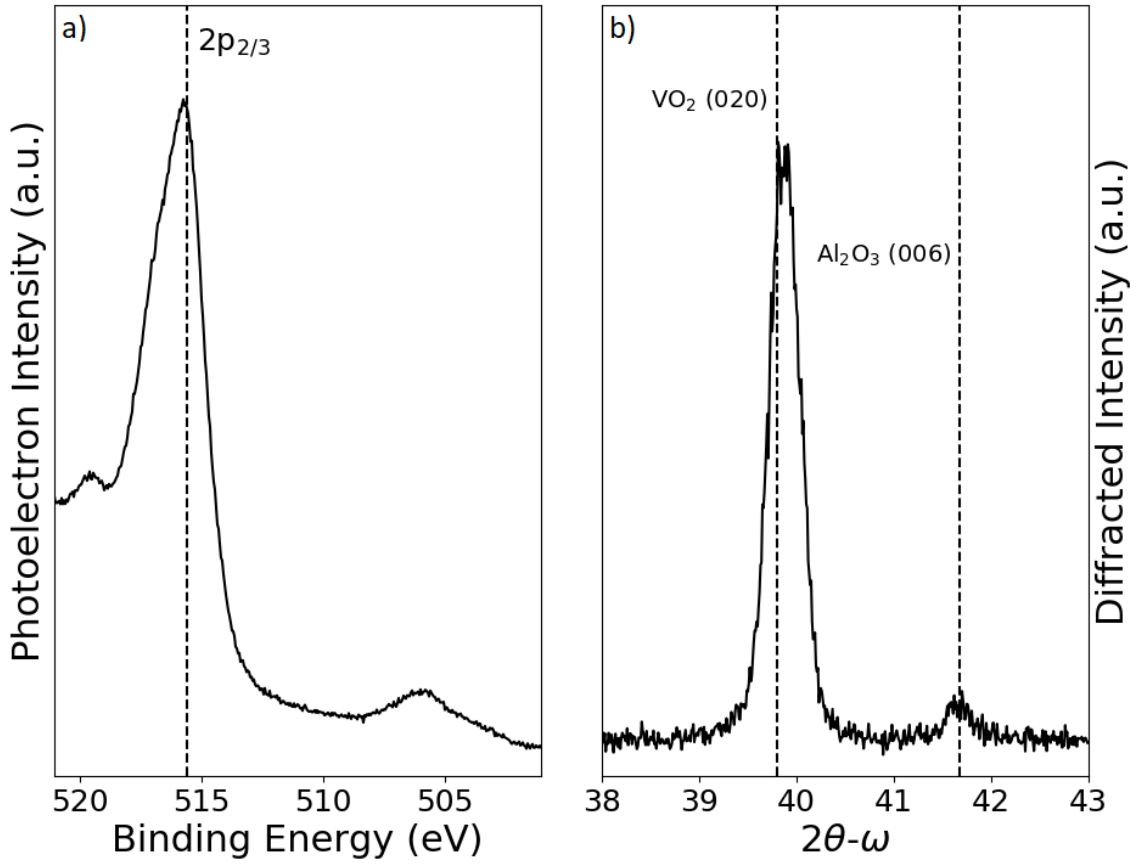

Figure 3.5: XPS and XRD spectra of PLD fabricated VO_2 thin-film. (a) XPS spectrum of the VO_2 the $2p_{2/3}$ peak of VO_2 overlaid on the spectrum. (b) XRD spectrum of VO_2 measured using the 2θ-ω method, with the (020) diffraction peak of VO_2 and the (006) peak of Al_2O_3 labelled.

The deposition conditions of NbO_2 were optimized by Prof. Matsui from the department of Electrical Engineering. They were found to be 550 ºC for the substrate temperature and $1x10^{-3}$ Pa for the oxygen pressure. A 60 nm NbO_2 thin-film was fabricated under these conditions, and its XPS and XRD spectra are shown in Figure 3.6a and Figure 3.6b, respectively. A clear match between the XPS spectrum of the sample and the $3d_{5/2}$ orbitals and $3d_{3/2}$ orbitals of NbO_2 were observed [66]. From the XRD results, a clear and sharp diffraction peak can be seen at a 2θ value of 37.28º, which matches well with the (440) peak of the low-temperature body-centred tetragonal phase of NbO2 [33]. The lack of any other NbO_2 peaks in the XRD spectrum once again suggests highly directional growth of the NbO_2 crystal. Similar to the VO_2 thin-film this indicates semi-epitaxial growth, and the conclusions should only be applied to epitaxially deposited films.

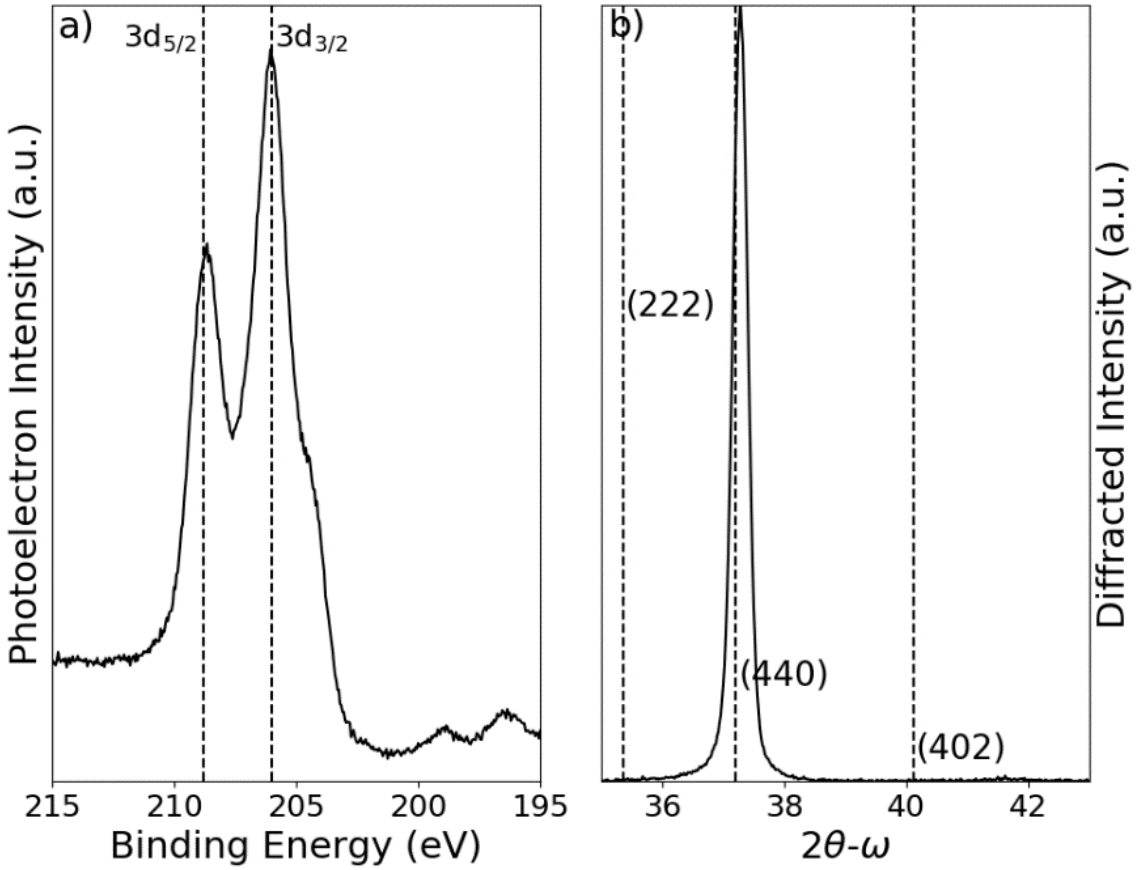

Figure 3.6: XPS and XRD spectra of PLD fabricated NbO_2 thin-film. (a) XPS spectrum of the NbO_2 with the $3d_{5/2}$ and $3d_{3/2}$ peaks of NbO_2 overlaid on the spectrum. (b) XRD spectrum of NbO_2 measured using the 2θ-ω method, with the (220), (440) and (402) diffraction peaks of NbO_2 and labelled.

3.2.2 X-Ray Reflectance

The thicknesses of the various deposited films were determined using X-Ray Reflectance (XRR).

When an X-Ray is incident on a thin-film structure, in the same manner as visible light, the X-Ray will be reflected at the interface between the sample and air and the sample and the substrate. The X-Rays reflected from these two interfaces will interfere with each other resulting in constructive or destructive interference depending on their optical path difference. The optical path difference is dependent on the refractive index of the material (at the X-Ray wavelength, the incident angle and the thickness of the film [67].

XRR is a technique similar to reflectometry, where the reflectance of an X-Ray beam by a sample is measured for varying angles of incidence. The resulting reflectance vs. incident angle curve is fit to a model of the sample and the thickness, density and roughness of the layers of the sample can be determined by optimizing the fit of the model and the measured X-Ray

reflectance [67]. An example of the X-Ray reflectance measurement and fit model is provided in Figure 3.7.

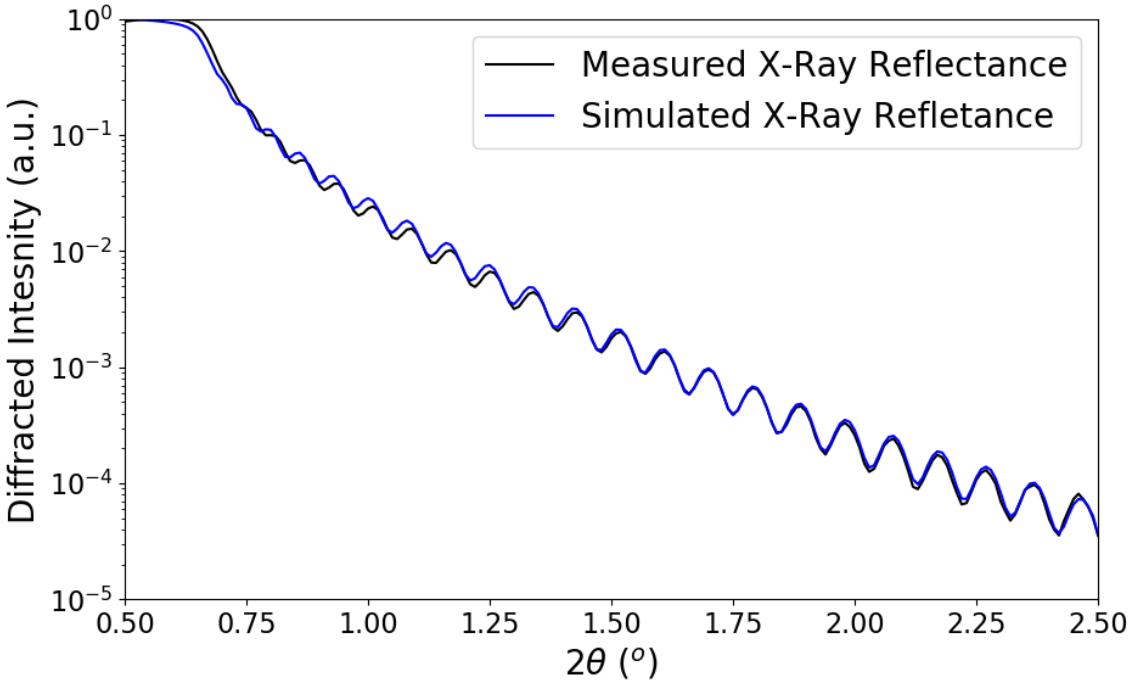

Figure 3.7: X-Ray Reflectance measurement of an NbO_2 thin-film. The simulated and measured x-ray reflectance are plotted, clearly showing interference bands as the angle of incidence is varied.

Using this method, the thickness of the VO_2 thin-film studied in the following section was determined to be 42 nm, and the thickness of NbO_2 thin-film was determined to be 60 nm.

3.2.3 Spectroscopic Ellipsometry

In order to be able to properly analyze the photo-induced modulation of the optical properties of the VO_2 and NbO_2 thin-films, it is essential that their initial steady state optical properties are well understood. The simulation and optimization of nanophotonic devices and structures also requires that the refractive index of all of the constituent materials be well known. For these reasons, it was necessary to determine the refractive indices of the VO_2 and NbO_2 thin-films fabricated using PLD. This was achieved using spectroscopic ellipsometry.

Spectroscopic ellipsometry is a technique that can be used to extract the structure and optical properties of a thin-film or multilayer sample from the reflectance of the sample. First the reflectance of TE and TM polarized light from the sample is measured over a broad wavelength range and for a variety of incident angles. A model that can be used to predict the reflectance of the structure is then defined, and the model parameters are optimized to match the measured reflectance of the sample to the simulated reflectance obtained from the model. The model itself is can be quite complex, as it defines the number of layers in the sample, order

of the layers, and the refractive index of each individual layer in the material. For a simple thin-film structure, the thickness of the layer and the refractive indices of the ambient medium, substrate and the sample must all be defined.

For the VO_2 and NbO_2 thin-films measured in this study, the substrate and ambient refractive indices were known to be the refractive indices of air and sapphire, respectively, and the thicknesses of the films were determined by X-Ray Reflectance as discussed earlier. Therefore, only the refractive indices needed to be modelled. For both VO_2 and NbO_2, there is no significant conductivity in the insulating state, and so the refractive index was modelled by several Lorentz oscillators to represent the different absorption bands of the two materials. Using this as a basis, the fitting process was able to match the measured reflectance and simulated reflectance quite well, and the refractive index of the two films could be determined.

Figure 3.8 shows the refractive index extracted through spectroscopy ellipsometry for the VO_2 thin-film.

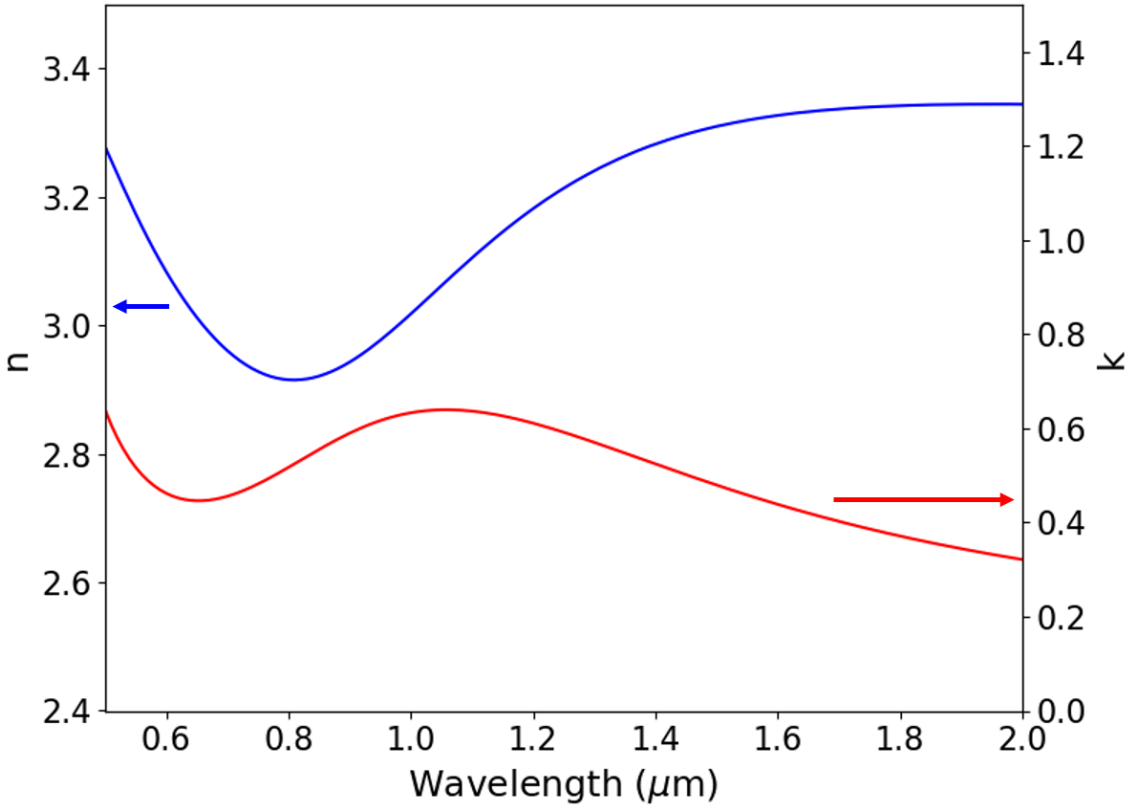

Figure 3.8: Refractive index of VO_2 thin-film as measured by ellipsometry.

In Figure 3.9, the refractive index of NbO_2 as determined by spectroscopy ellipsometry is shown.

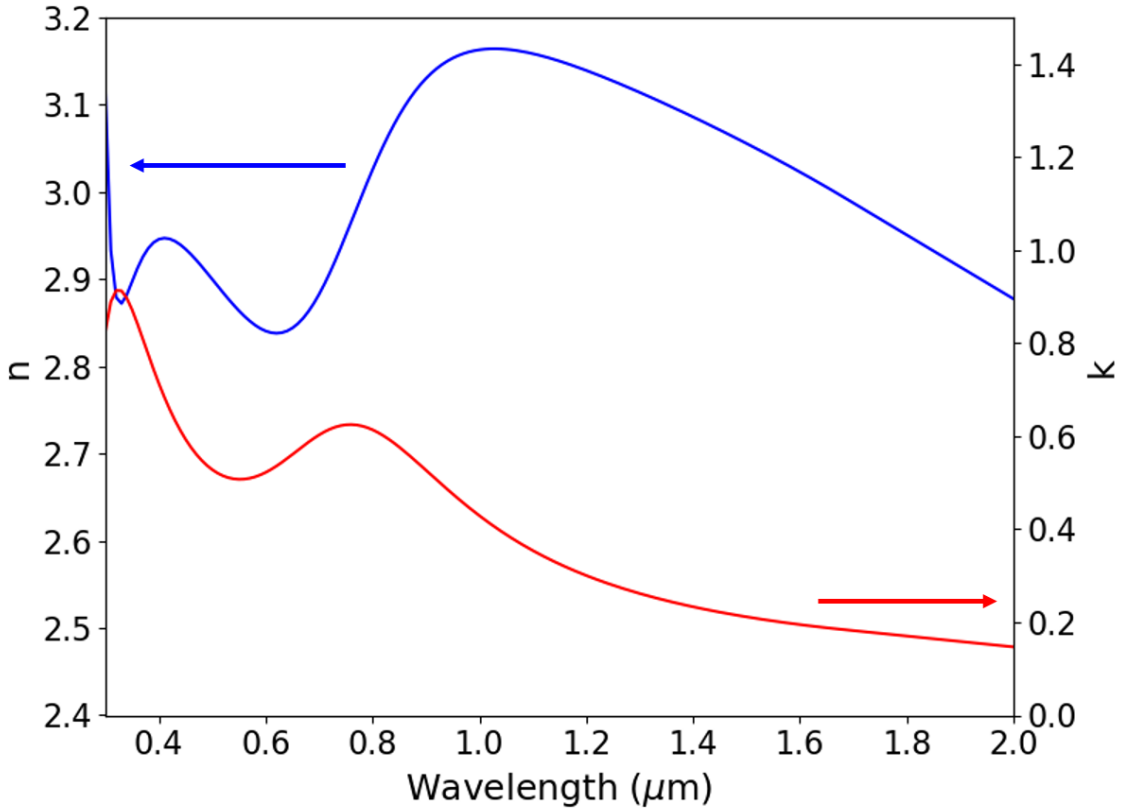

Figure 3.9: Refractive index of VO_2 thin-film as measured by ellipsometry.

Chapter 4 : Photo-induced Modulation of VO_2 and NbO_2 Thin-Films

In order to develop a deeper understanding of the photo-induced IMT of insulator-metal transition materials and in particular whether the high-speed modulation and recovery of IMT materials can be achieved by means of a purely electronic IMT, as has been proposed, in this Chapter, I investigate the photo-induced modulation of VO_2 and NbO_2 thin-films. The low pump fluence region, where a fast ps timescale modulation and slow ns timescale modulation have been observed for these materials is particularly focussed on in order to elucidate the nature of the slow ns timescale modulation and whether or not it is related to an IMT as has been proposed in the past.

The extremely low noise level of the micro pump-probe spectroscopy setup described in Chapter 2 enables the precise study of the photo-induced modulation of NbO_2 and VO_2 thin-films at pump fluence levels far below those studied by other groups. This makes it possible to determine if there exists a threshold for the slow ns timescale modulation, and therefore, if the slow ns modulation truly corresponds to a non-linear IMT process. The linearity of the slow ns modulation response is further studied using the pump-repump capabilities of the system.

A previously unknown mid-fluence regime where VO_2 exhibits a non-linear photo-induced modulation while exhibiting a fast recovery is also uncovered. The connection between this fast recovery mid-fluence region and the newly discovered monoclinic metal state of VO_2 found by other groups is also discussed.

4.1 VO_2

As VO_2 is more widely studied and better understood than NbO_2, the photo-induced modulation of VO_2 was first studied.

4.1.1 Pump-Probe Response

The modulation of the transmittance and reflectance of the 42 nm VO_2 sample was measured for three different pump fluences, the results of which are shown in Figure 4.1. In both the transmittance (Figure 4.1a) and reflectance (Figure 4.1b) measurements, two distinct phenomena are observed, a short-lived modulation on the ps timescale, and a long-lived modulation with a varying timescale and slope depending on the pump fluence. It is common in studying transient phenomena to fit the response to an exponential decay curve. Because

there are two clear phenomena, the VO_2 response was fit to a two-exponential decay curve given by the following equation,

$$\frac{\Delta I}{I} = A_0\left(1 + erf\left(\frac{t-t_0}{\tau_p}\right)\right)\left(A_1 e^{\frac{t-t_0}{\tau_1}} + A_2 e^{\frac{t-t_0}{\tau_2}}\right)$$

where $\frac{\Delta I}{I}$ corresponds to $\frac{\Delta T}{T}$ for the transmittance measurement and $\frac{\Delta R}{R}$ for the reflectance measurement, t_0 is the delay of the pump pulse, t_p is the duration of pump pulse, A_1 and t_1 are the intensity and recovery time constant of the ps timescale modulation, and A_2 and t_2 are the intensity and recovery time constant of the slow modulation. For all pump fluences, except the highest pump fluence where only a modulation steadily increasing in time is observed, the fast ps modulation is observed to have a recovery rate of approximately 1 ps and manifests as a decrease in the transmittance of the VO_2 and an increase in the reflectance. This phenomenon has been observed before in the literature and is generally described as resulting from a transient increase in the metallization of the VO_2. The nature of this metallization, and whether it is due to photo-excited free carriers in the conduction band of VO_2 or a purely electronic IMT resulting in a true metal band structure forming, however, is still debated.

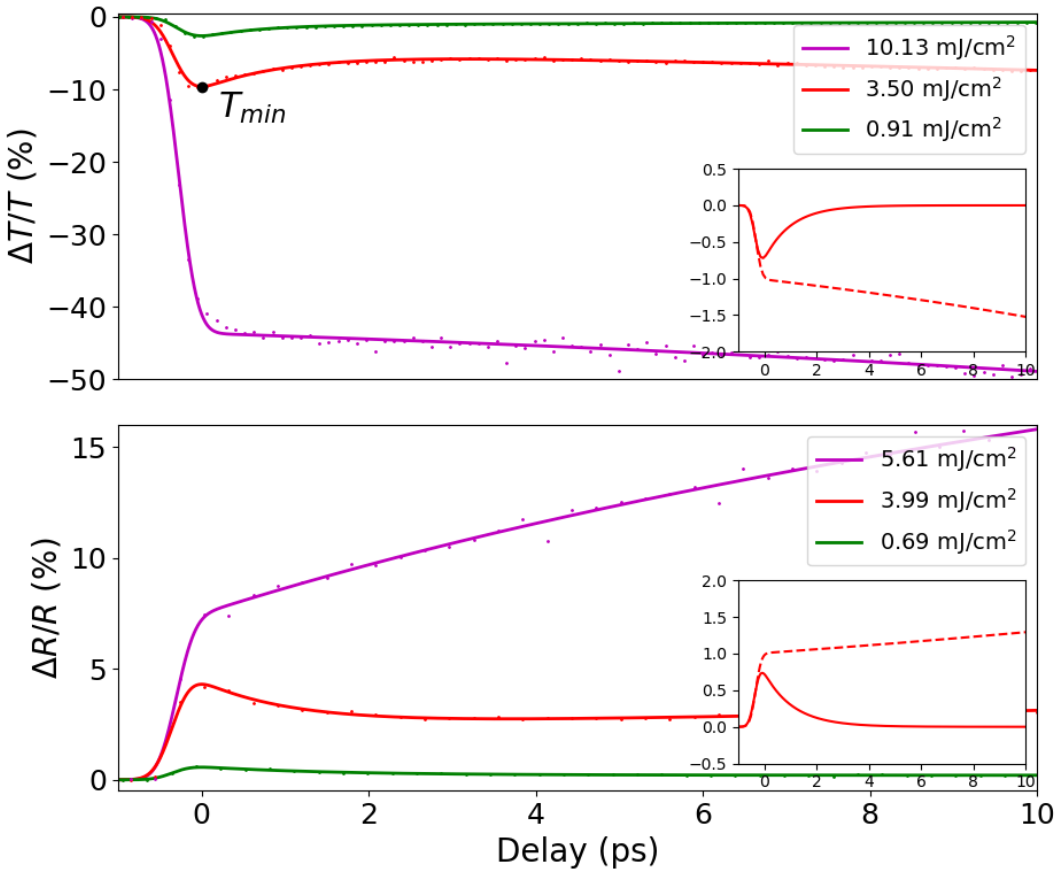

Figure 4.1: Modulation of VO_2 after excitation by a femtosecond pump pulse. The time-resolved photo-induced modulation in the transmittance (top) and reflectance (bottom) of VO_2 after excitation by a femtosecond laser pulse. Insets show the short-lived and long-lived components of the response for the red curves.

Unlike the short-lived modulation, whose recovery rate is independent of the pump fluence, the slow modulation has a far more complex behaviour. For low pump fluences, such as for the green curves in Figure 4.1, the modulation decays with a recovery time constant consistently around 600 ps. When the pump fluence is increased above a specific threshold – later found to be 1.47 mJ/cm^2, as shown in Figure 4.2 – the recovery time constant becomes negative, indicating that that the modulation is increasing over time as opposed to decreasing. Finally, at the highest pump fluences, the slow modulation dominates the response, with the modulation continuing to increase over time. For even higher pump fluences, which were not obtainable using the laser used here, it has also been shown that a full modulation that does not further increase saturates at a maximum value and does not increase over time can be observed [50].

The changing behaviour of the slow modulation clearly represents a non-linearity in the photo-induced response of the VO_2. As discussed in Chapter 1, this behaviour is commonly attributed to the photo-induced IMT and CPT of VO_2 to the high-temperature rutile phase in individual crystal grains, with the gradually increasing modulation being attributed to the spread of the rutile phase to neighbouring grains of VO_2.

4.1.2 Modulation vs Pump Fluence

To better understand the dynamics of the transient modulation of VO_2, the modulation in the transmittance at the minimum of the short-lived response, T_{min}, 100 ps after the pump pulse, T_{100ps}, and 1 ns after the pump pulse T_{1ns}, were measured for various pump fluences and then plotted against pump fluence in Figure 4.2. Three distinct features of interest can be observed in this Figure: the linearity of the modulation at the short-lived response minimum, the persistence of the slow modulation even for extremely low pump fluences, and the two thresholds corresponding to a non-linearity in the slow modulation at 1.47 mJ/cm^2 and a change in the ratio of the modulation at 1 ns and 100 ps at 4.00 mJ/cm^2.

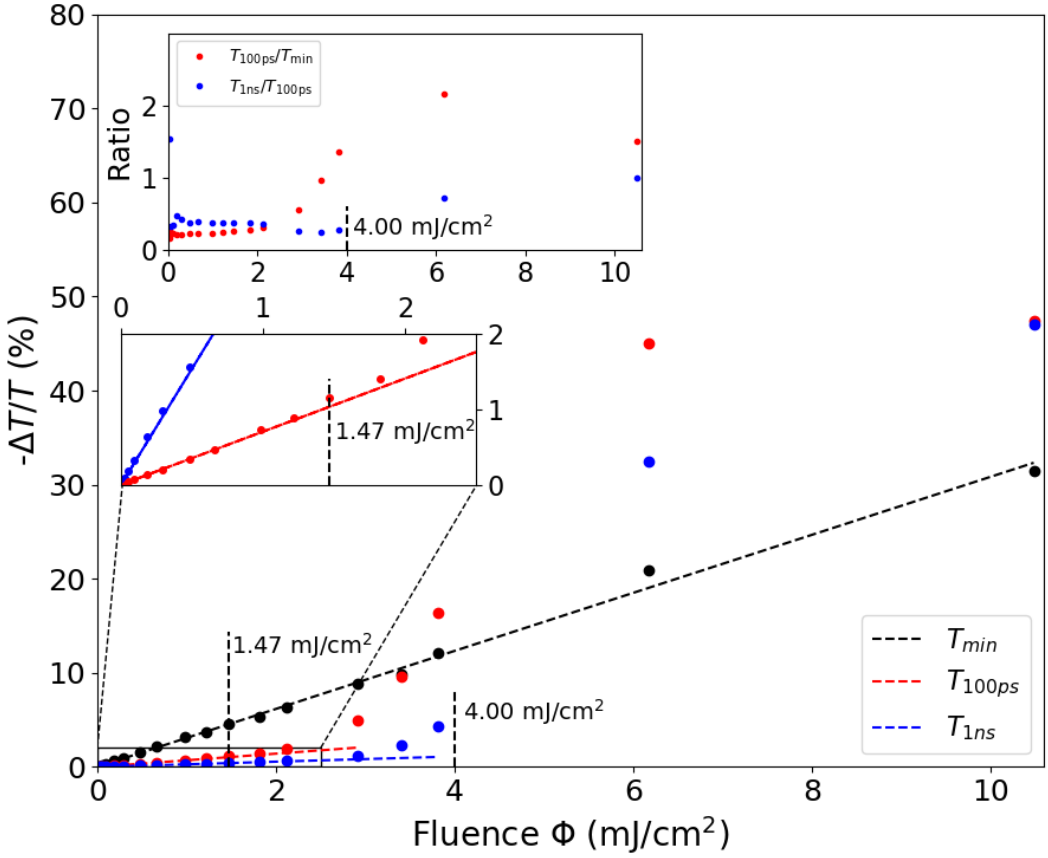

Figure 4.2: Change in modulation of VO_2 with fluence at minimum. The change in the modulation of the transmittance at the minimum of the short-lived response, 100 ps after the minimum and 1 ns after the minimum are plotted against pump fluence. (lower inset) Zoomed in image of the low-pump fluence region for the modulation at 100 ps and 1 ns. (upper inset) ratio of the modulation at the minimum and 100 ps and ratio of the modulation at 1 ns and 100 ps plotted against pump fluence.

The first feature that can be noticed from Figure 4.2 is the linearity of the response at the minimum of the fast response. The modulation at the minimum of the fast response (black points) follow closely to a line of best fit plotted through the pump-probe response (dashed black line). Only minor deviation from the line of best fit is seen for high pump intensities. The deviation can be attributed to either noise in the signal measurement or the measurement being taken at a delay slightly after the minimum of the fast response and, therefore, also including some contributions from the long-lived response. The linearity is observed for pump fluences ranging from as low as 21 μJ/cm^2 to as high as 10.49 mJ/cm^2. The line of best fit found for the data points also crosses through the origin, suggesting that no threshold exists for the short-lived response either and that it originates from a continuous linear phenomenon. This result contradicts recent proposals that the short-lived response may originate from a purely electronic IMT [52]. Possible origins for this response are discussed in the following section, 4.1.3.

Another feature of interest is the persistence of the long-lived modulation even for extremely low pump fluences, as well as the linearity of this low pump-fluence region. For the

low fluence region below 1.47 mJ/cm^2, both the modulation at 100 ps and 1 ns after the pump pulse scale linearly with the pump fluence with no evidence of a threshold, even for extremely low pump fluences, as can be seen in lower inset of Figure 4.2. From the upper inset of Figure 4.2, it can also be seen that the ratio of the modulation at the short-lived modulation minimum and 100 ps is constant in the low-fluence region. This is a further indication that both phenomenon are scaling linearly with pump fluence and exhibit no threshold for their onset. Once again, this disagrees with the common explanation of the long-lived modulation as being a result of the IMT being induced in individual grains of VO_2. The IMT is a non-linear process where the photo-excited carrier density reaches a critical threshold and then causes a collapse of the bandgap, drastically increasing the conductivity of the VO_2 and thus increasing its IR reflectance and decreasing its IR transmittance. Section 4.1.4 discusses the origin of the low-fluence long-lived modulation.

The final feature of interest is the presence of two thresholds in the long-lived modulation observed at 1.47 mJ/cm^2 and 4 mJ/cm^2. Because of the changing scale, it is difficult to discern the threshold at 1.47 mJ/cm^2 from the main plot; however, from the zoomed in plot shown in the lower inset, it is clear that the measured modulation at 100 ps (red points) deviates from the line of best fit for the low-fluence region at approximately 1.47 mJ/cm^2. Above 1.47 mJ/cm^2, both T_{100ps} and T_{1ns} deviate from their linear response and drastically increase in value with increasing pump fluence. This suggests a non-linear process, such as the onset of an IMT in the VO_2 thin-film as previously proposed by others. The gradually increasing long-lived modulation as seen on the short-timescale in Figure 4.1 can likely be explained by the spread of the propagation of a metallic phase nucleated in single grains to neighbouring grains.

From the upper inset of Figure 4.2, the ratio of the modulation at 100 ps and 1 ns can be seen to remain unchanged initially, even after the onset of the first threshold at 1.47 mJ/cm^2. This indicates that the rate of recovery of the short-lived modulation between 100 ps and 1 ns initially remains unchanged for a mid-fluence region between 1.47 mJ/cm^2 and 4 mJ/cm^2. Only after 4 mJ/cm^2 does the rate of recovery decrease and the duration of the long-lived modulation begin to increase. This suggests that as opposed to the simple model of an IMT and CPT being triggered at the lower threshold, a more complex two-step process may be present. An in depth analysis of this region is given in section 4.1.5.

4.1.3 Nature of the Short-Lived Modulation

The fact that the short-lived modulation of VO_2 scales linearly with pump fluence and shows no evidence of a threshold at low pump fluences suggests that the phenomenon is not due to an IMT. The ps timescale of the recovery of the short-lived response also hints that the phenomenon is related to the presence of photo-excited electrons in the conduction band and holes in the valence band of VO_2, as the relaxation of photo-excited carriers in semiconductor materials is usually on the order of several to 10s of ps. In order to better understand the physical processes at play in the short-lived modulation shown by VO_2, and if the observed modulation can be explained by the presence of photo-excited carriers, the effect of photo-excited carriers on the band-structure and optical properties of VO_2 was modelled.

When electron-hole pairs are excited in semiconductor materials, three distinct changes in the electronic structure of the materials that affect their optical properties are known to occur [14]. The first is a band filling effect, where the presence of excited electrons in the conduction band and excited holes in the valence band of the material prevents the excitation of further electron-hole pairs, decreasing the absorption coefficient of the material in the vicinity of the band gap. Another related effect is band shrinkage. Band shrinkage occurs due to large densities of excited carriers screening the lattice charge and forming an electron-hole plasma that has a finite binding energy. This lowers the energy of the excited electrons and holes and thus reduces the band gap, causing an increase in the absorption coefficient near the band gap [14]. Because causality requires that the real part of the refractive index, n', and the absorption coefficient of a material be related by the Kramer-Kronig's relation [12],

$$n' = 1 + \frac{c_0 \hbar}{\pi q_e} PV \int_0^\infty \frac{\alpha(E')}{E'^2 - E^2} dE'$$

the two phenomena above also result in a change in the real refractive index of the semiconductor material. Finally, the excitation of additional free carriers in the semiconductor material will also increase the conductivity of the material. This will cause an increase in the plasma frequency of the Drude component of the material's dielectric response.

In calculating the first two effects, first a model of how the absorption coefficient changes with energy (or wavelength) and how it relates to the band gap of the VO_2 is needed. VO_2 is an indirect bandgap material, and indirect bandgaps are known to have an absorption profile that follows the following equation [68]

$$\alpha(E) = \frac{(E - E_G + k_B\Theta)^2}{e^{\frac{\Theta}{T}} - 1} + \frac{(E - E_G - k_B\Theta)^2}{1 - e^{\frac{-\Theta}{T}}}$$

where E is the photon energy at which the absorption coefficient is being measured, E_G is the band gap, k_B is the Boltzmann constant, Θ is the phonon temperature of the phonon necessary to provide the momentum difference between the valence band maximum and conduction band minimum, and T is the lattice temperature [68]. Using the refractive index data extracted from the VO_2 thin-film and the fact that the imaginary part of the refractive index, n'', has the following relation to the absorption coefficient, α, and the wavelength, λ [12],

$$\alpha = 4\pi n''/\lambda$$

it was possible to fit the absorption coefficient of VO_2 to the above model and extract the band gap and phonon temperature of VO_2.

4.1.3.1 Band-Filling

Next, the band-filling effect was calculated. The band-filling effect, sometimes called Pauli blocking effect, is a result of the fermionic nature of electrons. When electrons are photo-excited from the valence band to the conduction band of a semiconductor, they occupy states in the conduction band of the material, and this prevents the excitation of another electron to the same state. In the same manner, when an electron is excited it leaves behind a hole, meaning that no electron exists to be excited from this level. Therefore, in order to calculate the effect of band-filling on the absorption coefficient of the material, it is simply necessary to multiply the absorption coefficient by the probability that an electron is present at the valence band energy that the electron will be excited from minus the probability that an electron is present at the conduction band energy that the electron will be excited to [14],

$$\alpha(E) = \alpha_0(E)[f_v(E_a) - f_c(E_b)]$$

where α_0 is the steady state absorption coefficient (to improve the accuracy of the calculation, the measured absorption coefficient is used rather than the modelled one), $f_v(E_a)$ is the probability that a state at E_a below the valence band maximum will be occupied by an electron, and $f_c(E_b)$ is the probability that a state at E_b above the conduction band minimum will be occupied by an electron. E_a and E_b are determined by the energy of the light and the band structure of the material and can be calculated as [14],

$$E_a = (E_G - E)\frac{m_e^*}{m_e^* + m_h^*} \quad \text{and} \quad E_b = (E - E_G)\frac{m_h^*}{m_e^* + m_h^*}$$

with m_e^* and m_h* representing the electron and hole effective masses, respectively. Note, that E_a is negative for energies below the valence band maximum.

When an ultrafast femtosecond pump laser pulse excites electrons to the conduction band of a material, the photo-excited electrons and holes initially have a very non-equilibrium distribution. On the order of 10s to 100s of fs though, the photo-excited electrons and holes will scatter with each other and phonons of the lattice to adopt a Fermi-Dirac energy distribution with separate quasi-fermi levels for the electrons and holes. Therefore, when calculating the probability that states at a given energy will be occupied when a pump pulse reaches the sample, the Fermi-Dirac distribution can be used. Hence [14],

$$f_v(E_a) = \frac{1}{1+e^{(E_a - E_{Fv})}} \qquad \text{and} \qquad f_c(E_b) = \frac{1}{1+e^{(E_b - E_{Fc})}}$$

Where the quasi-fermi levels for holes and electron, E_{Fv} and E_{Fc} can be calculated from the Joyce Dixon approximation [69],

$$E_{Fv} = -\left[\ln\left(\frac{N}{N_V}\right) + \frac{1}{\sqrt{8}}\left(\frac{N}{N_V}\right) + \left(\frac{3}{16} - \frac{\sqrt{3}}{9}\right)\left(\frac{N}{N_V}\right)^2 + \left(\frac{1}{8} + \frac{5\sqrt{2}}{48} - \frac{\sqrt{6}}{9}\right)\left(\frac{N}{N_V}\right)^3\right] k_B T$$

$$E_{Fc} = \left[\ln\left(\frac{N}{N_c}\right) + \frac{1}{\sqrt{8}}\left(\frac{N}{N_c}\right) + \left(\frac{3}{16} - \frac{\sqrt{3}}{9}\right)\left(\frac{N}{N_c}\right)^2 + \left(\frac{1}{8} + \frac{5\sqrt{2}}{48} - \frac{\sqrt{6}}{9}\right)\left(\frac{N}{N_c}\right)^3\right] k_B T$$

Here, the approximation up to the 3rd order was used. N_v is the density of states at the valence band maximum, N_c is the density of states at conduction band minimum [24],

$$N_{v/c} = 2\left(\frac{m_{h/e^*} k_B T}{2\pi\hbar^2}\right)^{3/2}$$

and N is the photo-excited carrier density excited by the pump pulse, calculated by assuming all of the light absorbed at the pump wavelength contributes to the excitation of photo-excited carriers,

$$N = \frac{(1 - R_{\text{pump}} - T_{\text{pump}})\Phi_{\text{pump}}}{t_{\text{film}} \times E_{\text{pump}}}$$

Φ is the fluence of the pump laser, R_{pump} is the reflectance of the sample at the pump wavelength, T_{pump} is the transmittance at the pump wavelength, t_{film} is the thickness of the semiconductor film (in this case VO_2) and E_{pump} is the photon energy of the pump laser.

The following equations were all calculated, and the change in the absorption coefficient expected from band filling for a pump fluence of 1 mJ/cm^2 in the case of the 42 nm VO_2 thin-film was determined. Using the Kramer-Kronig's relation for the real part of the refractive index and the absorption coefficient, the change in refractive index expected was then calculated and plotted against wavelength in Figure 4.3a (dashed line).

4.1.3.2 Band Shrinkage

Band shrinkage can be thought of in a sense as the opposite of band-filling, although the origin is quite different. When the number of photo-excited carriers in a semiconductor reaches a critical density, the mutual screening of the lattice charge results in the carriers forming a plasma with a lower energy than the individual carriers seen at lower carrier densities. This effectively decreases the band-gap, and the magnitude of the band-gap decrease is proportional to the density of free carriers. The magnitude of the decrease is described by the following equation [70],

$$\Delta E_G = -\left(\frac{q_e}{2\pi\epsilon_0\epsilon_s}\right)\left[\left(\frac{3}{\pi}(N+N_0)\right)^{\frac{1}{3}} - \left(\frac{3}{\pi}(N_0)\right)^{\frac{1}{3}}\right]$$

where ϵ_s is the static relative permittivity of the material (relative permittivity at DC) and N_0 is the intrinsic carrier concentration of VO_2. Simply incorporating this shift into the model of the absorption coefficient allows the change in the absorption coefficient expected from this phenomenon to be determined; however, the models of the absorption coefficient for both direct and indirect band gap materials are not necessarily very accurate away from the band gap energy. Therefore, instead of using the model of the absorption coefficient to calculate the change in absorption caused by the band gap shift, an effective energy method can be used [71]. In the effect energy method, the measured absorption coefficient is used, and the new absorption coefficient after band gap shrinkage is calculated by shifting the photon energy by the band gap shrinkage. The resulting equation is described by

$$\Delta\alpha(E) = \alpha_0\left(E - \Delta E_g\right) - \alpha_0(E)$$

Once again, using the Kramer-Kronig's relation, the refractive index was calculated and plotted in Figure 4.3a (dotted line).

4.1.3.3 Free-Carrier Excitation

As the free carrier density increases due to photo-excitation, the electrical properties of the material are modified. Photo-excited carriers, whether holes in the valence band or electrons in the conduction band behave as free carriers that add a Drude-Lorentz response to the dielectric response of the material. This is discussed in detail earlier in section 1.1.3 on epsilon-near-zero materials. Though the density of free carriers in VO_2 is very low under ambient conditions, photo-excitation by a strong pump pulse can significantly increase the number of free carriers and lead to the Drude response having a non-negligible impact on the refractive index of the material in the near-IR. To model this effect, an additional Drude-Lorentz component is simply added to the relative permittivity of the material [14].

$$\Delta\epsilon_r = -\frac{{\omega_p}^2}{\omega^2 + i\omega\gamma}$$

In the equation for the plasma frequency,

$$\omega_p = \frac{N{q_e}^2}{\epsilon_0 m^*}$$

N is taken as the photo-excited carrier density and the damping frequency, γ, is taken from values reported in the literature. The resulting change in refractive index can be calculated as,

$$\Delta n = \sqrt{\epsilon_{r0} + \Delta\epsilon_r} - \sqrt{\epsilon_{r0}}$$

where ϵ_{r0} is the initial relative permittivity. For small changes in the relative permittivity this can be approximated by a second order Taylor series expansion to give,

$$\Delta n = \frac{\Delta\epsilon_r}{2n_0} - \frac{(\Delta\epsilon_r)^2}{8{n_0}^3}$$

in which n_0 denotes the initial unmodified refractive index of the material. The calculated change in the refractive index for a 1 mJ/cm^2 pump fluence is shown in Figure 4.3a (dashed-dotted line).

4.1.3.4 Summary of Calculations

The effect of the three phenomena discussed above on the refractive index of VO_2 are plotted in Figure 4.3a below. The various parameters used in calculating the refractive index changes are detailed in Appendix A. From this figure, it is clear that the change in the refractive

index caused by the band-shrinkage effect strongly dominates the response at 1550 nm, with the other two effects only modifying the refractive index very slightly.

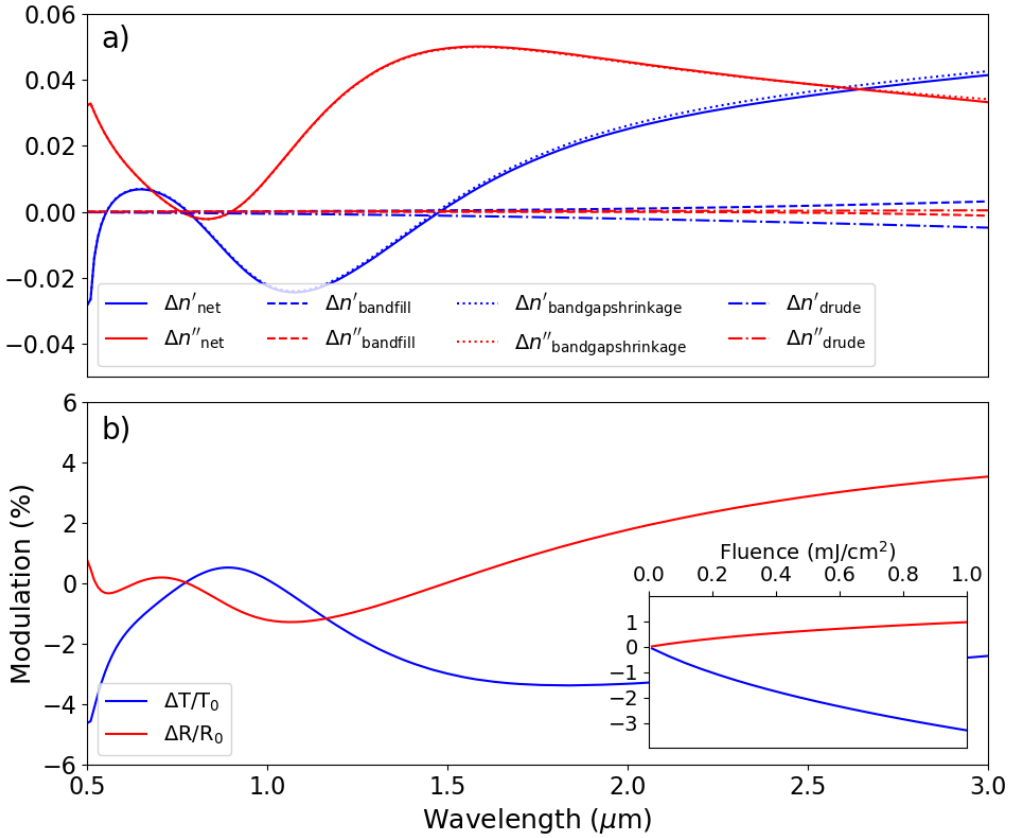

Figure 4.3: Photo-carrier induced change in VO_2's optical properties. a) Change in the refractive index of VO_2 due to photo-excited carriers. The theoretical change in the refractive index due to photo-excited carriers caused by the three predominant effects: band filling (bandfill), band gap shrinkage (bandgapshrinkage) and free carriers (drude). b) predicted short-lived modulation of VO_2 for a 1 mJ/cm^2 pump fluence for various wavelengths. (inset) Predicted modulation at 1.55 μm for different pump fluences.

The modulation expected was plotted against wavelength over the visible and nearIR range for a pump fluence of 1 mJ/cm^2 in order to compare the predicted value to that measured in experiment (Figure 4.3b). The calculation of the modulation from the refractive index variation is discussed in Appendix B. Note, the calculation was slightly modified for this figure, as an accurate prediction of the band-shrinkage effect must also include the effect of band-filling on the absorption for the reduced band gap as well. Therefore, instead of calculating the band-filling effect and band gap shrinkage effect separately, a single equation was used to calculate the change in absorption resulting from both effects. With the change in absorption being represented by,

$$\Delta\alpha(E) = \left(\alpha_0\left(E - \Delta E_g\right) - \alpha_0(E)\right)\left[f_v(E_a) - f_c(E_b) - 1\right]$$

Because E_a and E_b are relative to the valence and conduction band edges, as are E_{Fv} and E_{Fv}, the equations for these do not need to be modified to account for the changing bandgap.

At 1 mJ/cm^2, the predicted transmittance modulation is -4.8%, whereas the measured modulation as can be seen from Figure 4.2 is -3.1%. Although the two values do not match exactly, they have a similar order of magnitude, and the sign of the modulation for both the transmittance and reflectance modulation both agree with this band gap shrinkage induced modulation. The discrepancy between the exact values may be caused by a variety of factors, among these are inaccuracy of the effective masses, static permittivity or any other material parameter, and the slight discrepancy should not be taken negatively.

To see if the observed linear scaling of the pump modulation is reproduced by the model of the photo-induced change in the refractive index at low fluences, the modulation at 1550 nm for a range of pump fluences was calculated and plotted in Figure 4.3b inset. Upon examining Figure 4.3b inset, we find that the modulation intensity over the low-fluence region is very similar to that obtained in experiment, but the modulation scales to the power of 2/3 with fluence. This is because ΔE_G scales with the cubed root of the photo-excited carrier concentration, and the absorption coefficient scales with the square of the difference between the photon energy and ΔE_G. It can therefore be concluded that the short-lived modulation is a result of changes in the refractive index of VO_2 caused by photo-excited holes and electrons excited by the pump pulse. This gives a clear explanation for the dynamics of the short-lived modulation as well, as recombination of the photo-excited carriers occurs on a ps timescale, causing the modulation resulting from these photo-excited carriers to also recover on a ps timescale.

An interesting consequence of this conclusion is that the photo-induced response could be used as a means of measuring the recombination of photo-excited carriers in VO_2. This could allow for temporal resolution of the recombination process much higher than is possible with traditional micro photo conductance measurements.

Another interesting thing to note is that the band gap shrinkage phenomenon is a process that has a threshold associated with it. As discussed earlier, the band shrinkage effect only occurs after the free carrier density reaches a critical density high enough to form an electron-hole plasma – known as the Mott density, but unrelated to the Mott transition. Below this density this effect should disappear and a non-linearity in the modulation vs. pump fluence

should be seen. Unfortunately, the Mott density is very low for most materials ($7x10^{16}$ cm^{-3} for GaAs [14]), and a pump fluence low enough to be below this threshold could not be used.

4.1.4 Nature of Long-Lived Modulation at Low-Fluences

Similar to the short-lived modulation, the long-lived modulation in the low-fluence region of VO_2's photo-induced modulation shows a linear dependence on the pump fluence with no threshold behaviour. This suggests that a non-linear threshold phenomenon such as an IMT in the VO_2 is unlikely to be the cause of the modulation at low-fluences. The long-lived nature, on the order of 100s of ps to several ns, of the modulation also rules out the contribution of photo-excited carriers in creating this modulation, as they would have relaxed on a ps timescale as discussed above. Another possible explanation, and the most likely, is that the refractive index change is simply a thermos-optic effect. The lattice temperature of the VO_2 changes as a result of the relaxation and recombination of the photo-excited carriers and the thermo-optic changes in the refractive index are what is seen in the long-lived modulation. This hypothesis can easily be tested by simply determining the temperature change induced by a given pump fluence, checking the modulation observed for that temperature change in the transmittance vs. temperature measurement (Figure 4.4), and comparing the temperature induced modulation to the photo-induced modulation measured.

Whenever light is absorbed by a material through the excitation of photo-excited carriers, there will always be a significant amount of waste energy that manifests as heat and raises the temperature of the material. This is known as photothermal heating and originates from two main sources. The first source is the extra energy beyond the band gap energy that photons of the light contain. If the photon energy of the incident light is larger than the band gap energy, then electrons will be excited from below the valence band maximum to an energy above the conduction band minimum. The relaxation of the electrons from their elevated energy to the bottom of the conduction band and the relaxation the holes to the top of the valence band occurs through scattering processes between the phonons of the lattice and the carriers and raises the temperature of the lattice. Another source is non-radiative recombination processes. In addition to recombining through the emission of a photon, carriers can recombine through non-radiative pathways that dissipate the extra energy into heat. These non-radiative pathways are far more common than radiative pathways for indirect band gap materials like VO_2. Based on this, it is possible to predict the photothermally induced temperature change of

the VO_2 lattice after excitation by the pump laser pulse by assuming that all of the absorbed energy contributes to warming the VO_2 according to the following equation,

$$\Delta Temp = \frac{(1 - R_{766\,nm} - T_{766\,\mathrm{nm}})\Phi_{\mathrm{pump}} M_u}{t_{film}\rho_{\mathrm{VO2}} C_p}$$

where C_p is the heat capacity of the VO_2 and ρ_{VO2} is the density of the VO_2. Note, a more accurate calculation of the temperature change that accounts for the difference in absorption at different depths in the VO_2 thin-film is provided in the subsequent section; however, for the simple discussion of the long-lived modulation at low-fluence given here, this average temperature change will suffice.

The dependence of VO_2's transmittance on temperature was calculated for a range from 20C to 100ºC, as can be seen in Figure 4.4. The IMT can clearly be seen at 67C, along with its characteristic hysteresis. In addition to the strong decrease in the transmittance of the VO_2 at the T_{IMT}, we can see that there is also a linear decrease in the transmittance with temperature. The inset of Figure 4.4 shows this more clearly with the differential modulation, compared to the transmittance at 20ºC plotted against the temperature. At 40ºC, or a temperature change of 20 C, we see that the induced modulation in the transmittance is -2.41%. The fluence corresponding to a 20ºC change can be calculated from the equation above to be 0.84 mJ/cm^2, and from Figure 4.2 we can see that at a pump fluence of 0.84 mJ/cm^2, the induced long-lived modulation is approximately -0.58 %. The fact that the expected modulation from photothermal excitation is significantly larger than the observed modulation clearly indicates that the photothermally induced modulation dominates the long-lived modulation. The measured modulation being less than what is expected is likely because heat dissipation was ignored in calculating the temperature of the VO_2 after photoexcitation. In reality some of the photothermally generated heat will be dissipated between the excitation by the pump pulse and the measurement of the long-lived modulation at 100 ps.

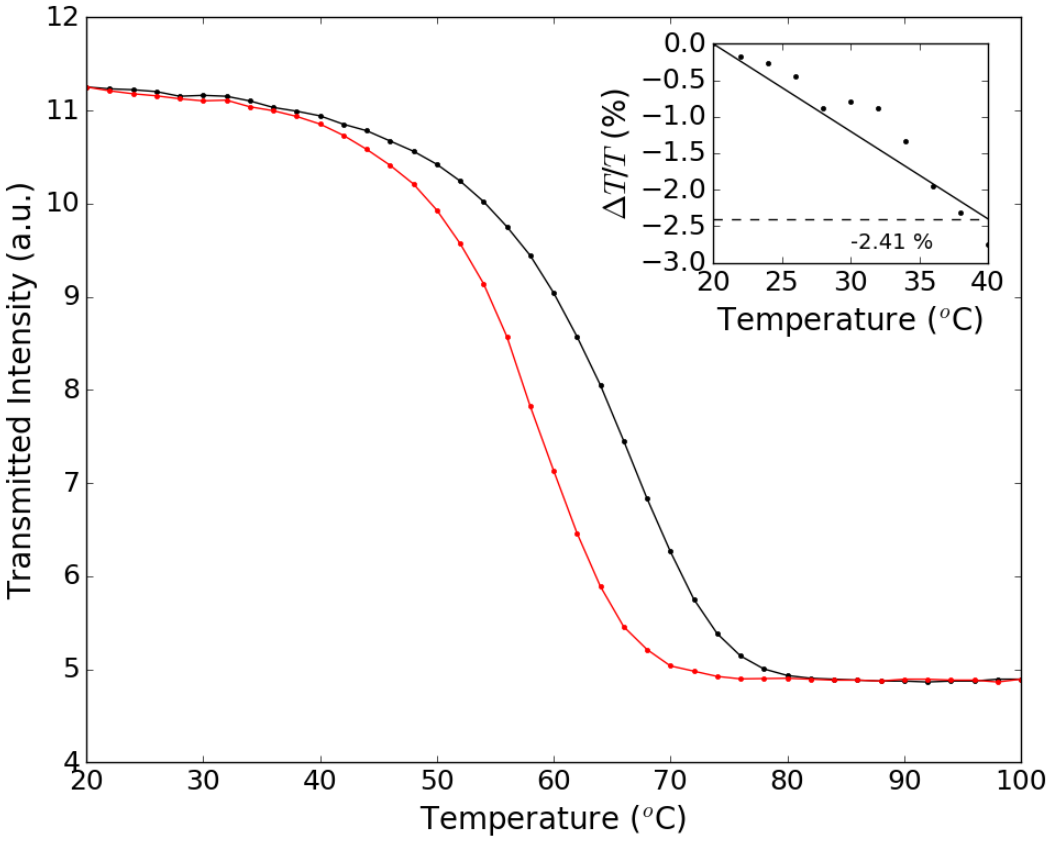

Figure 4.4: Transmittance of 42 nm VO_2 thin-film at different temperatures. The transmitted intensity of 1550 nm laser light through the VO_2 thin-film at different temperatures for an increasing temperature scan (black) and decreasing temperature scan (red). A clear hysteresis in the transmittance curve can be seen at the T_{IMT}. (inset) differential transmittance for the range of 20ºC to 40ºC.

4.1.5 Mid-Fluence Region Response

In order to better understand the mid-fluence region, the transient transmittance modulation was examined over a much longer range of time, as can be seen in Figure 4.5. The low-fluence regime behaves as one would expect, after the initial recovery of the short-lived modulation, the long-lived modulation gradually decays with a time constant of several hundred ps. The long-lived modulation at low fluences is simply a result of photothermally induced changes in the lattice temperature, and the recovery time constant is therefore limited by heat dissipation to the substrate. In the high-fluence regime, the incident pump pulse provides enough energy to induce a CPT of the VO_2 to the high-temperature rutile phase and heat the VO_2 significantly above the phase transition temperature. The recovery of the initial optical properties thus requires both the dissipation of the heat and the change of the crystal structure back to the low temperature monoclinic phase. This results in the long-lived recovery occurring on a much longer timescale of hundreds of ns, as has been observed by others [55,56]. Unlike the low- and high-fluence regimes, the mid-fluence regime exhibits an unexpected behaviour. The

gradually increasing long-lived modulation that was seen on the short-timescale peaks at a maximum modulation around approximately 100 ps, but rather than exhibiting a slow decay on the 100s of ns timescale, as was observed in the high-fluence regime, the recovery is at a similar rate to the low-fluence regime recovering over 70% of the modulation within 1 ns.

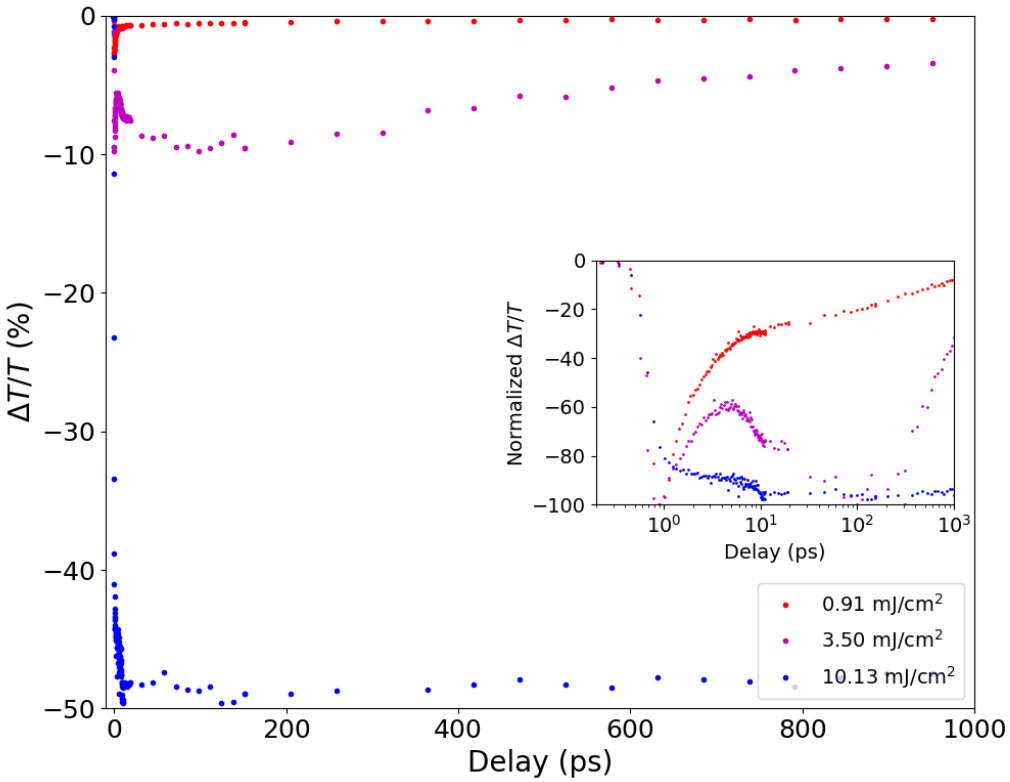

Figure 4.5: Long-timescale differential transmittance of 42 nm VO_2 thin-film. Differential transmittance of the three pump fluences on a long-timescale normalized to the maximum of their respective curves. (inset) Normalized differential transmittance plotted on a logarithmic x-axis.

The differential transmittance of VO_2 at a delay of 0 ps (maximum of the short-lived modulation), 100 ps (maximum of the long-lived modulation in mid-fluence regime) and 1 ns are shown again in Figure 4.6 to illustrate the recovery dynamics of the different regimes of behaviour and their associated thresholds.

We can see from the inset of Figure 4.6a, that the long-lived modulation at 100 ps and 1 ns initially scales linearly with pump fluence at low pump fluences. In this region the recovery in the long-lived modulation region can be approximated by an exponential decay, and the time constant of the decay, τ, can therefore be calculated according to,

$$\tau = \frac{1\ ns - 100\ ps}{\ln\left(\frac{T_{1\ ns}}{T_{100\ ps}}\right)}$$

For the low-fluence region, a τ of approximately 930 ps is observed as seen in Figure 4.6b. At a threshold pump fluence, measured here to be 1.47 mJ/cm^2, the modulation at 100 ps begins to deviate from a linear dependence on pump fluence, suggesting a non-linear process such as an IMT has begun to occur. At the same time, however, ttime constant of the long-lived modulation decreases, indicating a faster recovery of the modulation, as opposed to a slower recovery that is usually seen when VO_2 undergoes a phase transition to its high-temperature rutile phase. The time constant does not begin to increase until above a much higher threshold of 3.82 mJ/cm^2. Above the second threshold of 3.82 mJ/cm^2, the time-constant begins to increase with increasing pump fluence, exceeding 100 ns at a fluence of 10.49 mJ/cm^2. This indicates a longer time constant for recovery, as can clearly be seen from the long-timescale differential transmittance measurement at 10.13 mJ/cm^2 shown in Figure 4.5.

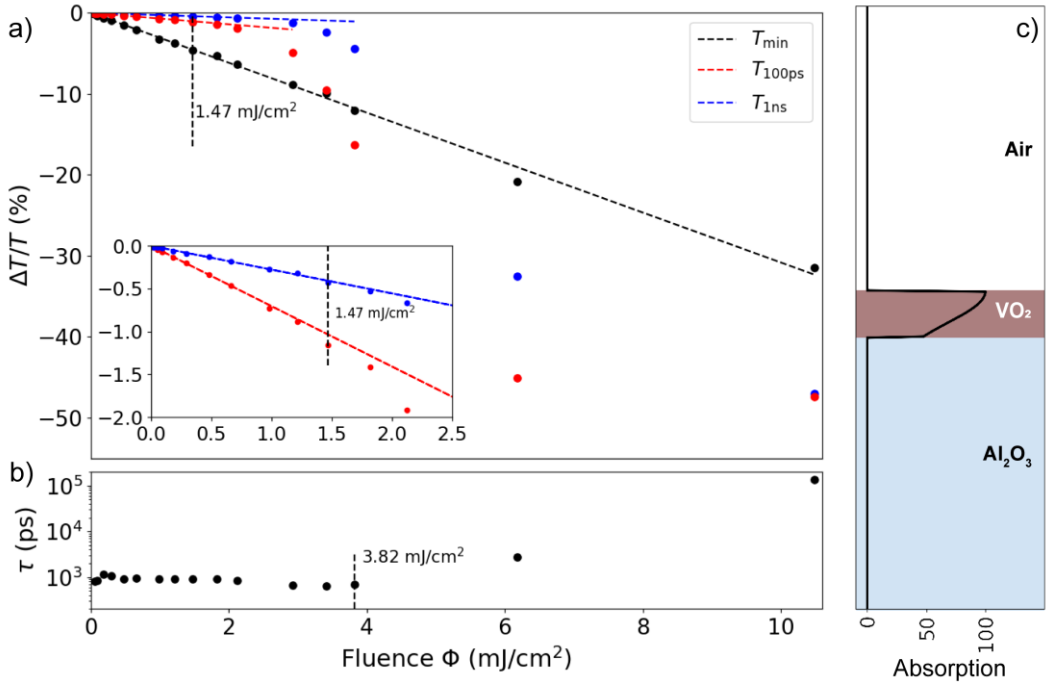

Figure 4.6: Modulation and recovery dependence on pump fluence for 42 nm VO_2 film. a) Differential transmittance at a 0 ps, 100 ps and 1 ns probe delay. b) Ratio of the modulation at 100 ps vs 0 ps and the modulation at 1 ns vs the modulation at 100 ps plotted against pump fluence. The vertical dashed lines at 1.47 mJ/cm^2 and 3.82 mJ/cm^2 represent respectively the onset of a non-linear increase in the long-lived modulation, corresponding to the IMT, and the onset of the increase in the ratio between the modulation at 1 ns and 100 ps, corresponding to an increase in the long-lived modulation recovery time. c) Simulated absorption distribution in the VO_2 thin-film used to calculate the local photothermal heating of VO_2.

In Wen et al.'s study of the recovery of VO_2 after photothermal excitation, they concluded that the non-linearity in VO_2 modulation was a result of a photothermally induced CPT to the high-temperature rutile phase [56]. In order to compare the two thresholds found in this work to theirs, the predicted change in VO_2's temperature if all absorbed energy contributes to heating was calculated.

As a first step, the spatial distribution of the pump light absorption had to be determined. Using the rigorous coupled wave analysis method (DiffractMOD, Rsoft Design Group, Ossining, USA), the absorption profile in a 42 nm thick VO_2 thin-film was simulated. Because the pump pulse used in this work has a pulse width of 250 fs, which corresponds to a spatial pulse width of 25.7 μm in VO_2 (refractive index of 2.92 at 766 nm), the pump pulse will interfere with itself as it passes through the VO_2 thin-film and RCWA therefore gives a good prediction of the true absorption distribution in the VO_2. The simulated absorption distribution, normalized to the maximum in absorption, is shown in Figure 4.6c.

With this absorption distribution, it is then possible to calculate the local temperature change induced in the VO_2 thin-film according to,

$$\Delta Temp = \frac{A(x)}{\rho_{VO2} C_p}$$

where C_p and ρ_{VO2} are the heat capacity and density of VO_2 (0.69 J/gK and 4.34 g/cm^3 [72]) and $A(x)$ is the absorbed energy in J/cm^3 at x in the film and can be simply calculated from the normalized absorption distribution in Figure 4.6c by,

$$A(x) = \frac{A_{norm}(x)}{\int_0^{t_{film}} A_{norm}(x)\, dx}(1 - R_{766nm} - T_{766nm})\Phi$$

Here, R_{766} and T_{766} are the reflectance and transmittance of the VO_2 thin-film at the pump wavelength (766 nm) measured experimentally and Φ is the pump fluence. $(1 - R_{766nm} - T_{766nm})\Phi$ is the total pump energy absorbed by the thin-film in J/cm^2.

Using the above equations, we find that the first measured fluence corresponds to a temperature change of 43.89ºC where the absorption is highest at the top surface, which results in an increase from an initial temperature of 22 ºC to a final temperature of 65.89 ºC, nearly at VO_2's phase transition temperature of 67 ºC. It is important to note, however, that the transition of VO_2 from its monoclinic phase to its rutile phase is a first order transition with an associated latent heat of 51.46 J/g [73]. Therefore, in order for VO_2 to undergo a photothermally-induced CPT additional energy is required. The pump fluence required to raise VO_2's temperature to 67 ºC and provide the latent heat was calculated to be 4.00 mJ/cm^2. The similarity between this second threshold value and the measured threshold of 3.82 mJ/cm^2 for the onset of the increasing recovery time cannot be dismissed, especially when it is considered that the no data point exists for a 4.0 mJ/cm^2 fluence, and therefore the threshold lying there cannot be ruled out.

The pump fluence at which the bottom surface of VO_2 would be photothermally excited to 67 ºC is 3.17 mJ/cm^2. Though this is further from the measured threshold of 3.87 mJ/cm^2, the proximity to the threshold makes it difficult to conclude whether the second threshold is related to the bottom surface of VO2 reaching 67 ºC or the CPT to the rutile phase of VO_2.

Studying a thinner sample of VO_2 has the potential to clarify the nature of the second threshold, as the absorption distribution will be more uniform, and therefore, the mid-fluence region would be expected to disappear if the second threshold is related to the photothermal excitation of the back surface of VO_2. For this reason, a 15 nm VO_2 thin-film was fabricated and the modulation at a 0 ps, 100 ps and 1 ns delay was measured for a range of pump fluences (Figure 5). The response once again exhibits two threshold fluences, one at 2.03 mJ/cm^2 representing the onset of a non-linearity in the long-lived modulation, and a second at 5.07 mJ/cm^2 representing the fluence at which the recovery time-constant of the long-lived moduation begins to increase. The absorption profile in Figure 4.7c shows a much more uniform distribution with the absorption only differing by 10 % between the top and bottom surfaces of the VO_2.

The same analysis of the photothermal temperature change used on the 42 nm thin-film was performed on the 15 nm thin-film. The fluence corresponding to the top surface of VO_2 being photothermally excited to 67 ºC was found to be 1.78 mJ/cm^2 and the fluence corresponding to the additional latent heat energy also being provided was found to be 4.72 mJ/cm^2. The fluence corresponding to the bottom surface of VO_2 being photothermally excited to 67 ºC, on the other hand, was found to be only 1.97 mJ/cm^2. The proximity of the measured second threshold and the threshold for the photothermally induced full CPT suggests that the second threshold and the onset of the slow recovery dynamics is a result of the VO_2 thin-film transitioning to the high-temperature rutile phase.

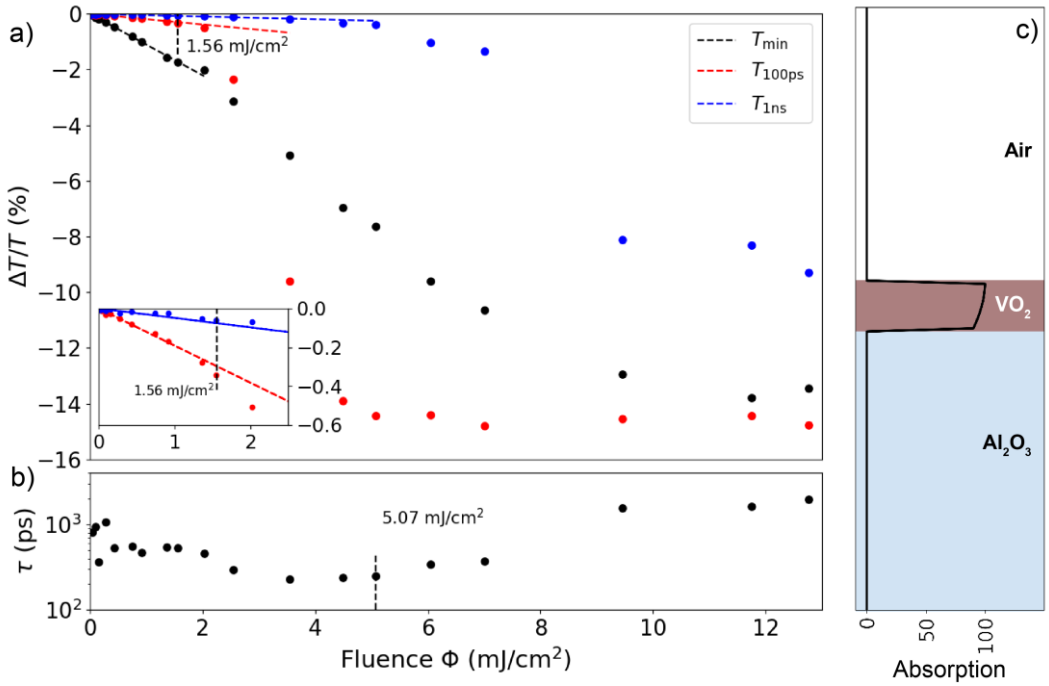

Figure 4.7: Modulation and recovery dependence on pump fluence for 15 nm VO_2 film. a) Differential transmittance at different probe delays plotted against pump fluence. b) Ratio of modulation at probe delays shown in (a) vs pump fluence. The vertical dashed lines at 2.03 mJ/cm^2 and 5.07 mJ/cm^2 represent the thresholds for the non-linearity in the long-lived modulation and the increase in the long-lived modulation recovery time, respectively. c) Absorption distribution of 766 nm pump pulse in the 15 nm VO_2 thin-film.

Another interesting aspect of the modulation vs fluence plot shown in Figure 4.7a is the fact that the modulation at a delay of 100 ps saturates at a maximal value of approximately 14% at a pump fluence lower than the second threshold. In other words, there exists a range of pump fluences in the mid-fluence region where whatever phenomenon that causes the change in the optical properties of VO_2 has fully occurred while the CPT has yet to occur.

This is highly reminiscent of the recent demonstrations of the monoclinic metal phase of VO_2 found by time-resolved electron diffraction measurements [53]. In that work, it was found that the onset of the non-linearity in VO_2's optical modulation occurs at a lower threshold than the threshold for the CPT of VO_2. A mid-fluence region – measured to be between 2 mJ/cm^2 and 9 mJ/cm^2 for their sample – was found where VO_2 retains a monoclinic crystal structure (although not identical to the steady-state monoclinic crystal structure) but exhibits metal-like optical properties. Another interesting observation is that if the same analysis discussed above is applied to the 70 nm film used in the study, the threshold at which a portion of the film is photothermally excited to 67 ºC is 2.59 mJ/cm^2, and the second threshold where a photothermally-induced CPT would be expected is at 6.89 mJ/cm^2. These thresholds do not have perfect agreement with the measured thresholds of 2 mJ/cm^2 and 9 mJ/cm^2; however, the

deviation may be due to the fact that the thresholds given by Morrison et al. are interpolated and only approximate in value [53].

This similarity strongly suggests that the mid-fluence region measured in this work corresponds to the excitation of the monoclinic metal phase of VO_2. After photo-excitation with a pump flunece above the first threshold, an IMT is triggered in a portion of the VO_2 and the VO_2 adopts the monoclinic metal phase there. Above the second threshold, there is enough thermal energy to drive the CPT, causing VO_2 to adopt the high-temperature rutile structure, from which recovery is slow due to the need for large structural rearrangement. The IMT is separate from the CPT and therefore it is possible to achieve the full IMT and maximum modulation of the 1550 nm transmittance in the mid-fluence region provided the pump pulse absorption is sufficiently uniform throughout the VO_2 thin-film.

The time-resolved differential transmittance of the 15 nm VO_2 thin-film was measured over the short-timescale (Figure 4.8) and long-timescale (Figure 4.9). From Figure 4.8, we see that at low pump fluences a semiconductor-like response similar to the 42 nm thin-film is observed. Just above the first threshold at 2.23 mJ/cm^2, after the first short-lived modulation decays, the long-lived modulation shows a gradually increasing magnitude in the same manner as the thicker film. From examining the long-timescale modulation in Figure 4.9, it is clear that the response differs slightly in that the increase in the modulation is significantly less than was seen in the 42 nm thin-film. The modulation only gradually increases from a value of approximately 80% of the maximum just after the decay of the short-lived modulation to 90% at the maximum of the short-lived modulation (ie. The initial long-lived modulation is 88.9 % of the value at the peak). In the case of the 42 nm film, the 3.50 mJ/cm^2 fluence curve increases from a value of 55% of the maximum to 100 % of the maximum at the peak of the long-lived modulation.

A clear similarity between these ratios and the absorption distributions of the films can also be observed. In the case of the 42 nm thin film, the absorption at bottom surface of VO_2 is 47.6% of the absorption at the top surface of the VO_2 (Figure 4.6c). Similarly, the 15 nm films absorption profile is close to the ratio of the initial long-lived modulation to the maximum long-lived modulation, with the absorption at the bottom surface being 90.2% of the absorption at the top surface (Figure 4.8c).

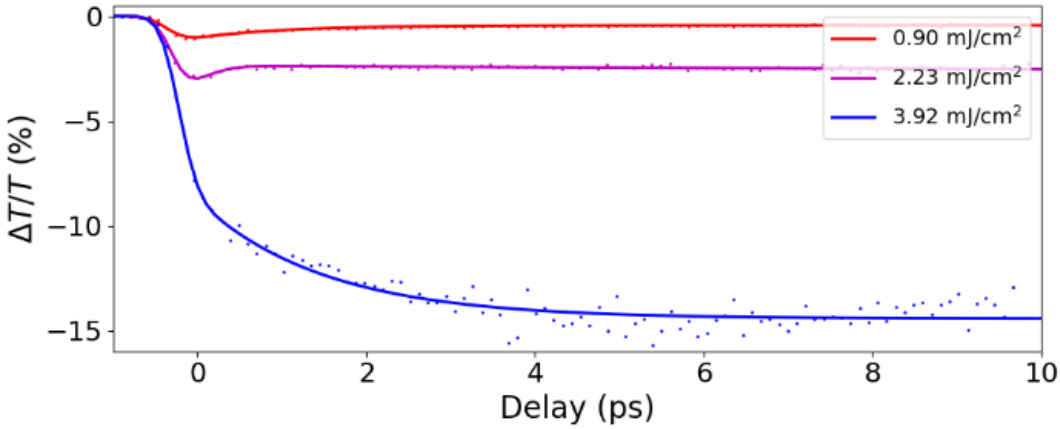

Figure 4.8: Time-resolved differential transmittance measurement of the 15 nm VO_2 thin-film.

Furthermore, the time required to reach the maximum modulation is also different for the two films. Whereas the 42 nm thin-film does not reach its maximum modulation until 100 ps in the mid-fluence region, the 15 nm thin-film reaches its maximum modulation very quickly within 10 ps. As seen in Figure 4.9, after reaching this maximum modulation, the long-lived modulation persists at the maximum modulation for a short period of time before decaying quickly. The length of time that this modulation persists also seems to depend on the fluence. Although the 2.23 mJ/cm^2 and 3.92 mJ/cm^2 decay at nearly the same rate after the long-lived modulation begins to decay, the long-lived modulation persists for nearly 100 ps in the case of a 3.92 mJ/cm^2 pump fluence and only 30 ps in the case of a 2.23 mJ/cm^2 pump fluence. Once the modulation begins to decay, the rate of recovery appears to be limited to the rate at which heat can be dissipated from the VO_2 film and therefore dependent on the film thickness. The ultra-thin 15 nm film is capable of achieving full recovery after modulation to the saturation value of 15% within a sub-ns time of 600 ps.

Finally, in the mid-fluence region, both the initial long-lived modulation and the maximum of the long-lived modulation increase gradually with pump fluence and not abruptly. A given pump fluence induces a proportional modulation and as the thermal energy diffuses from areas of high absorption to the rest of the film, the net modulation increases. This behaviour is more in line with an activation energy driven transition to the monoclinic metal phase, as proposed recently by Otto et al. [74], rather than a first-order transition as is seen for the CPT. Otto et al. proposed that the transition of VO_2 transitions to its monoclinic metal phase when conduction band electrons have sufficient energy to surmount a potential energy barrier to a metastable state. They propose that photo-excitation causes a transient increase in the conduction band electron temperature and the high electron temperature allows some electrons to surmount this barrier. The correlation between the threshold fluence for the monoclinic metal and the lattice

temperature reaching 67ºC found here, however, suggests a phonon driven process as opposed to an electron driven process. This is similar to the critical phonon density driven IMT proposed by Cocker et al., albeit at the time the monoclinic metal was unknown and it was believed the transition was a CPT to the rutile structure.

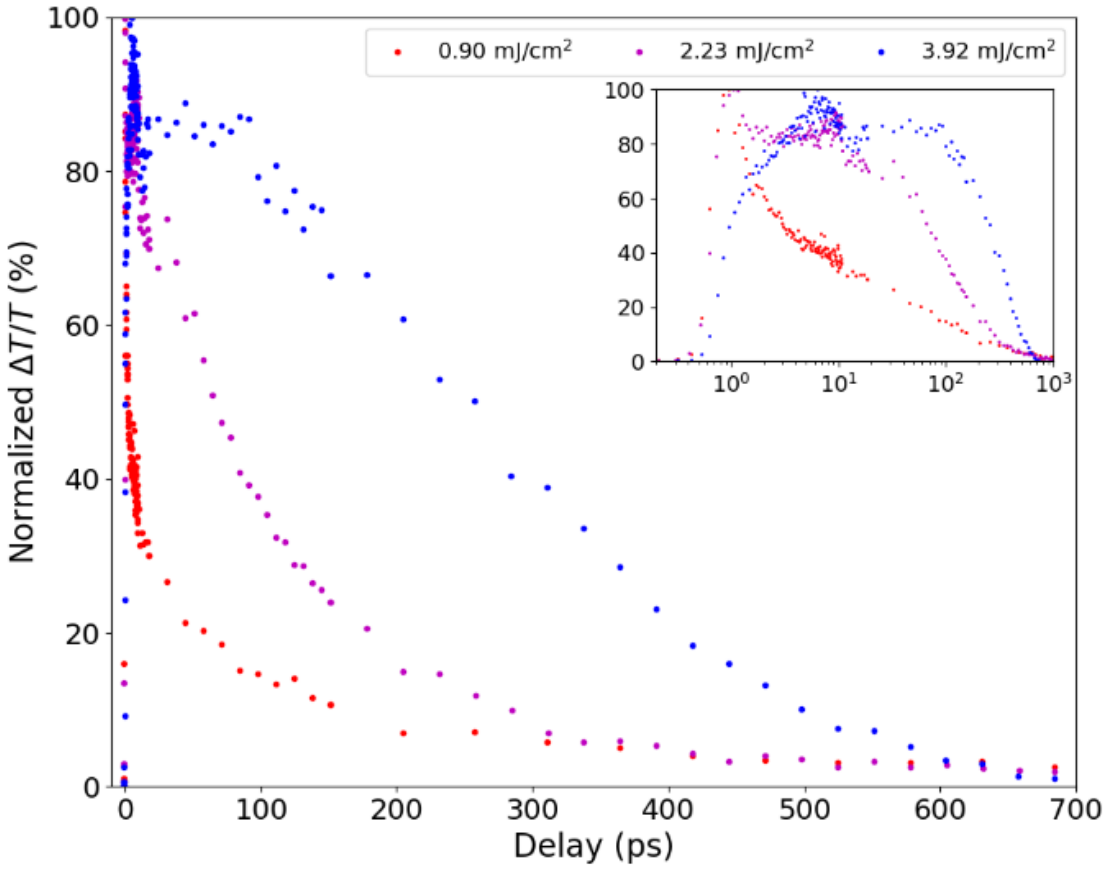

Figure 4.9: Long-timescale differential transmittance of 15 nm VO_2 thin-film. The long-timescale differential transmittance for the curves shown in Figure 4.8, normalized to the maximum of each respective curve. Both pump fluences in the mid-fluence region (2.23 mJ/cm^2 and 3.92 mJ/cm^2) show recovery on a sub-ns timescale. The onset of strong modulation occurs within 10 ps and persists for a fluence-dependent time before decaying rapidly on a sub-ns timescale.

4.2 NbO_2

Due to the low insulator-metal transition temperature of VO_2 it is difficult to isolate the thermally driven IMT from other processes unrelated to the IMT in the photo-induced modulation of the material. For this reason, the photo-induced modulation of the NbO_2 was also investigated.

4.2.1 Pump-Probe Response

The transient modulation in the reflectance and transmittance of the 60 nm NbO_2 thin-film for three different pump fluences was once again investigated and the results are shown in Figure 4.10. Similar to the VO_2, a fast modulation that recovers on a ps timescale and a slow

modulation that recovers on a timescale of hundreds of ns can initially be observed in the transmittance spectra. On examining the reflectance modulation, however, an additional ultrafast modulation with a sub-ps timescale can also be observed. On closer inspection of the transmittance modulations, the fast ps response is also found to be composed of both an ultrafast sub-ps response and a fast ps response. For this reason, the modulation in the transmittance of the NbO_2 thin-film was fit to a three-exponential decay curve given by,

$$\frac{\Delta T}{T} = A_0\left(1 + erf\left(\frac{t-t_0}{\tau_p}\right)\right)\left(A_1 e^{\frac{t-t_0}{\tau_1}} + A_2 e^{\frac{t-t_0}{\tau_2}} + A_3 e^{\frac{t-t_0}{\tau_3}}\right)$$

t_0 corresponds to the delay between the pump and probe pulses, τ_p is related to the laser pulse width and the response time of the material, and τ_1, τ_2 and τ_3 are the time-constants of the three decay rates. The components of the decay for the 1.29 mJ/cm^2 curve are shown in the inset of Figure 4.10a. There is an ultrafast decay with a time constant τ_1 of 324 fs, another short-lived decay with a time constant of τ_2 3.24 ps, and finally a long-lived decay with a time constant of τ_3 543 ps. As expected, with increasing pump fluence, the modulation intensity increases and the overall behavior and the three decay rates remain consistent. The exact values of the decay rates varied with different fluences, but an ultrafast response on the order of hundreds of fs, a short-lived response on the order of several ps, and a long-lived response on the order of hundreds of ps to several ns were consistently observed.

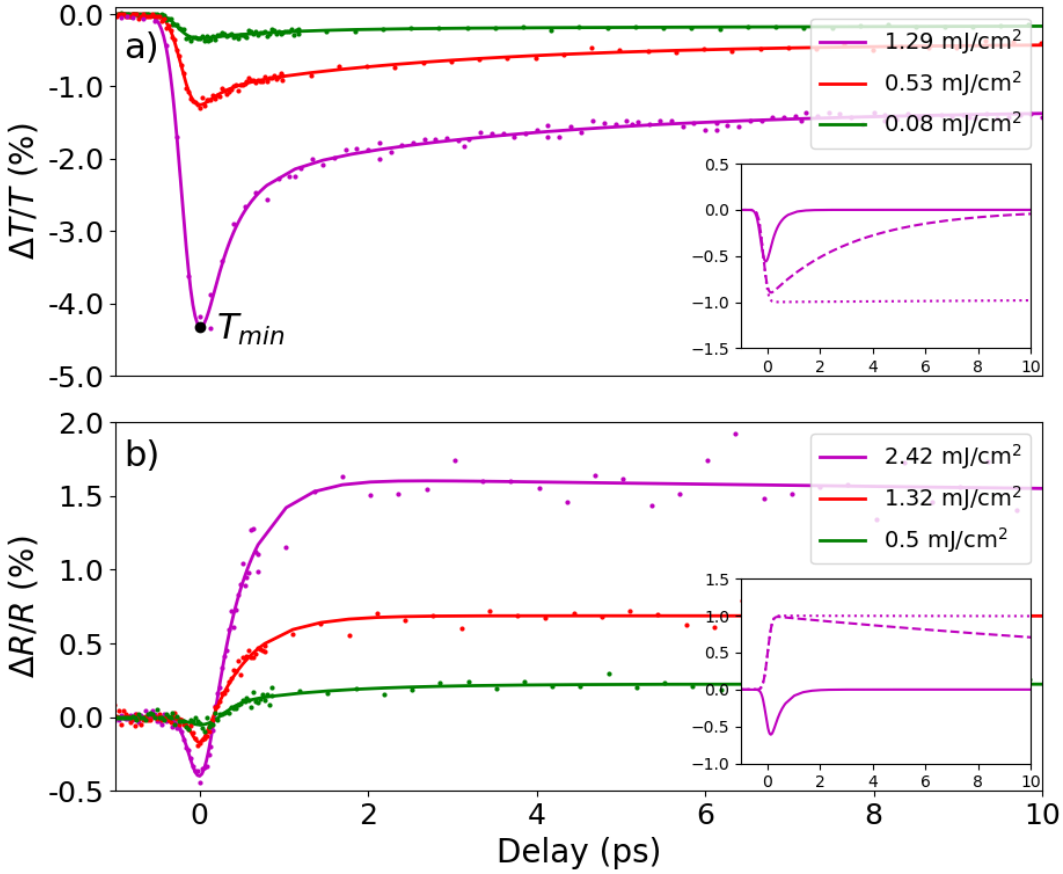

Figure 4.10: Modulation of NbO_2 after excitation by a femtosecond pump pulse. The time-resolved photo-induced modulation in the transmittance (top) and reflectance (bottom) of NbO_2 after excitation by a femtosecond laser pulse. Insets show the short-lived and long-lived components of the response for the magenta curves.

To model the reflectance, the same model in the equation above was used. The ultrafast fs response, short-lived ps response and the long-lived ns response are all observed; however, whereas the short-lived and long-lived modulations correspond to decreases in the transmittance at 1550 nm and the reflectance at 800 nm [33], they represent increases in the reflectance at 1550 nm.

4.2.2 Modulation vs Pump Fluence

The modulation in the transmittance for pump fluences between 4.6 μJ/cm^2 and 1.4 mJ/cm^2 was subsequently measured. The maximum modulation of the transmittance (T_{min} in Figure 4.10a and the modulation of the transmittance at 100 ps after the minimum (T_{100ps}) are shown in Figure 4.11. For the entire range of fluences studied, the magnitude of the modulation maximum and the long-lived modulation were found to scale linearly with pump fluence, and no evidence of any threshold for the long-lived modulation was observed. Furthermore, the ratio of the transmittance minimum to the long-lived decrease in transmittance, as shown in the upper inset of Figure 4.11, was found to be relatively constant (only fluctuating as the signal

to noise ratio decreased for very low fluences). This linear and thresholdless behaviour suggests that for these low fluence levels, both the short-lived ps response and the long-lived ns response are the result of changes in the refractive index of NbO_2 caused by photo-excited carriers in the conduction band of NbO_2 or changes in the lattice temperature as opposed to free carriers at the fermi level of NbO_2 grains that have undergone an IMT. Based on the Mott-Hubbard description, an IMT occurs when the concentration of excited carriers in the conduction band reaches a threshold level at which they sufficiently screen the coulomb interaction and cause the bandgap of the insulator to collapse [52]. This results in a drastic increase in the metallic reflection of the material. Based on this description, when the pump-fluence increases above the threshold level, we should expect a non-linearity in the fluence vs. modulation curve. For this low-fluence regime, however, we see a purely linear relation between the modulation and the fluence intensity to as low as 4.6 μJ/cm^2, meaning that no IMT threshold exists in this range.

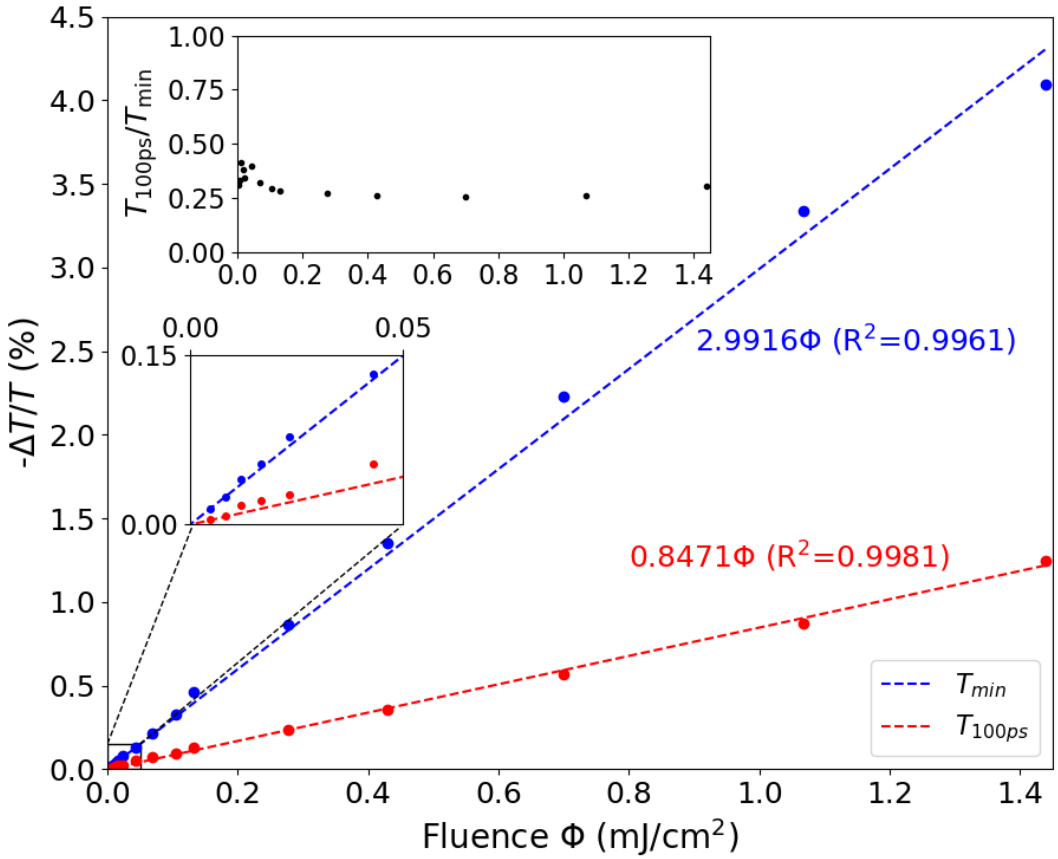

Figure 4.11: Change in modulation of NbO_2 with fluence at minimum. The change in the modulation of the transmittance at the minimum of the short-lived response and 100 ps after the minimum are plotted against pump fluence. (lower inset) Zoomed in image of the low-pump fluence region for the modulation at the minimum and 100 ps. (upper inset) ratio of the modulation at the minimum and 100 ps plotted against pump fluence.

By comparing the photo-excited carrier concentration excited by a 4.6 μJ/cm^2 pump pulse to the thermally excited carrier concentration of NbO_2 below its thermally induced IMT, we can further show that the photo-excited carrier concentration is insufficient to induce

NbO_2's IMT, and no IMT threshold exists below 4.6 μJ/cm^2 either. By assuming that each incident photon of the pump pulse is perfectly absorbed, it is possible to calculate the photo-excited carrier density using,

$$N = \frac{\Phi_{\text{pump}}}{t_{\text{film}} \times E_{\text{ph}}}$$

Here Φ_{pump} is the pump fluence, t_{film} is the thickness of the NbO_2 film, E_{ph} is the photon energy of the pump, and N is the photo-excited carrier density. Using this equation, a pump fluence of 4.6 μJ/cm^2 would correspond to a photo-excited carrier density of only 2.96×10^{18} carriers/cm^3. This is several orders of magnitude lower than the carrier concentration of NbO_2 at 1000 K, just before the thermally induced IMT [75]. Since a thermally induced IMT does not occur when the thermally-excited carrier concentration reaches this level, one would not expect the photo-excited carriers to induce an IMT when the pump fluence is only 4.6 μJ/cm^2. The optically induced metallic reflection must therefore be a result of photo-excitation increasing the free carriers in NbO_2's conduction band and not an IMT.

4.2.3 Pump-Repump Probe Response

To further support the conclusion that the long-lived modulation at low pump fluences is not the result of an IMT, a pump-repump-probe measurement was conducted. In the standard description of the long-lived modulation of NbO_2 at low fluences, the NbO_2 is proposed to have undergone an IMT in individual grains of NbO_2 where the excitation density is slightly higher than other regions. As the fluence increases, the increasing excitation density results in a larger number of grains having the threshold density of excited carriers necessary to undergo the IMT, and hence the modulation increases. In this model, after the initial excitation by the femtosecond laser pulse, the grains with an excited carrier density below the threshold have their carriers relax on a ps time scale – which describes the short-lived ps response – and the long-lived modulation is attributed to only those grains that have undergone the full IMT. According to this description, therefore, if a second pump pulse with the same magnitude as the first is incident on the sample, then the grains that previously did not reach a high enough excited carrier density to undergo a full IMT would be once again excited to a sub- threshold carrier density and would subsequently relax back to their initial state over a period of several ps, without an increase in the long-lived modulation. To test this, a second pump pulse delayed by approximately 100 ps was injected after the first. The resulting response of the NbO_2 transmittance is shown in Figure 4.12.

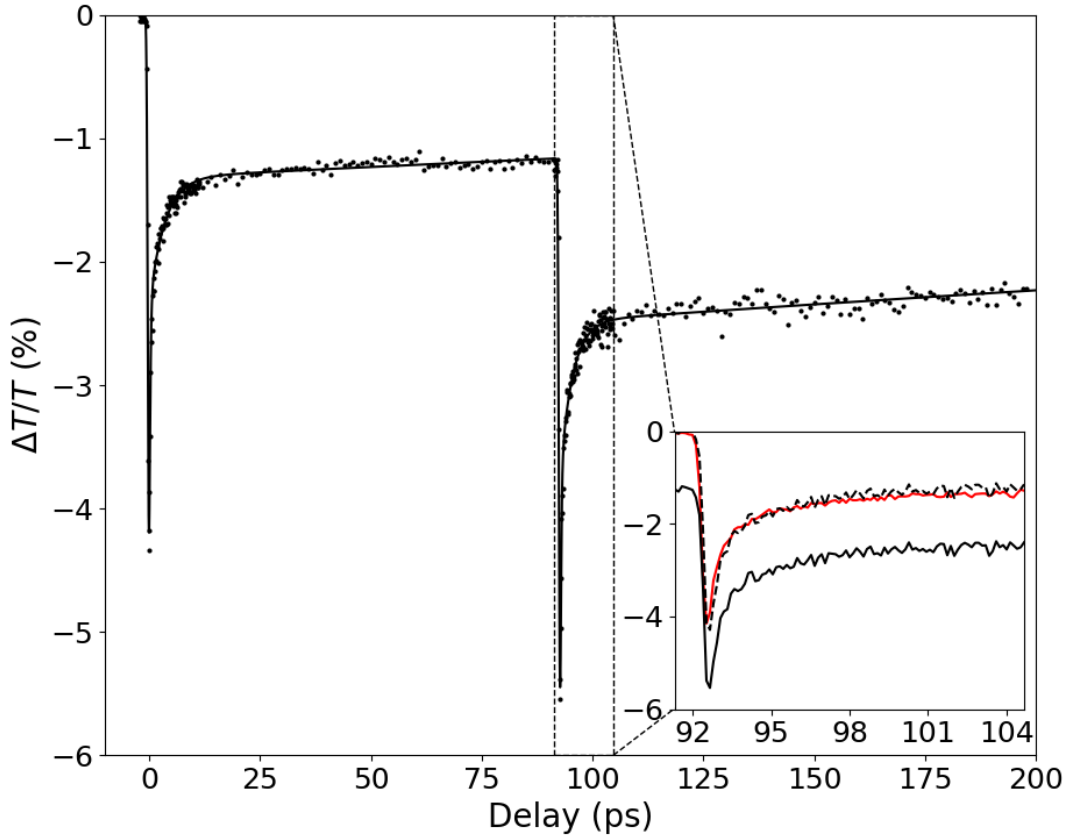

Figure 4.12: Pump-repump response of NbO_2 thin-film. The photo-induced response after and NbO_2 thin-film is excited by a 1.288 mJ/cm^2 pump pulse and then a second 1.289 mJ/cm^2 pump pulse delayed by 90 ps. The inset shows the modulation caused by the pump-repump measurement (solid black line), only the second pump pulse (sole red line) and the response of the pump-repump measurement minus the response to the first pump pulse only (dashed black line).

The first pump pulse, with a fluence of 1.288 mJ/cm^2, results in a response identical to that described earlier, where the total modulation is described by a short-lived decrease in the transmittance that decays over several ps and a longer-lived modulation that persists until the second pump-pulse arrives. The second pulse, with a fluence of 1.289 mJ/cm^2 arrives 93 ps later, and contrary to what would be expected if the long-lived modulation were caused by individual grains undergoing an IMT, it induces an identical response to the first pulse.

From the inset of Figure 4.12, it is clear that pump-repump response simply represents the linear summation of the response to the two pulses individually. If the response to both pump pulses (solid black line) is taken, and the long-lived modulation caused by the first pulse is subtracted from it, a curve (dashed black line) identical to the response to the second pump pulse alone (solid red line) is reproduced.

So far I have claimed that the explanations of the short-lived modulation and long-lived modulation in NbO_2's photo-induced modulation are insufficient to explain the results shown here. Using the same process discussed in the section 4.1 for the photo-induced modulation of

VO_2 thin-films I will attempt to analyze the short-lived and long-lived modulations of NbO_2 as well.

4.2.4 Nature of the Short-Lived Modulation

The predicted change in the refractive index of NbO_2 due to band-filling, band gap shrinkage and free carrier excitation were calculated using the same method as discussed earlier, but for NbO_2. Parameter values are discussed in Appendix A. Due to the lack of readily available data on the effective hole mass of NbO_2 [76,77], it had to be calculated from a theoretical study on the band structure of NbO_2. The calculated changes in the refractive index of NbO_2 for a pump fluence of 1 mJ/cm^2 is shown in Figure 4.13a below.

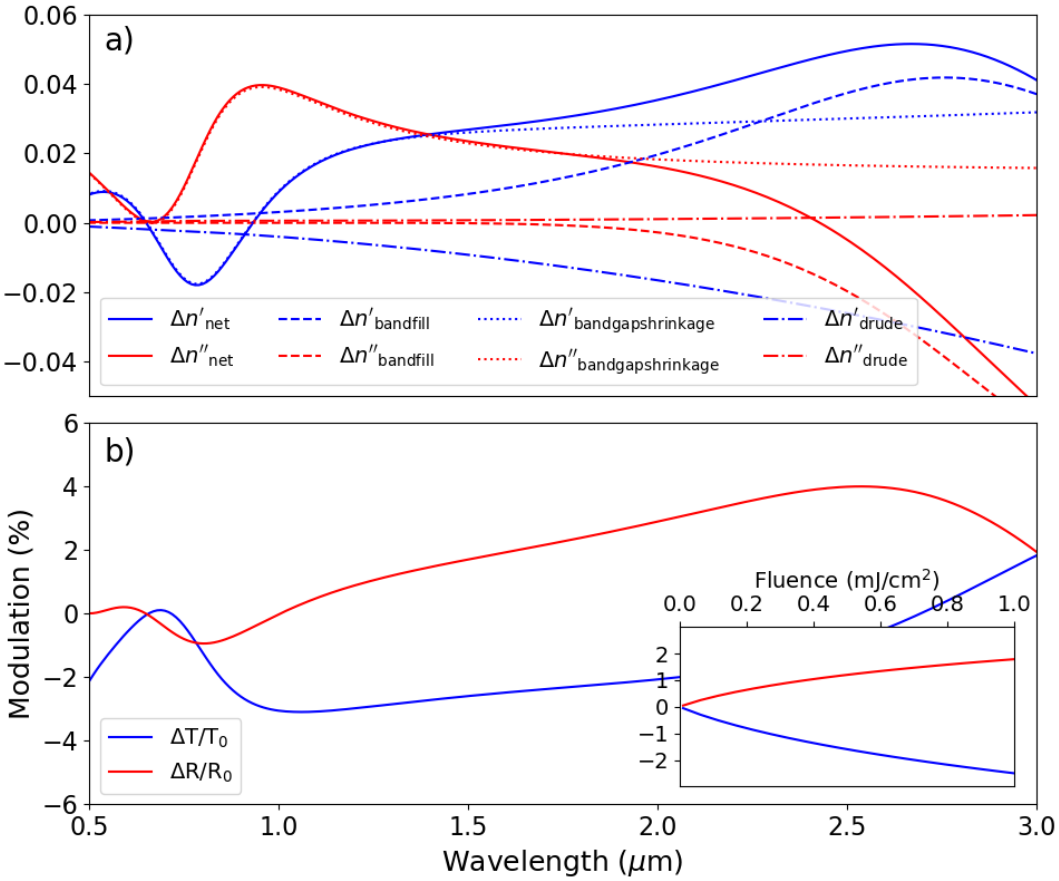

Figure 4.13: Photo-carrier induced change in NbO_2's optical properties. a) Change in the refractive index of NbO_2 due to photo-excited carriers.The theoretical change in the real and imaginary parts of the refractive index caused by the band filling effect (blue), band gap shrinkage effect (red) and Drude-response (black) originating from the photo-excited carriers excited by the pump pulse. (inset) Predicted modulation at 1.55 μm for different pump fluences.Similar to VO_2, the band shrinkage effect appears to dominate the change in the refractive index for the NbO_2. The resulting change in the transmittance and reflectance was plotted against wavelength for a pump fluence of 1 mJ/cm^2 as seen in Figure 4.13b. The observed experimental response, with an increase in the reflectance and a decrease in the transmittance can clearly reproduced.

Furthermore, the decrease in reflectance at 800 nm found by Beebe et al. [33] is also reproduced in this model of the photo-induced modulation. The magnitude of the modulation, however, is found to differ slightly from that measured in experiment. A much larger modulation for the same pump fluence is predicted by the model (-7.93% for the model vs. -2.99% for the measurement). This may be due to a variety of factors, including the intrinsic excited carrier concentration being higher than expected in the NbO_2 material used, the calculation of the pump fluence being over-estimated, or even NbO_2 effective masses being over estimated. Lower effective masses would increase the effect of the Drude response on the changes in the refractive index, and as these are in the opposite direction of the changes caused by the band shrinkage effect, they would lower the expected modulation.

To further examine how the modulation scales with pump fluence and determine whether or not the predicted scaling matches with the linear scaling found, the calculated modulation at different incident pump fluences was determined and is plotted in Figure 4.13b inset. It can be seen that the predicted scaling is not exactly linear. Just as with the VO_2 sample, the actual scaling is approximately proportional to the pump fluence raised to the power of 2/3, because of the rate at which ΔE_G scales with pump fluence. For the range of pump fluences used, this deviation from linearity falls within the noise level of the differential transmittance measurements and should not be taken as evidence that band gap shrinkage is not a good explanation for the short-lived modulation observed.

4.2.5 Nature of Long-Lived Modulation

The thermally induced change in the transmittance of NbO_2 was examined in order to determine if the low-fluence long-lived modulation could once again be explained simply by photothermally induced changes in the lattice temperature. The transmittance modulation relative to the initial room temperature transmittance is plotted in Figure 4.14.

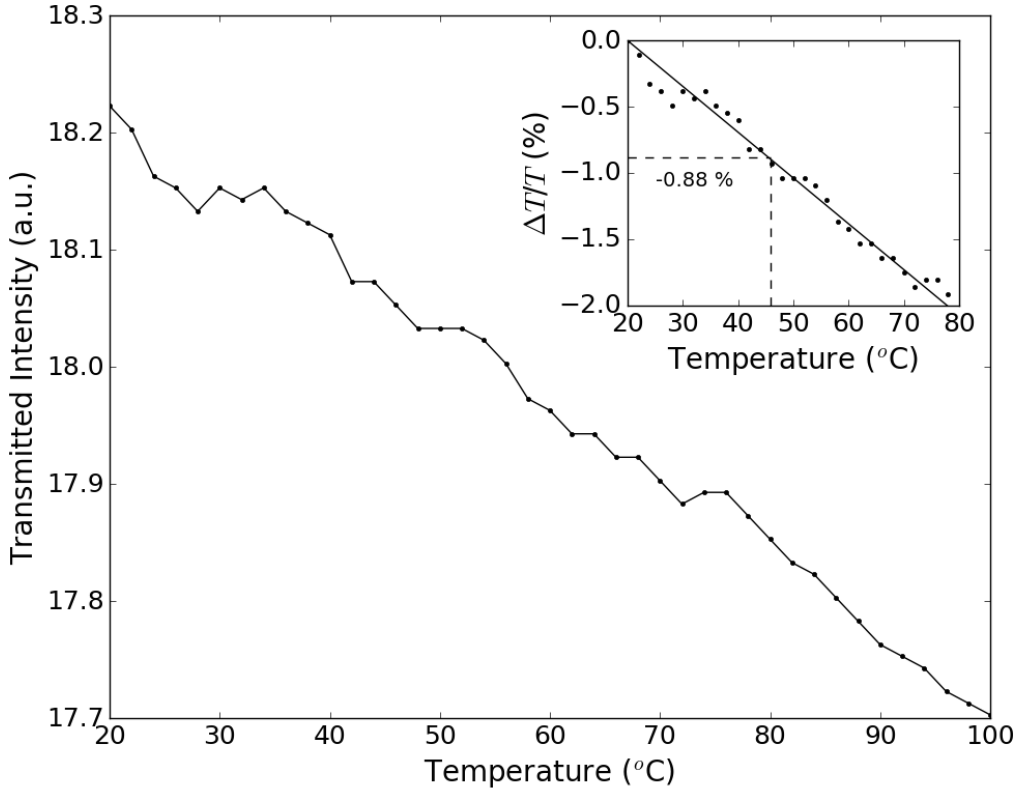

Figure 4.14: Transmittance of NbO_2 thin-film at different temperatures. Transmitted intensity of 1550 nm laser light through the 60 nm NbO_2 thin-film at different temperatures. (inset) differential transmittance relative to the transmittance at 20ºC for the range of 20ºC to 80ºC, showing a clear linear dependence of the modulation on temperature.

In comparing the modulation at different temperatures against the photo-induced long-lived modulation, the expected photothermally induced temperature increase corresponding to a given pump fluence was once again calculated according to,

$$\Delta Temp = \frac{(1 - R_{766\,nm} - T_{766\,\mathrm{nm}})\Phi_{\mathrm{pump}} M_u}{t_{film}\rho_{\mathrm{NbO2}} C_p}$$

For a pump fluence of 1 mJ/cm^2, the expected temperature increase is 25.8ºC, raising the temperature of the NbO_2 to 45.8ºC, where the modulation is -0.88% in the thermally induced modulation measurement. The corresponding in long-lived modulation at 100 ps was found to be -0.85%. The slightly larger value of the thermal measurement may be due to the fact that the long-lived modulation is measured at a 100 ps delay, and as such, the NbO_2 thin-film will have had time to dissipate some of the photothermally generated heat and is likely not at exactly 45.8ºC anymore. The lower thermal conductivity of NbO_2 relative to VO_2 and therefore the reduced amount of heat dissipation after 100 ps is likely the reason why the measured modulation is closer to the predicted modulation than was the case for the VO_2 thin-film. The

similar magnitude confirms that photothermally induced changes in the lattice temperature of NbO_2 fully explain the long-lived modulation at low pump fluences.

Chapter 5 : Size Dependence of the Photo-induced Modulation

In Chapter 4, the natures of the short-lived and long-lived responses in the photo-induced modulation of VO_2 and NbO_2 thin films were studied, and it was found that for all pump fluences, both responses are present. It was also determined that a mid-fluence region exists for VO_2, and in this region a strong modulation resulting from an IMT to a monoclinic metal state with a fast recovery can be obtained. Although both the mid-fluence monoclinic metal state of VO_2 and the short-lived ps response of NbO_2 are promising for developing all-optical modulators with strong modulations, the presence of the long-lived modulation ultimately limits how fast the materials can be modulated.

The conclusion drawn in the previous chapter that the long-lived modulation at low fluences is the result of photothermally induced changes in the lattice temperature of the materials and that the recovery is therefore governed by heat dissipation away from the film is a promising conclusion, as it is well known that thermal dissipation can be managed through the use of ultra-thin thin-films and nanostructures. In this chapter, I investigate the size dependence of the recovery rate of the long-lived modulation in the photo-induced modulation of VO_2 and NbO_2. In particular, the effects of thin-film thickness and nanostructure size on the recovery rates of the long-lived modulation of VO_2 and NbO_2 are studied.

5.1 Thin-Films

To study the size dependence of the recovery rate of the long-lived modulation, the long-lived response of VO_2 and NbO_2 thin films of varying thicknesses were studied.

5.1.1 Simulation

As the modulation in the reflectance and transmittance of VO_2 and NbO_2 thin-films were found to scale linearly with temperature for small temperature changes below the phase transition temperature, and the long-lived modulation of VO_2 and NbO_2 were found to be a result of photothermally induced changes in the lattice temperature, the recovery of a thin-film of VO_2 or NbO_2 to ambient temperature from an elevated temperature can be used to approximate the recovery rate of the optical properties as well. Using COMSOL's Heat Transport in Solids module, the cooling of a NbO_2 thin-film raised to 370 K from an ambient temperature of 273.15 K was simulated (Figure 5.1) for a variety of different film thicknesses. As would be expected, film thickness was found to be directly proportional to the rate of heat

dissipation, with thinner films dissipating heat into the Al_2O_3 substrate faster and returning to ambient temperature in a much shorter time.

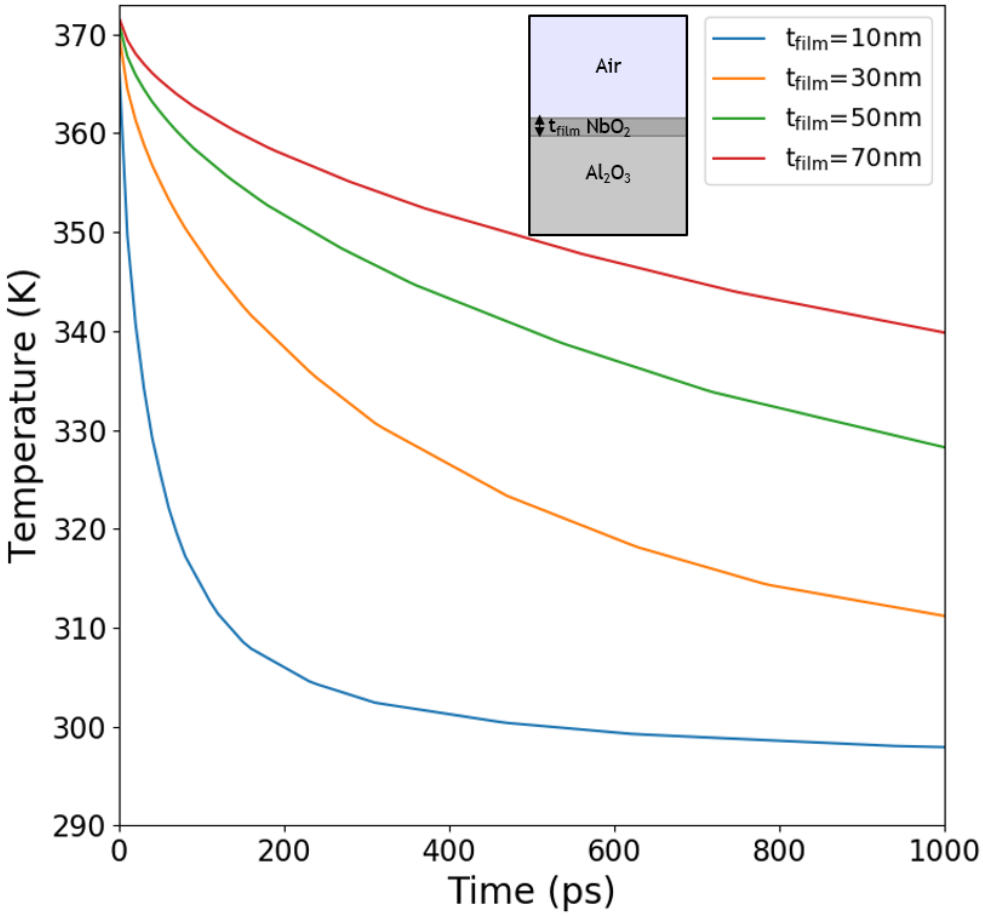

Figure 5.1: Effect of film thickness on heat dissipation in NbO_2 thin-films. Inset shows a schematic of the simulated structure.

Based on this result, it was expected that the recovery rate of the long-lived modulation in the optical properties of VO_2 and NbO_2 thin-films could also be increased through the use of thinner thin-films.

5.1.2 Experimental Results

A series of VO_2 and NbO_2 thin-films with varying thicknesses were fabricated by PLD. In order to reliably understand the effect of the thin-film thickness, it was necessary to first provide an accurate measure of the film thicknesses. This was achieved by using X-ray reflectance (XRR) as described in section 3.2.3.

To characterize the effect of the thin-film thickness on the recovery rate of the long-lived modulation observed in NbO_2 and VO_2, the modulation in the transmittance of the films was measured on the long timescale (from 100 ps after the pump pulse to 600 ps after the pump pulse). At this timescale, the only modulation remaining is the long-lived modulation, and so

the recovery rate of the long-lived modulation can be determined by fitting the measured response given by the following equation,

$$M = e^{\frac{-(t-100ps)}{\tau}}$$

Where M is the intensity of the modulation, normalized to the intensity of the modulation at a 100 ps delay, t is the delay of the probe pulse relative to the pump pulse, and τ is time constant of the modulation recovery. On the left of Figure 5.2 the normalized modulations of VO_2 films with three different thicknesses are shown. A clear trend of the recovery time constant decreasing with decreasing thickness can be seen; however, to make this trend clearer, the calculated time constants were plotted against film thickness for several difference VO_2 film thicknesses, and the results are shown on the right of Figure 5.2. Though there is a slight deviation due to noise in the modulation measurements, there is a clear trend of the time constant decreasing, indicating faster recovery of the film, as the thickness of the VO_2 film is reduced.

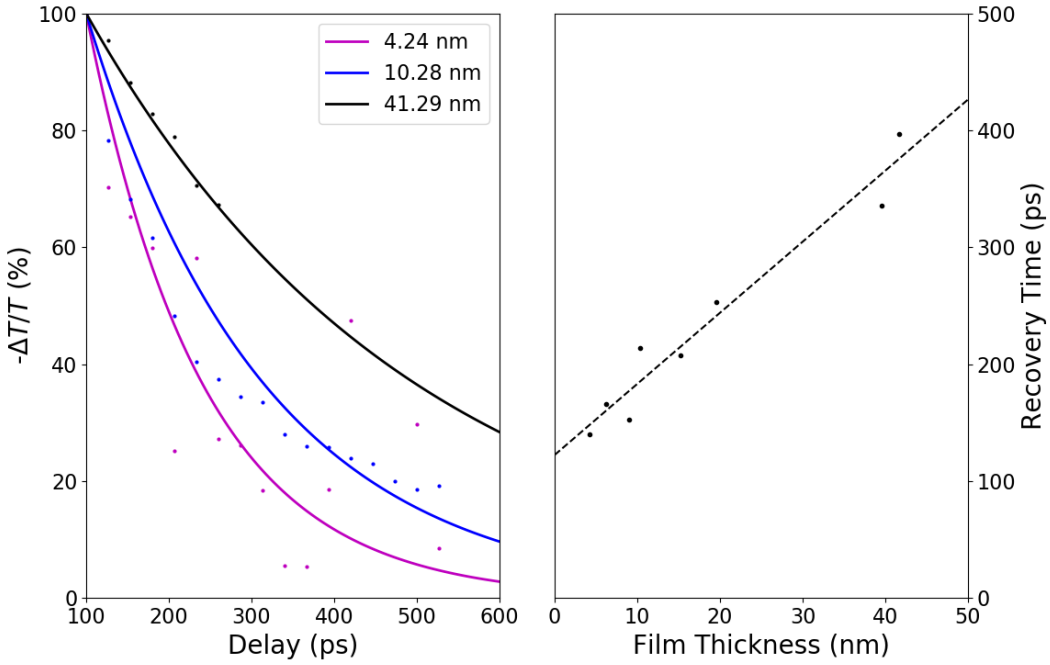

Figure 5.2: Effect of film thickness on the recovery time of VO_2's long-lived modulation. (left) transmittance modulation on the long timescale for various film thicknesses. (right) change in the time constant of the long-lived recovery with film thickness.

The same measurements were conducted for a series of NbO_2 thin-films, with the results shown on the left and right of Figure 5.3. The same linear dependence of the recovery time constant on the NbO_2 film thickness was also observed; however, both the minimum recovery rate observed and the rate at which the recovery rate increased with thickness was different than VO_2.

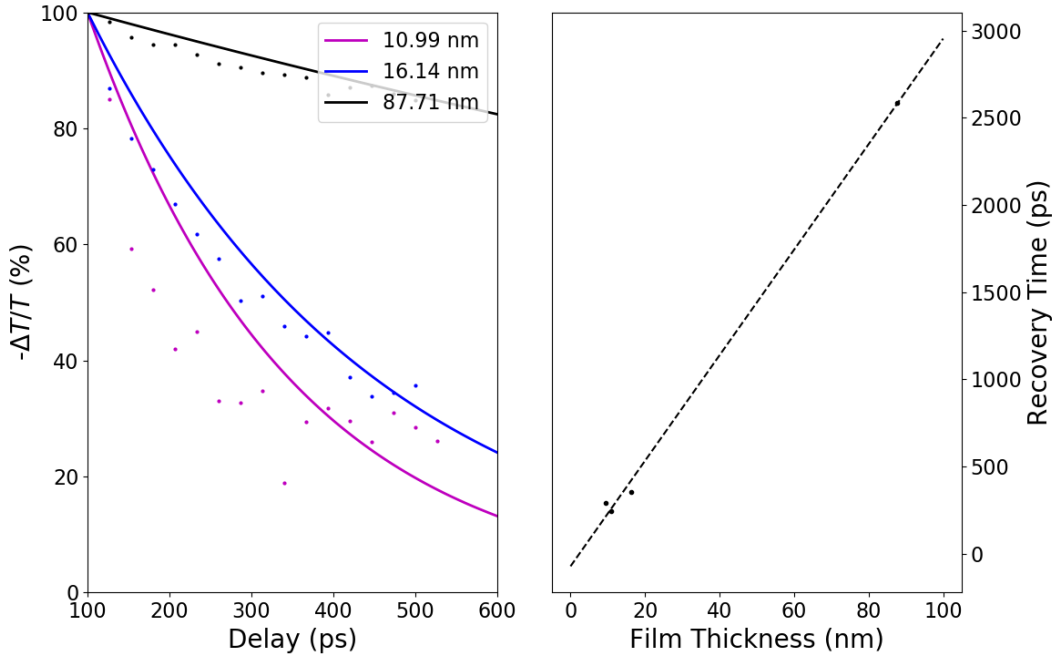

Figure 5.3: Effect of film thickness on the recovery time of NbO_2's long-lived modulation. (left) transmittance modulation on the long timescale for various film thicknesses. (right) change in the time constant of the long-lived recovery with film thickness.

These results clearly demonstrate that the recovery rates of the long-lived modulation of both VO_2 and NbO_2 scale linearly with the film thickness for film thicknesses ranging from 5 nm to 100 nm. Though this information is extremely valuable for designing insulator-metal transition material based all-optical modulators, the lowest recovery times observed, even for a 4.24 nm VO_2 thin-film that shows a very weak modulation, was on the order of 100 ps.

The primary reason for the increase in the recovery rate can simply be explained by the increase in the surface area to volume ratio as the thickness of the film is decreased. For the thin-film to return to room temperature, it must dissipate all of the excess energy to the substrate on which it is deposited. The surface area of the substrate and thin-film interface does not change as the film thickness is decreased; however, the amount of energy to be dissipated for a given temperature scales linearly with the film thickness, resulting in the time constant of the recovery scaling also scaling linearly with film thickness.

5.2 Nanopillar Arrays

As the surface area to volume ratio is the primary factor determining the rate of recovery for the long-lived modulation, it is expected that using a reducing the dimensions of the VO_2 and NbO_2 to the nanoscale in all three dimensions will further improve the recovery rate. Here we model the performance of such nanopillar structures and demonstrate their potential to decrease the recovery time of IMT materials.

5.2.1 Nanopillar Structure

A nanopillar array structure, pictured in Figure 5.4, was chosen to study the effect of nanostructure size on the recovery rate of the long-lived modulation of VO_2 and NbO_2. Isolated pillars were chosen due to their relative ease of fabrication, and their electrically isolated nature.

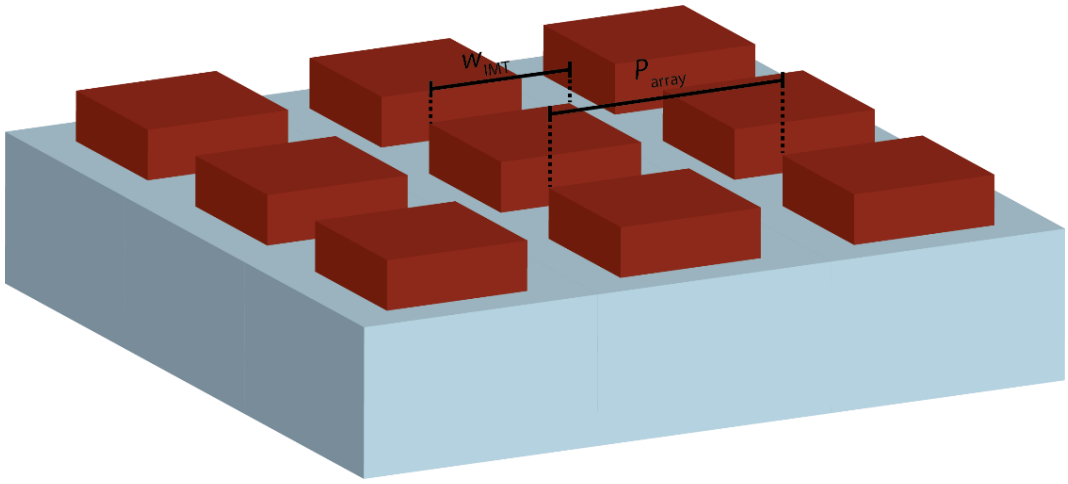

Figure 5.4: Nanopillar array structure.

The structure was fabricated by depositing a VO_2/NbO_2 thin film by VO_2, spin-coating a lithography resist, patterning the nanopillar array on the resist using electron-beam lithography, and finally etching the film using RIE with SF6 gas. SF6 gas will etch both VO_2 and NbO_2 while leaving the Al_2O_3 substrate untouched. The resist acts as a mask, protecting the pillars from etching, during the etching process. Figure 5.5 shows an SEM of one of the fabricated nanopillar structures in NbO_2.

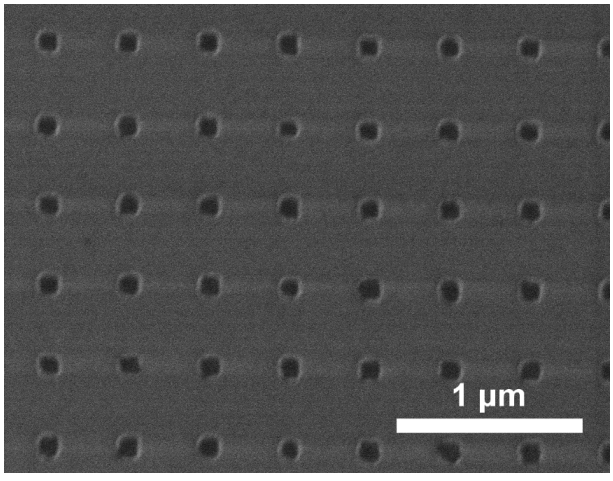

Figure 5.5: SEM of fabricated NbO_2 nanopillar array. Secondary electron SEM image of a nanopillar array fabricated in a 5 nm NbO_2 film with a period 435 nm and a pillar width of 100 nm.

5.2.2 Simulation

The potential to reduce the recovery time of the long-lived modulation was once again demonstrated by simulating the heat dissipation of the proposed structure. Figure 5.6 shows a comparison of the dissipation of heat from NbO_2 nanopillar structures with different pillar widths and a NbO_2 thin-film. From this it can clearly be seen that reducing the pillar width can significantly enhance the rate of heat dissipation.

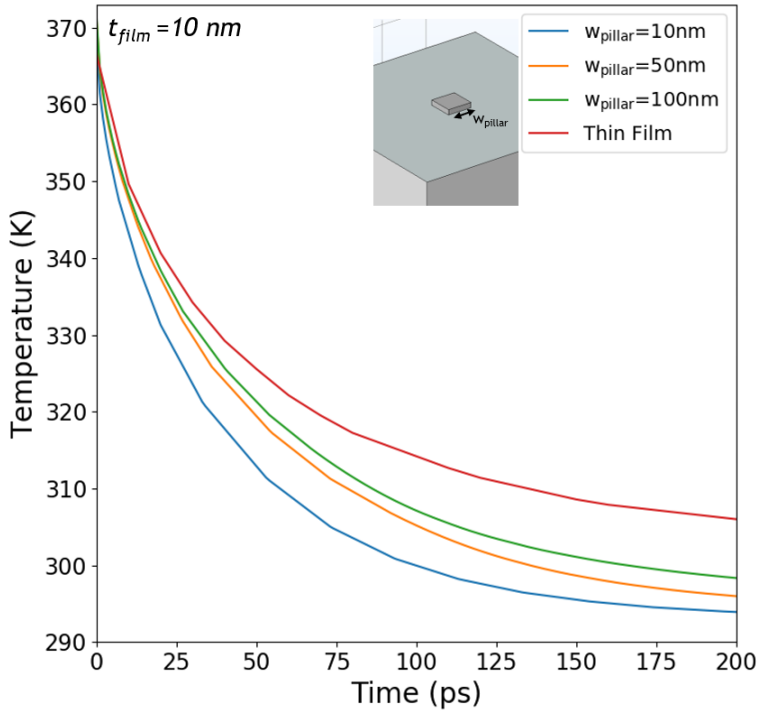

Figure 5.6: Effect of nanopillar width on heat dissipation in NbO_2 nanopillar array. Inset shows a schematic of the simulated structure.

These results show that the heat dissipation rate and thus recovery can be significantly improved through using ultra-thin thin-films and nanostructuring. One limitation of the heat dissipation in both the thin-film structures and nanopillar structures studied here, however, is that heat is only significantly dissipated through the substrate. The diffusion of heat across the VO_2/NbO_2 and Al_2O_3 interfaces is quite efficient because the two crystalline materials are in close contact. Between the VO_2/NbO_2 and the air interfaces, however, the efficiency of heat transport it quite poor. It is expected that coating the VO_2/NbO_2 with another solid material, even one that does not have a particularly high thermal conductivity should help to further enhance the recovery of the long-lived modulation, allowing sub-100 ps recovery rates to be achieved.

Chapter 6 : Modulation Enhancement using Plasmonic Nanostructures

The mid-fluence region of VO_2's photo-induced modulation where VO_2 exhibits a strong modulation as a result of an IMT to a monoclinic metal state is extremely promising for the development of strong modulation all-optical modulators; however, the threshold fluence for this behaviour to be realized is on the mJ/cm^2 order, and this limits the efficiency of the optically-induced modulation. In this chapter, the use of plasmonic nanostructures to concentrate the pump light and reduce the threshold fluence for the mid-fluence monoclinic metal state of VO_2 is investigated. A plasmonic nanohole array comprised of a gold film periodically perforated by VO_2 filled holes is designed, optimized and fabricated, and the photo-induced modulation of the structure is studied.

Plasmonic nanohole arrays are nanostructures consisting of a metal thin-film perforated periodically by subwavelength apertures that may or may not be filled with a dielectric material. Interest in plasmonic nanohole arrays grew when it was discovered that over a resonant wavelength range they exhibit a much higher optical transmittance than would be expected for transmission through a periodic array of opaque subwavelength apertures, a phenomenon known as extraordinary optical transmission (EOT) [78]. EOT has been found to be the result of a cooperative plasmonic effect where surface plasmon polaritons (SPPs) excited by the periodic nanostructure propagate on the surface of the metal thin-film and couple to the local surface plasmon resonance (LSPR) of the sub-wavelength dielectric apertures in the metal thin-film. When the SPPs and LSPR occur at the same wavelength, an enhancement in the transmittance of the nanostructure is observed. In addition to an enhancement in the transmittance of the nanostructure, due to the concentration of light into the sub-wavelength apertures, if the dielectric material in the apertures is absorbing, the absorption is also enhanced [79]. Plasmonic nanohole arrays have been applied as wavelength selective biosensors [80], negative refraction superlenses [81], and metalenses [82], among other things.

The light concentrating and EOT phenonmena exhibited by plasmonic nanohole arrays can both be harnessed to enhance the performance of a VO_2 based thin-film all-optical modulator. Using such structures has two key advantages. First, the pump light used to induce the IMT in VO_2 can be concentrated into the VO_2 to reduce the threshold for the photo-induced IMT. In addition to this, the LSPR resonance of the VO_2 filled nanoholes when VO_2 is dielectric can be matched to the probe light wavelength in order to enhance the transmittance of the

nanostructure when VO_2 is dielectric, thus increasing the contrast between the transmittance when VO_2 is dielectric and when VO_2 is metallic.

6.1 Simulation and Optimization

As the EOT phenomenon is a resonant phenomenon that occurs over a specific wavelength range determined by the structure of a plasmonic nanohole array, it was first necessary to optimize the plasmonic nanohole array. The optimization of the structure was performed by simulating the optical properties of a periodic Au/VO_2 nanohole array using the rigorous coupled wave (RCWA) method using the electromagnetic simulation software RSOFT's DiffractMOD module (Rsoft Design Group, Ossining, USA).

The Au/VO_2 plasmonic nanohole array consisting of a gold thin-film with VO_2 filled square holes arranged in a 2D square lattice that was designed is shown in Figure 6.1. A thickness of 25 nm was chosen to ensure the Au film was sufficiently opaque and that the transmission of light would only occur through the VO_2. The period of the array (P_{array}) was then optimized to match the SPP resonance condition to the wavelength of the pump laser (766 nm). Finally, the width of the VO_2 filled square nanoholes (w_{IMT}) was optimized to enhance the transmittance of the nanohole array when VO_2 is dielectric by matching the LSPR resonance of the nanohole to the probe laser wavelength (1550 nm).

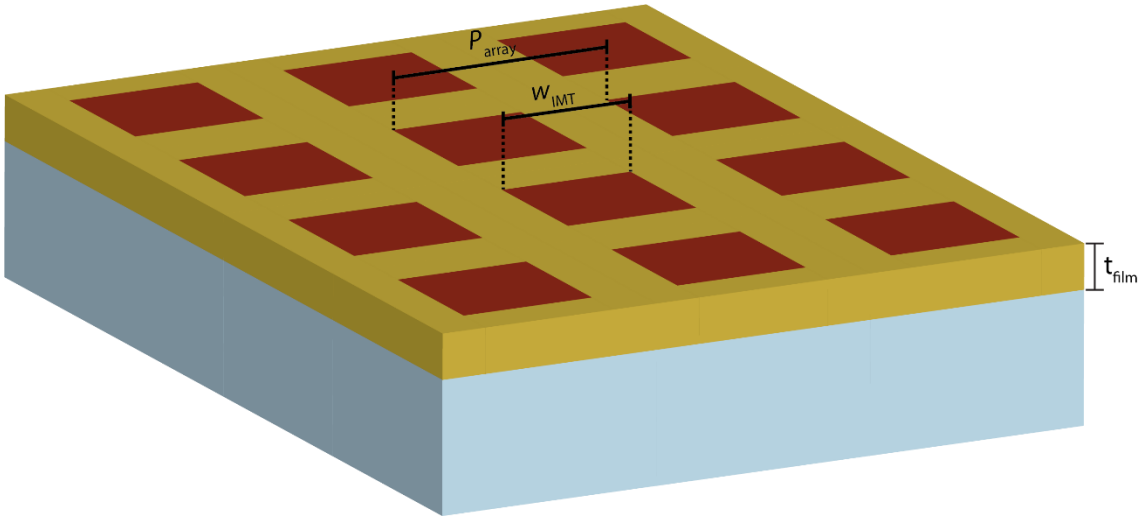

Figure 6.1: Structure of the Au/VO_2 plasmonic nanohole array.

The effect of P_{array} on the SPP resonance condition can be seen in Figure 6.2 below. As the period is increased, the resonance is shifted to longer wavelengths. This is a well-known phenomenon for the excitation of SPP resonances using periodic gratings [83]. SPPs are electromagnetic modes that exist at the interface between a metal and a dielectric; however,

they have an in plane wave-vector slightly larger than the wave-vector of the dielectric material, and hence are not normally excited by incident plane waves. When periodic structures diffract light into different diffraction orders, they add momentum in the direction of the periodicity to the diffracted light which increases the in plane wave-vector by $\Delta k_x = 2\pi m/P$, where m is the diffraction order and P is the periodicity of the structure. Normally incident light can then be coupled to SPPs using periodic structures if the nanostructure period satisfies the following condition [83],

$$P = m\lambda/n_{\mathrm{SPP}}$$

where λ is the wavelength of light to be coupled and n_{SPP} is the effective index of the SPP mode [83]. From this it is clear that the period of the structure and wavelength of light coupled to an SPP by the structure are directly proportional to each other, and therefore the observed behaviour is as expected.

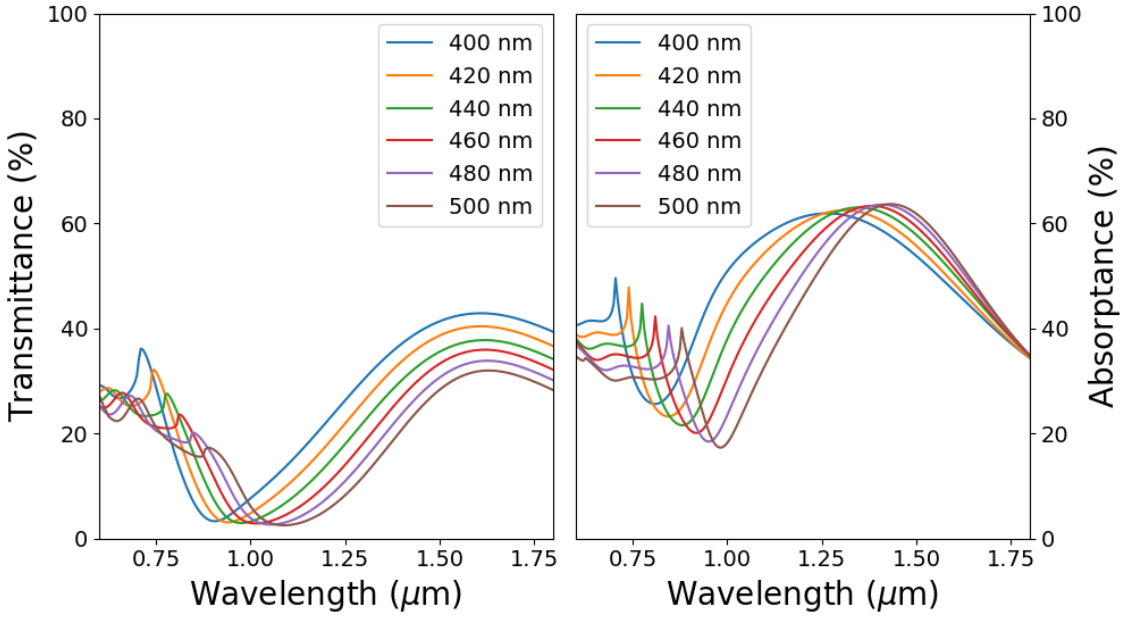

Figure 6.2: Effect of period on optical properties of plasmonic nanohole array. Simulated (left) transmittance and (right) absorptance of the plasmonic nanohole array for varying periods of the structure.

The LSPR resonance that enhances the transmittance of the nanohole array can be observed as a broad transmittance peak in the IR when VO_2 is in the dielectric state, as can be seen in Figure 6.3. From Figure 6.3, it can clearly be seen that as the width increases, the LSPR wavelength shifts to longer wavelengths. In addition, the magnitude of the transmittance increases with increasing hole width; however, this is a result of the increasing fraction of VO_2 in the Au/VO_2 nanohole array and the fact that VO_2 has a much higher transmittance than Au. It is important to note as well that the absorption enhancement caused by the SPP resonance

does not change wavelength when the hole width is increased, and therefore, is clearly solely a result of the structure's periodicity.

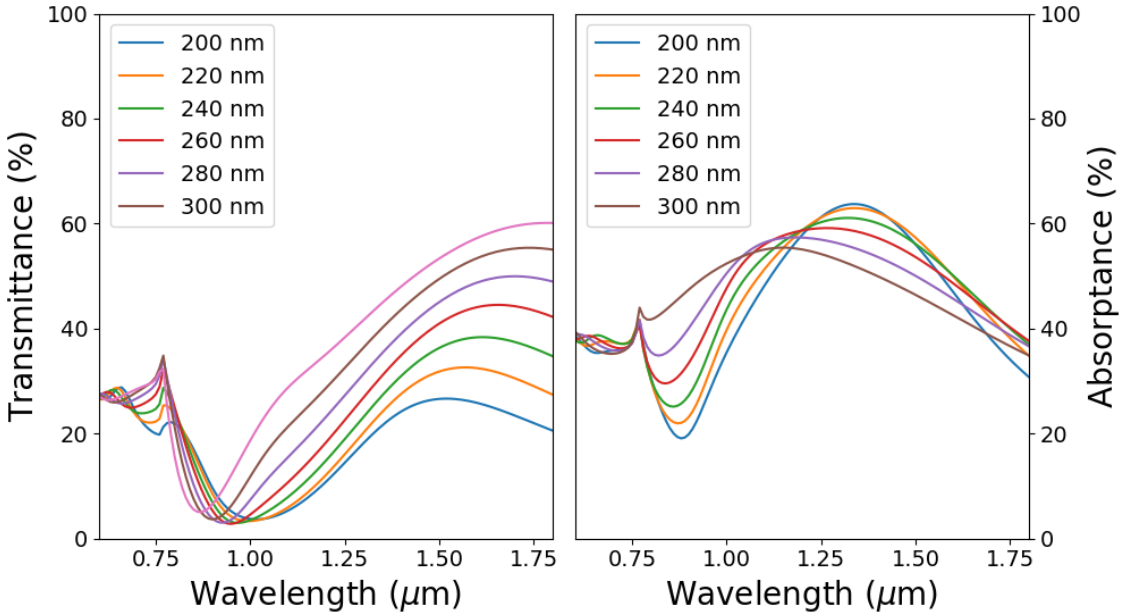

Figure 6.3: Effect of nanohole width on optical properties of plasmonic nanohole array. Simulated (left) transmittance and (right) absorptance of the plasmonic nanohole array for varying widths of the nanoholes.

Through the optimization of both the array period and the nanohole width, it was possible to enhance the absorption of the 766 nm pump laser as well as enhance the transmittance of the 1550 nm probe light used in our pump-probe studies in order to improve the performance of the a thin-film all-optical modulator using VO_2. A comparison of the performance of a VO_2 thin-film and the Au/VO_2 plasmonic nanohole array are shown in Figure 6.4, with the key results summarized in Table 6.1. It is clear that the absorption can be significantly enhanced, with a 6x enhancement in the absorption within the VO_2 being seen for the plasmonic nanohole array as compared to the VO_2 thin-film. The differential transmittance is also enhanced, and, given the smaller fraction of the area consisting of VO_2 (25.6 %), the modulation resulting from the VO_2 IMT is clearly significantly enhanced.

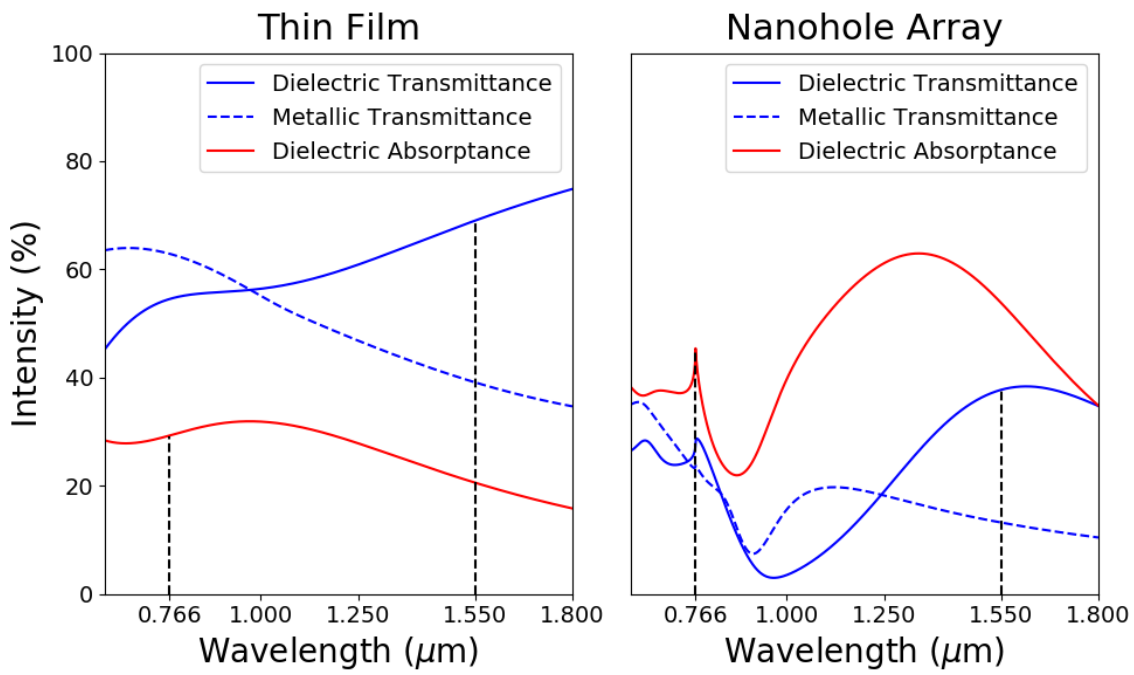

Figure 6.4 : Comparison of the VO_2 thin-film and plasmonic nanohole array modulation performance. (left) simulated absorptance and transmittance when VO_2 is in its dielectric state and transmittance when VO_2 is in its metallic state for a 25 nm VO_2 thin-film. (right) simulated absorptance and transmittance when VO_2 is in its dielectric state and transmittance when VO_2 is in its metallic state for the optimized plasmonic nanohole array.

Table 6.1: Summary of the optical properties of the plasmonic nanohole array and a VO_2 thin-film.

	Nanohole Array in 25nm Au Film (P_{array} = 435 nm, w_{IMT} = 220 nm)	**25 nm VO_2 Thin Film**
T_{1550} Dielectric (%)	37.7	69.0
T_{1550} Metallic (%)	13.1	39.1
ΔT/T (%)	-65.2	-43.3
A_{766} (%)	45.4	29.2
VO_2 Fraction	0.256	1
Normalized A_{766}	177.3	29.2
Absorption Enhancement	6x	

6.2 Fabrication

The fabrication of the Au/VO_2 plasmonic nanohole array was the next step in my study. Using the same method detailed in Chapter 3, a 25 nm thick VO_2 thin-film was deposited on an Al_2O_3 (001) substrate using PLD. Following this, an electron-beam lithography resist (ZEP520A) was spin-coated on top of the VO_2 thin-film at 4000 rpm to obtain an approximately 300 nm thick coating of resist. Using electron-beam lithography with a 110 μC/cm^2 excitation dose and subsequently development in ZED-N50, a periodic square lattice

of resist pillars on top of the VO_2 thin-film was fabricated. This process left the VO_2 underneath the pillars protected with the rest of the VO_2 exposed. Next, the exposed VO_2 was etched using reactive ion etching. SF_6 with no Ar was used as the etching gas, as SF_6 will not Al_2O_3, and this way the substrate can act as an etch-stop after the VO_2 is fully etched. After depositing Au with RF sputtering onto the etched structure, lift-off with ZDMAC was used to remove the remaining resist and the Au deposited on top of the resist. The structure obtained as imaged by scanning electron microscopy (SEM) is shown in Figure 6.5 below.

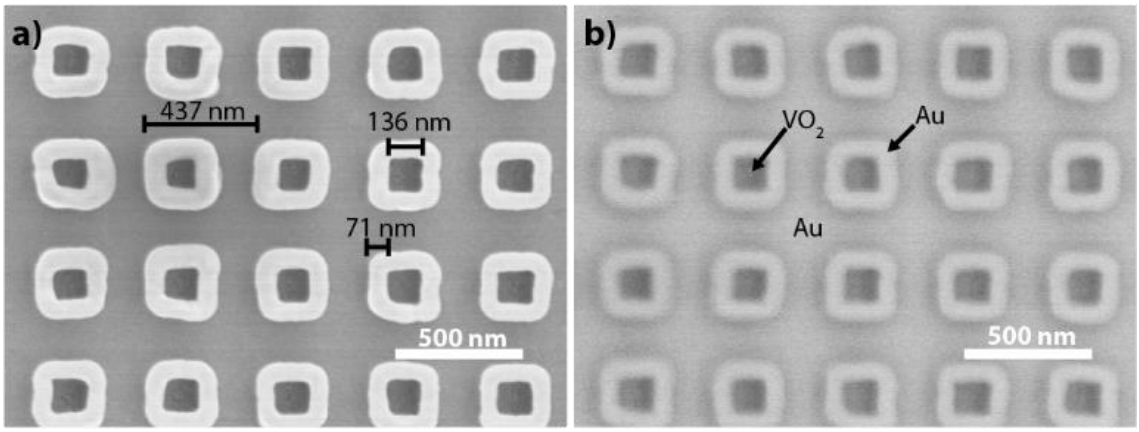

Figure 6.5: Overhead SEM image of the Au/VO_2 plasmonic nanohole array. (left) Secondary electron image. (right) Backscattered electron image.

From the secondary electron (SE) SEM image Figure 6.5a, a periodic structure with three distinct portions can be observed. A flat and uniform background is interspersed by a periodic array of square donuts surrounding recessed structures. Though the measured period of the periodic nanostructure (437 nm) is very similar to the designed 435 nm period, the VO_2 nanoholes have a much different appearance. Since the thicknesses of the VO_2 and Au thin-films deposited were the same, it was expected that a flat surface with some roughness at the interface between Au and VO_2 regions would be obtained; however, a much different structure was obtained in reality. By using back-scattered electrons (BSE) to obtain a material contrast image (Figure 6.5b), the composition of the different portions of the structure can be elucidated. BSEs result from the scattering of incident electrons from the SEM off the nuclei of the sample material, meaning that the signal strength is directly related to the size and charge of the nuclei in the material – materials comprised of atoms with higher atomic numbers have a stronger BSE signal. From Figure 6.5b, we see that both the square donuts and the background film have the same intensity, while the material recessed inside the donuts has a weaker signal. This suggests that the former are composed of the higher atomic number Au, whereas the latter is

comprised of VO_2 whose constituent atoms both have lower atomic numbers. To further clarify the structure, tilted SEM images of the structure, shown in Figure 6.6, were taken.

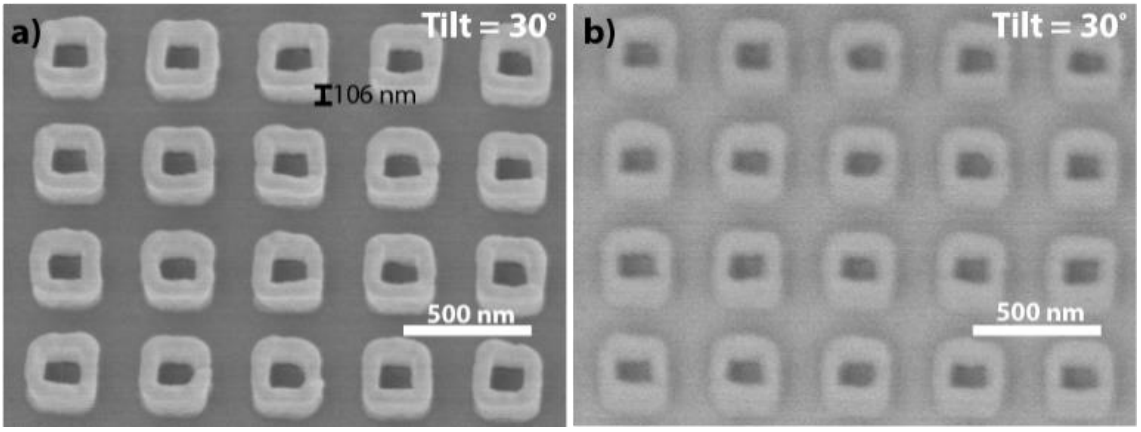

Figure 6.6: Overhead SEM image of the Au/VO_2 plasmonic nanohole array. (left) Secondary electron image. (right) Backscattered electron image.

The tilted SEM images clearly demonstrate that the Au donuts surrounding the VO_2 have a significant height (106 nm); however, it is not clear if the edges of the donuts are on top of the VO_2 or the Au. To clarify this, the structure was cut using focussed ion-beam (FIB) milling and the SEM images were retaken, as seen in Figure 6.7. Here we can see that the walls of the Au donuts sit on top of the VO_2. We can also see that the width of the VO_2 underneath the Au donuts is 224 nm, close to the designed 220 nm. Based on this structure and the fact that the etching rate of the resist is significantly faster than the etching rate of the VO_2, it is likely that during the etching process, the faster etching of the resist resulted in the edges of the VO_2 nanopillars being exposed. Therefore, when the Au was deposited, some was deposited on top of the VO_2 edges and was not removed during the lift-off process. Despite the differences between the actual structure and the designed structure, the periodicity of the plasmonic nanostructure means that the reduction of the IMT threshold and modulation enhancement should still be observable, and so the photo-induced modulation of this structure was examined.

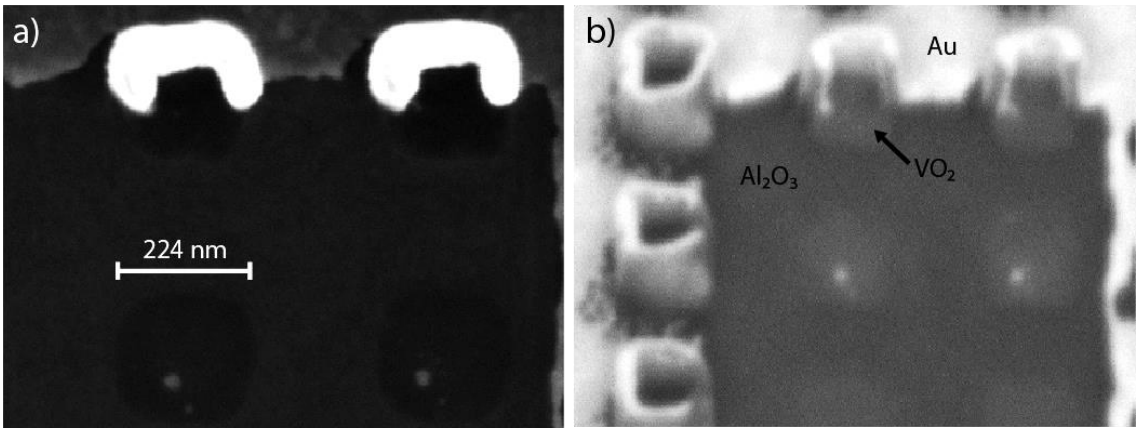

Figure 6.7: SEM image of the nanohole array after etching with FIB. (left) Overhead secondary electron image demonstrating the width of the VO_2 nanopillars. (right) Tilted backscattered electron image demonstrating that the Au donuts are deposited on top of the VO_2.

6.3 Photo-induced Modulation

First, the photo-induced modulation in the transmittance of the plasmonic nanohole array was examined for low pump fluences. The same 766 nm pump wavelength and 1550 nm probe wavelength were used as for the prior thin-film and nanopillar studies. In Figure 6.8, the photo-induced transmittance modulation for the first 8 ps after a 0.35 mJ/cm^2 pump pulse excites the nanostructure can be seen. The response is similar to that for a VO_2 thin-film in the low-fluence regime, with an initial strong decrease in the transmittance immediately after the pump pulse excites the sample, followed by a partial recovery on a fast ps timescale and a slow recovery on a timescale of several hundred ps to several ns. In the specific case of this plasmonic nanohole array, the slow recovery was found to have a time constant of around 1 ns, which is comparable to the time constant found for a VO_2 thin film with a similar thickness as discussed in Chapter 3. Interestingly, the time constant of the short-lived modulation is significantly shorter in nanohole array than the thin-film (260 fs vs. 2 ps). This may be the result of metal quenching of the photo-excited carriers. The similarity between the photo-induced modulation of the Au/VO_2 plasmonic nanohole array and the VO_2 thin-films suggests that the photo-induced modulation is solely a result of the changes induced in the VO_2 and not due to photo-induced changes in the Au portions of the nanostructure.

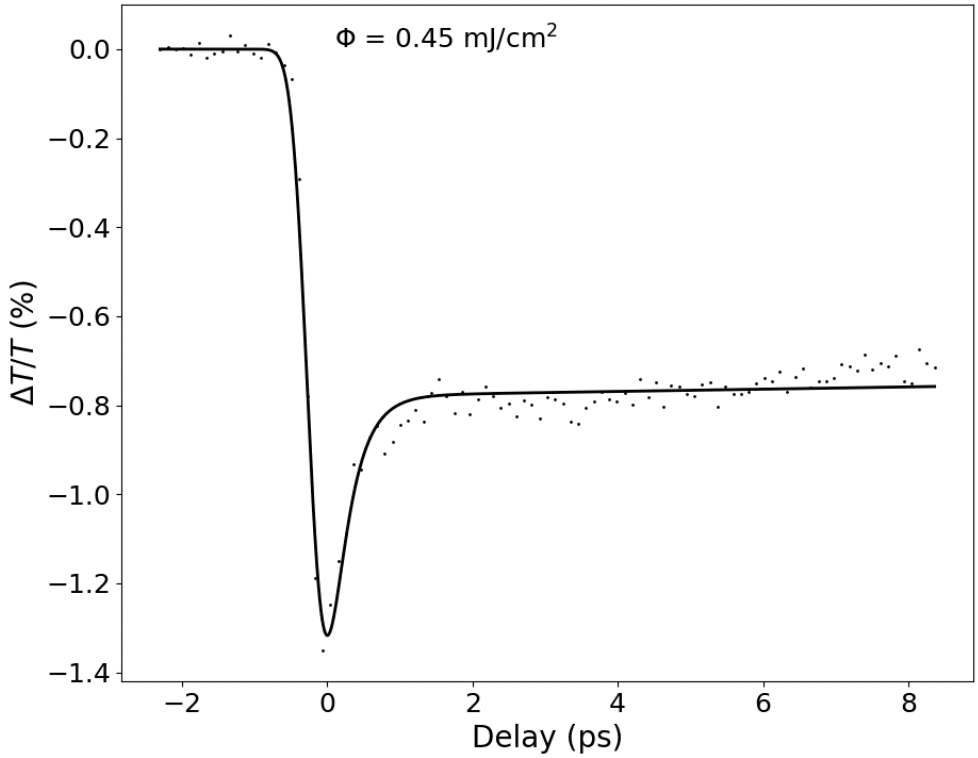

Figure 6.8: Low-fluence differential transmittance of Au/VO_2 plasmonic nanohole array.

6.3.1 Modulation Intensity vs. Pump Fluence

The photo-induced modulation of the plasmonic nanohole array for a range of pump fluences was measured at three different delays in order to understand the threshold behaviour of the plasmonic nanostructure. Once again, the modulation was measured at no delay, when the pump and probe pulses reach the sample at the same time was measure; at a 100 ps delay, where all non-thermal processes have finished and the sample reaches its maximum modulation; and at a 1 ns delay, when the recovery of the film is governed by heat dissipation. To ensure that any threshold reduction and modulation enhancement effects are truly a result of the plasmonic nanostructure and not simply sample-to-sample variability, the nanohole array was fabricate on a portion of a VO_2 thin-film, and the modulation of the nanohole array at the three delays was compared to the modulation of the bare VO_2 thin-film (Figure 6.9).

The modulation at no delay (Figure 6.9 bottom) shows little difference from the thin-film behaviour, with the same linear dependence on the pump fluence.

In the modulation at 100 ps (Figure 6.9 middle), however, three distinct variations can be seen. The first is that the threshold fluence where the modulation deviates from a linear dependence on the pump fluence is reduced significantly by a factor of 2.3x to a pump fluence of only 781 μJ/cm^2. Another clear difference between the thin-film behaviour and the nanohole

array is the reduction of the modulation saturation. The nanohole modulation saturates at a fluence slightly above 2 mJ/cm^2, whereas the thin-film`s modulation does not fully saturate until a much higher pump fluence of 4 mJ/cm^2. Finally, the low-fluence behaviour of the thin-film and nanohole array are also different. Although the maximum modulation of the nanostructure is smaller than the thin-film, in the low-fluence region, the modulation of the nanohole array is larger for the same pump fluence.

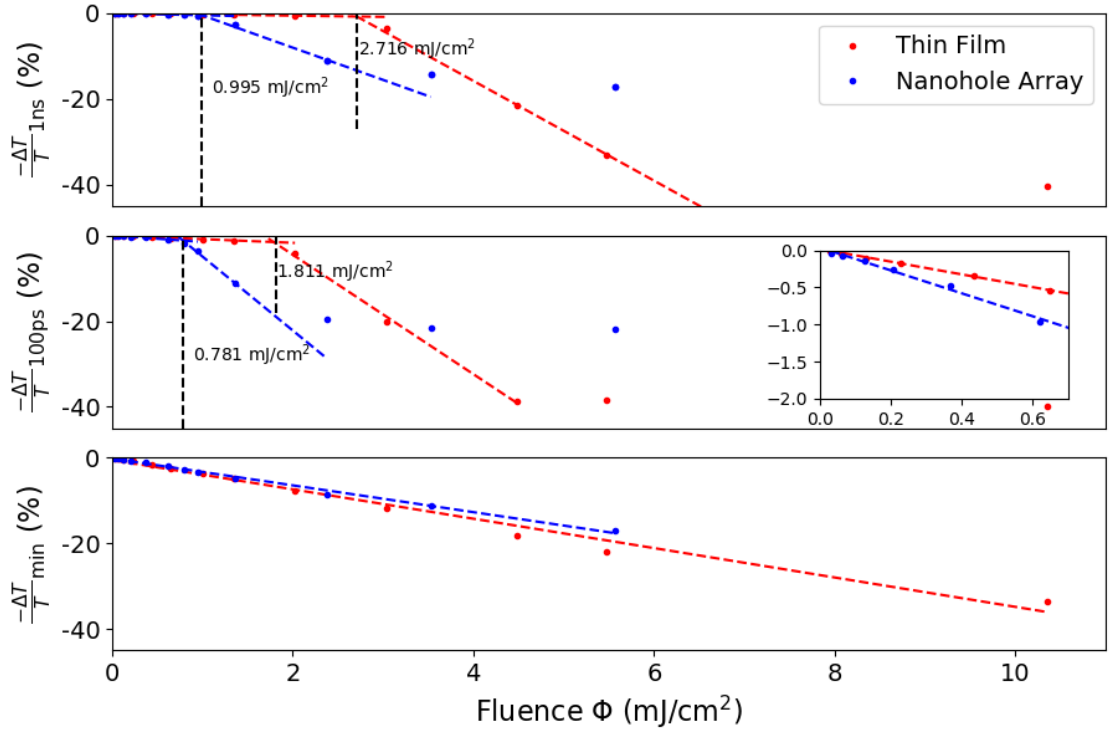

Figure 6.9: Fluence dependence of the transmittance modulation of the plasmonic nanohole array. The transmittance modulation at three delays, the minimum of the short-lived response (bottom), at a 100 ps delay (middle), and at a 1 ns delay (top) are plotted against the pump fluence. The linear low-fluence regime for the 100 ps delay is shown in the inset of the middle plot.

At the longer delay time of 1 ns, we see a similar behaviour to the 100 ps delay time, albeit with a different rate of increase in the delay, and a slightly higher threshold for the non-linearity to appear in the modulation vs. fluence curve. If the ratio of the modulation at 1 ns and 100 ps is plotted against the fluence, as seen in Figure 6.10, we once again see that there is a range of fluences above the threshold for the IMT in which the ratio does not increase, indicating that the recovery time is unchanged and providing evidence for the fast recovery of VO_2 from the monoclinic metal state. Another interesting observation is that the decrease in the ratio before it begins increasing again occurs faster in the case of the nanohole array.

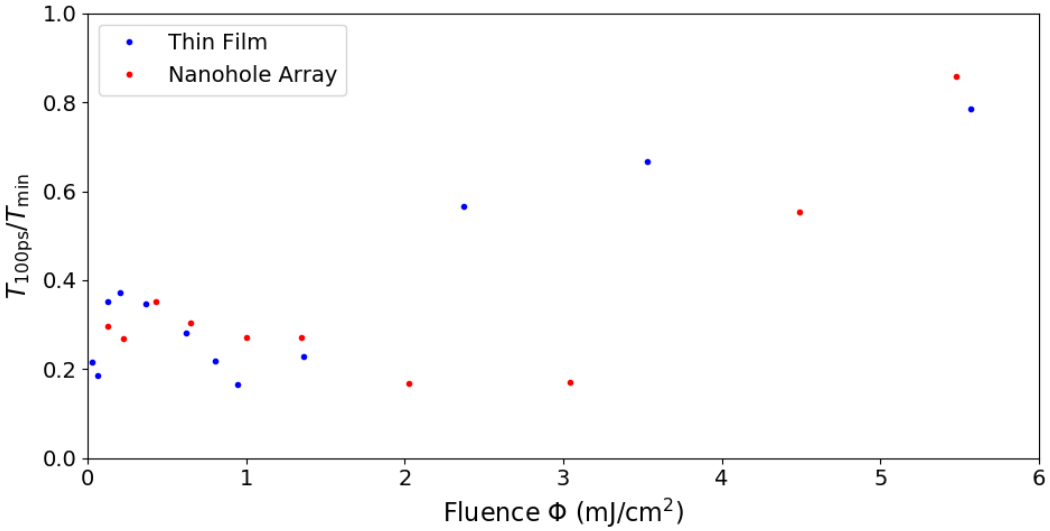

Figure 6.10: Comparison of second threshold for a VO_2 thin-film and the plasmonic nanohole array. The ratio of the modulation at 1 ns and 100 ps for the thin-film and plasmonic nanohole array are compared. A clear earlier onset of the second threshold is observed for the nanohole array.

All of these phenomena taken together clearly indicate that the plasmonic nanohole array effectively concentrates the pump light into the VO_2 thus decreasing all thresholds associated with the IMT and CPT as well as enhancing the modulation observed for a given pump fluence. Unfortunately, due to deviations of the nanohole array structure from the designed structure, enhancement of the maximum modulation was not observed.

6.3.2 Mid-Fluence Regime

The mid-fluence region of the Au/VO_2 plasmonic nanohole array's photo-induced modulation was examined to determine if sub-ns recovery from the monoclinic metal state of VO_2 could be achieved with the plasmonic nanohole array as well. This must be verified, as plasmonic nanostructures often suffer from resistive heating, and this has the potential to cause a thermal IMT at a lower threshold value than previously observed for the thin-film VO_2. The nanohole array was excited with a 1.49 mJ/cm^2 pump fluence that lies within the fast mid-fluence region as measured in section 6.3.1. Figure 6.11 shows the resulting time-resolved differential transmittance measurement. As can be seen, the response consists of an initial fast decrease in the transmittance, followed by a partial recovery on a ps timescale, and then a gradual increase in the modulation up to a maximum modulation at 80 ps after the pump excitation. This is followed by a decay in the modulation on a sub-ns scale. Though full recovery is not achieved at 1 ns, over 75% of the initially induced modulation is recovered after 1 ns. As the final recovery is governed by thermal dissipation, it is expected that the recovery could be further enhanced through the use of a thinner nanohole array, or smaller nanohole

diameters. The use of an alternative plasmonic material with a higher thermal conductivity and lower absorption at 766 nm could further improve both the thermal dissipation and the range over which the monoclinic metal exists as well.

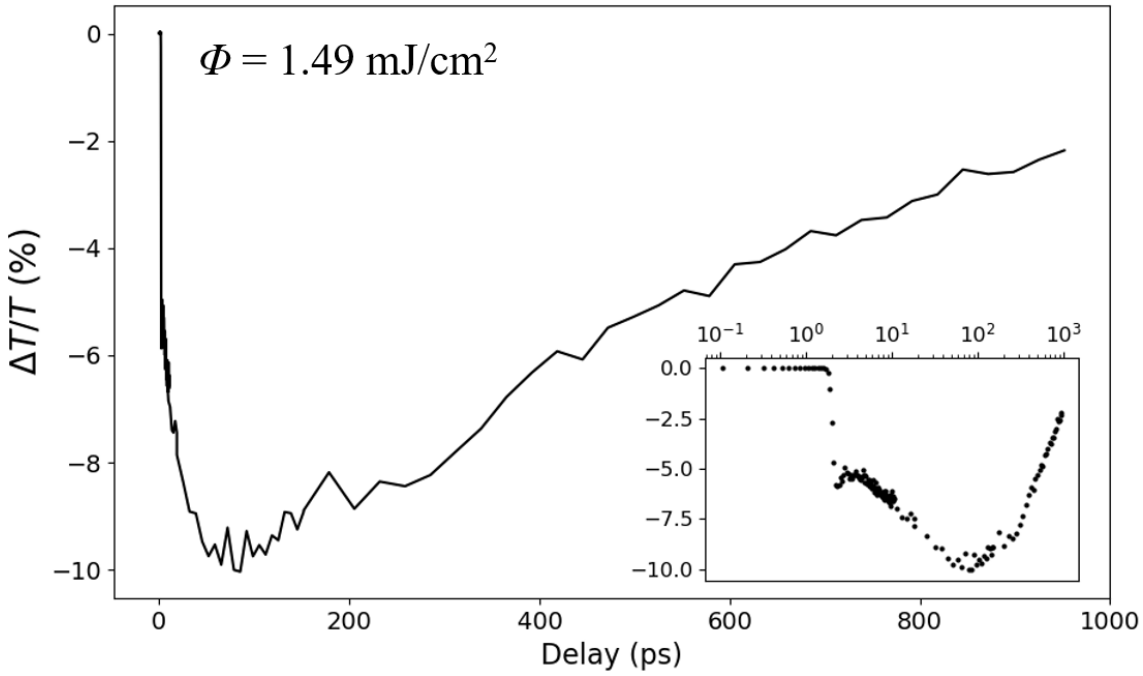

Figure 6.11: Recovery of the nanohole array's modulation in the mid-fluence fast recovery region. The inset shows the modulation with a logarithmic x-axis.

Chapter 7 : All-optical Waveguide-integrated Modulator using VO_2

The results described in the prior chapters clearly demonstrate that high-speed modulation of IMT materials can be achieved through the use of ultra-thin thin-films and nanoscale structuring. It was also demonstrated that the small modulation observed for such materials and the efficiency of optical pumping could be significantly enhanced through the incorporation of plasmonic nanostructures.

In this chapter, an all-optical modulator that uses a plasmonic nanostructure incorporating nanoscale domains of VO_2 in a photonic waveguide-integrated is designed. The design allows for the ultrafast modulation of an optical signal with a large extinction ratio while boasting a small nanoscale size and low insertion loss.

7.1 Modulator Design

The device is comprised of a thin sub-wavelength Au/VO_2 nanostructure that coats a silicon waveguide. This hybrid structure allows an optical pump signal propagating in the silicon waveguide to be concentrated into the VO_2 in order to switch the VO_2 phase, and provides a resonant photonic cavity that enhances the contrast between the transmission of the modulator in the dielectric VO_2 state and the metallic VO_2 state. This design has the potential to realize an all-optical modulator with an extinction ratio (ER) as high as 26.85 dB/μm, while only being 550 nm in length.

As a first step to the development of a high-speed all-optical modulator, an overall device architecture had to be envisaged. This device architecture needed to fulfill three key requirements. The first requirement was that the device should be easy to integrate with CMOS devices and telecommunication devices, the second requirement was that the device should concentrate a pump signal into the VO_2 in order to facilitate an optically induced phase change, and the third requirement was that the structure should be an efficient waveguide for the signal wavelength. To fulfill the first and third requirements, a silicon waveguide, designed for 1550 nm light, was chosen as the base for the modulator.

The devised waveguide structure is illustrated in Figure 7.1a. At the base of the device, is a patterned silicon-on-insulator (SOI) wafer with a Si ridge waveguide designed for a 1550 nm signal light. On top of the Si ridge waveguide is a nanostructure coating of Au and VO_2 that can trap a pump light propagating through the silicon waveguide into the VO_2. The Au/VO_2

nanostructure coating was made sub-wavelength and periodic in order to provide an effective waveguide medium for the efficient propagation of the 1550 nm signal light. The possibility of creating an effective waveguide medium from a subwavelength nanostructure has been demonstrated in the literature for Si/Air [84], and in this work we have applied the same principle to an Au/VO_2 nanostructure in order to form an effective hybrid plasmonic-photonic waveguide.

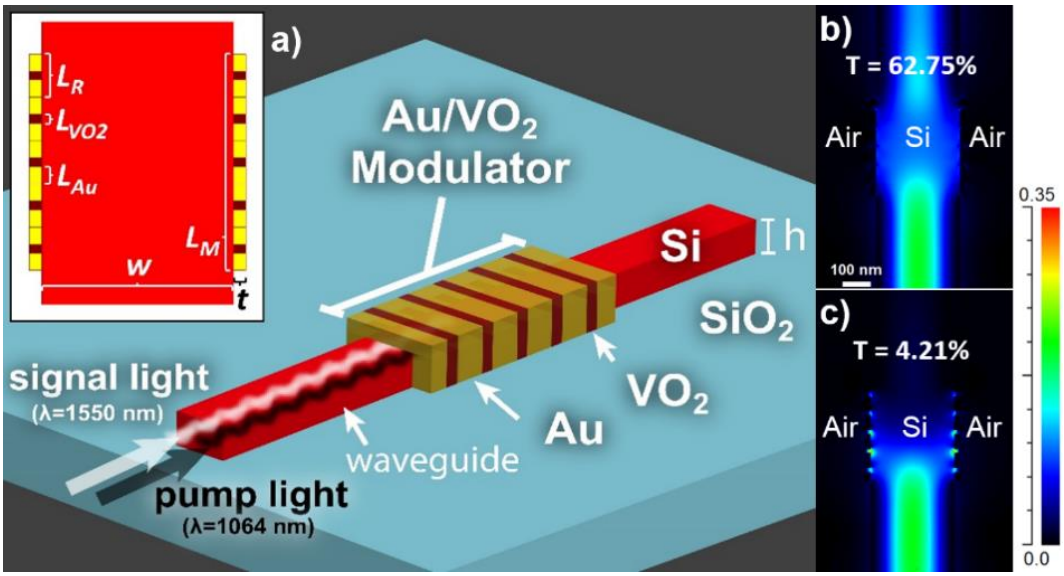

Figure 7.1: Hybrid VO_2 all-optical modulator. a) 3D waveguide structure, illustrating pump and signal light injection, b,c) Poynting vector magnitude when VO_2 is b) dielectric, and c) metallic, for a 2D slab waveguide modulator.

In the proposed design, there are a large number of parameters that affect the performance of the modulator, including the VO_2 length (L_{VO2}), the Au length (L_{Au}), the number of periodic elements in the device (N), the total modulator length (L_M), and the waveguide width (w), height (h) and nanostructure coating thickness (t). The waveguide width and height were fixed at 320 nm and 300 nm respectively in order to ensure single mode operation with the electrical field polarization being primarily horizontal. The thickness of the coating was fixed at 20 nm as it is understood that optical pumping of VO_2 induces a complete metal-insulator transition in individual VO_2 grains [85], and a 20 nm thickness will ensure each VO_2 domain is comprised of only a single crystal grain. In order to better understand the physical processes governing the performance of the modulator device and the impact of the other parameters, a 2-dimensional analogue to the 3-dimensional waveguide was studied in detail and optimized in the following section. The impact of the VO_2 and Au ratio in the modulator, L_M, and L_R were studied and understood clearly based on the allowed photonic and plasmonic modes of the device. An ideal pump light wavelength was then determined. The Poynting vector magnitude and the transmission of the optimized 2D modulator when the VO_2

is in the dielectric state and metallic state are shown in Figure 7.1b and Figure 7.1c respectively. The ratio of the transmittance in the dielectric state (62.75%) to the transmittance in the metallic state (4.21%) corresponds to an ER (ratio of the transmittance in the on state to the transmittance in the off state) of 23.98 dB/μm. Finally, using the understanding developed from the study of the 2D simulation, a 3D simulation was designed and optimized.

The proposed nanostructure represents a CMOS compatible design that can be fabricated using standard nanofabrication procedures. Standard electron-beam lithography of an SOI wafer can be initially used to define the silicon waveguide. Following this, deposition of the VO_2, patterning with e-beam lithography and etching with reactive ion etching (RIE) can be done to create a sub-wavelength VO_2 grating. After this, Au deposition and lift-off of the gold can be performed to obtain the Au/VO_2 coated silicon waveguide. The possibility of achieving a high-quality sputtered film on the sidewalls of Si was demonstrated in previous work [86].

7.2 Optimization

7.2.1 Modal Analysis

A 2D optimization of the modulator structure was first performed in order to develop a clear understanding of the governing factors that determine the modulator performance. Simplifying the model to a 2D simulation makes the waveguide resonances much more evident. Before the proposed modulator structure could be optimized however, an understanding of how the optical modes propagate in the uncoated, Au coated and VO_2 coated waveguides needed to be developed. For this purpose, a modal analysis was performed using the finite-difference-time-domain technique (FullWAVE, Rsoft Design Group, Ossining, USA). The calculate mode indices and mode profiles for a 320 nm wide slab waveguide with no coating, an Au coating, a dielectric VO_2 coating and a metallic VO_2 coating are shown in Figure 7.2. Refractive indices for the dielectric and metallic VO_2 states were taken from a previous article [87], and indices for Au [88], Si [89] and SiO_2 [90] were taken from the literature. For the uncoated silicon waveguide, and both the metallic phase and dielectric phase VO_2, the propagating modes are photonic modes with effective indices near the silicon waveguide index of 2.607. The drastic difference between the imaginary component of the effective index for the metallic and dielectric VO_2 indicates that the mode is far more lossy in the metallic VO_2 case, which will result in a large contrast between the transmission of a metallic VO_2 coated waveguide and a dielectric VO_2 coated waveguide. It is evident from the electric field distribution of the Au

coated silicon waveguide mode that the mode is a plasmonic metal-insulator-metal (MIM) waveguide mode with a high effective index. The high effective index is characteristic of plasmonic modes, and allows the device size to be reduced [91].

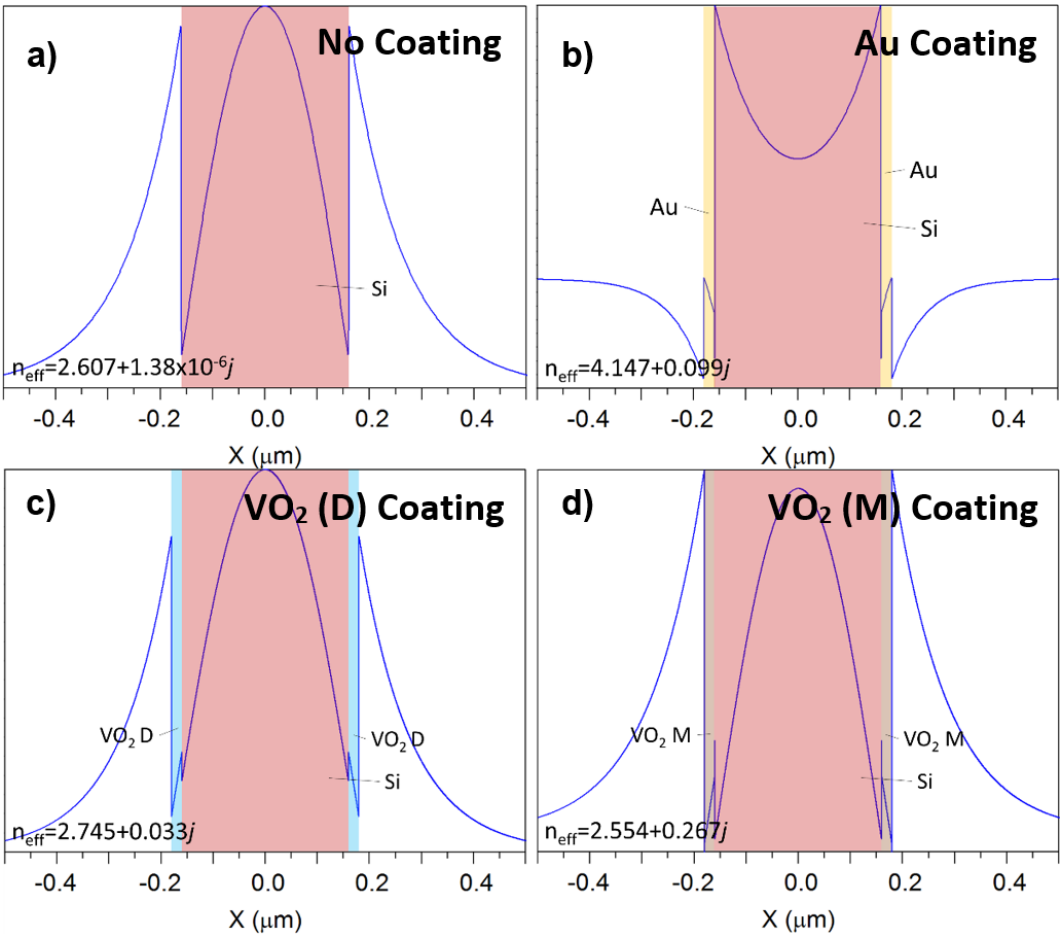

Figure 7.2: Effective modes for waveguide segments in hybrid all-optical modulator. The effective mode indices and modal field distributions of the TM_0 mode for a 320 nm wide silicon slab waveguide, with a) no coating, b) a 20 nm thick gold coating, c) a 20 nm thick coating of VO_2 in the dielectric phase of VO_2, and d) a 20 nm thick coating of VO_2 in the metallic phase of VO_2.

We subsequently demonstrated (Figure 7.3) that the waveguides described above can form resonant cavities that either enhance the transmission or reflection of the waveguide depending on the effective optical length of the waveguide. In the case of the Au coated waveguide, the calculated effective index was 4.147+0.099*j*. Based on this value, the effective longitudinal wavelength for 1550 nm light within the waveguide is approximately 374 nm. It can be expected that light reflected from the ends of the waveguide will interfere with each other, and that the transmitted and reflected intensity (*T* and *R* respectively) will depend on the length of the waveguide. Where a minimum or maximum in the reflection of the waveguide is found, we expect another when L_M is $\lambda_{eff}/2$ longer, as this will correspond to an optical path length difference of λ_{eff}, where the optical phase must be the same. For the Au coated

waveguide, we therefore expect that if the reflectance is plotted against the waveguide length (Figure 7.3b), the distance between two reflectance peaks should be approximately 187 nm. The value obtained in simulation was 185 ± 20 nm, and therefore fits this explanation. For the dielectric VO_2 coated waveguide (Figure 7.3c), the value predicted based on the effective index was 282 nm, and the value obtained in simulation was 270 ± 20 nm. For the metallic VO_2 coated waveguide (Figure 7.3d), the predicted value was 303 nm, and the obtained value was 295 ± 20 nm. These results clearly indicate that the modulator can act as a resonant cavity, for which the total length of the modulator is important in determining the transmissivity, and hence efficiency of the modulator.

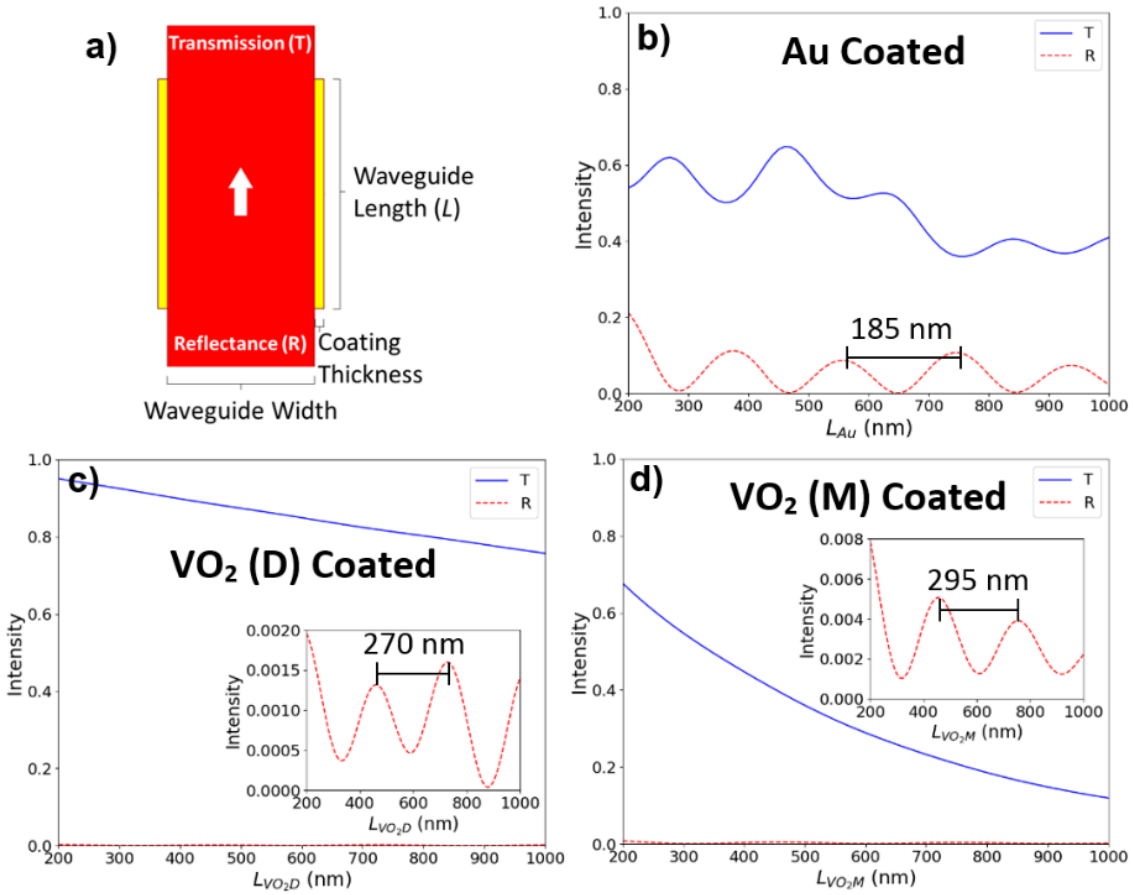

Figure 7.3: Model analysis of Au, VO_2 and bare waveguide structures. a) Illustration of the simulated 2D waveguide structure. Simulated reflectance and transmittance of waveguides composed of a silicon core and a thin film on either side of the silicon, where the thin film is b) gold, c) dielectric VO_2, or d) metallic VO_2 are shown in b), c) and d). Insets in c) and d) show reflectance.

This phenomenon was subsequently applied to the hybrid Au/VO_2 coated nanostructure to optimize the effective optical length of the entire modulator structure, and thus maximize the transmission when VO_2 is in its dielectric state, in order to obtain a high ER modulator.

7.2.2 2D Optimization

In order to determine the ideal modulator parameters and understand the underlying physical principles of the device, we optimized three main parameters. The first parameter was the ratio of L_{Au} to L_{VO2} in the periodic element, the second was the number of periodic units in the modulator, and the final parameter was the length of the individual periodic units. Since the sub-wavelength periodic elements will behave as a single effective waveguide, the initial Au/VO_2 ratio optimization (Figure 7.4b) was performed in order to determine the ideal waveguide medium for the modulator. Although the ER will intuitively increase overall as the modulator length increases, it was expected that there would be an optimal length of the device for which a maximal ER per unit length would be achieved. To determine this length, the dependence of the ER per unit length on the number of periodic units was characterized in Figure 7.4c. Finally, it was understood from the simulations in Figure 7.3 that the total length of the modulator would have a significant impact on the transmittance of the device, and therefore in order to further optimize the performance, the length of the periodic elements was varied, without changing the number or composition of the units. The results for this are shown in Figure 7.4d.

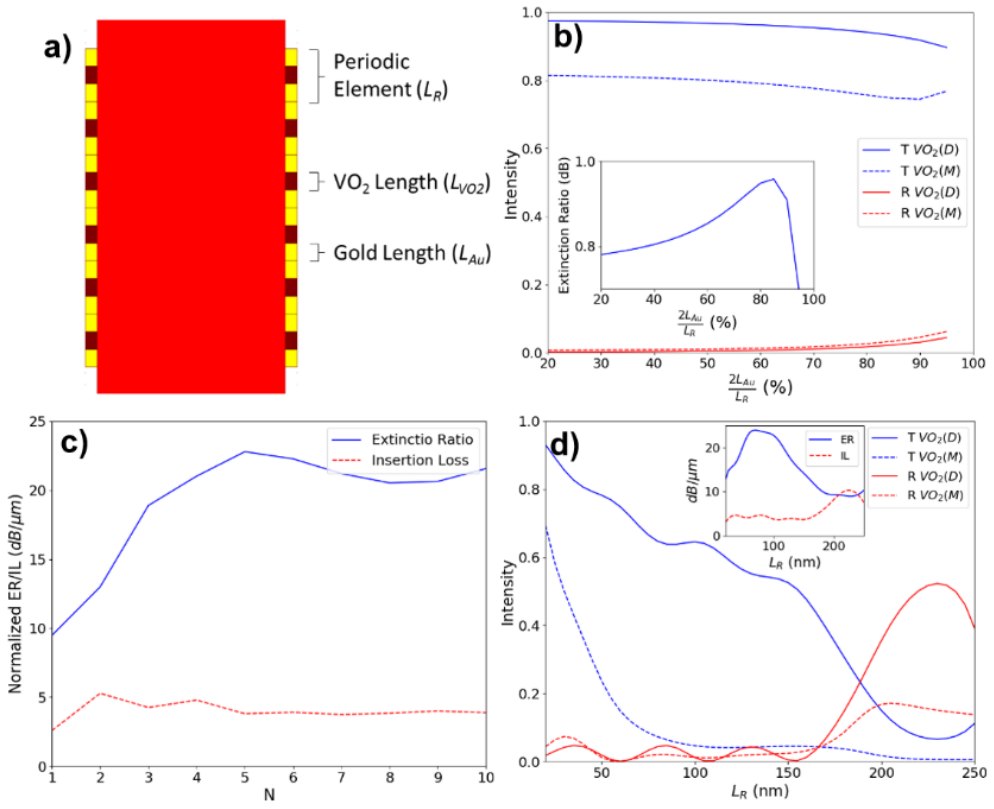

Figure 7.4: Optimization of the 2D modulator structure. a) Illustration of the modulator structure, showing the definition of one periodic element, the gold length and the VO2 length. b) Change in the transmittance and reflectance of the modulator as the percentage of gold in a 100 nm long single periodic element modulator is changed. The inset of b) shows the extinction

ratio for the single unit modulator. c) Extinction Ratio and Insertion Loss for modulators with a periodic element length of 100 nm, a periodic element that is 80% (80 nm gold, with 20 nm VO2) gold, and a varying number of periodic elements. d) Transmittance and reflectance for a five periodic element modulator with 80% gold periodic elements, and a varying periodic elements length, with the inset shown the corresponding ER and IL.

The periodic unit length (L_R), the length of the VO_2 segment in the periodic element (L_{VO2}), and the length of the Au segment in the periodic element (L_{Au}) are illustrated in Figure 7.4a. Figure 7.4b shows that dependence of the transmittance and reflectance of a modulator formed of a single 100 nm periodic element on the percentage of gold (as compared to VO_2) in the periodic element. It was found that for a periodic element composed of 85% gold, the ER ratio of the modulator was maximized. In addition to this conclusion, however, an unexpected result was found. Despite the metallic VO_2 mode being more lossy than the Au mode, the transmission of the metallic VO_2 mode decreases as the portion of Au in the periodic unit increases. This can be explained by two phenomena. First, the metallic VO_2 index is very close to the Si waveguide index whereas the Au effective index is much larger, and therefore as the portion of Au in the periodic unit increases, the effective index of the periodic element as a whole becomes larger and the back reflection from the Si-modulator interface increases. Second, the plasmonic mode of the Au coated portion of the modulator actually helps to concentrate the light in the VO_2 and enhance the absorption. This can clearly be seen in Figure 7.1c, where the pointing vector magnitude is evidently much stronger in the VO_2 regions than the other regions of the modulator.

Following the optimization of the Au/VO_2 ratio, the number of periodic units in the modulator was optimized. Although periodic element with 85% Au were found to be the ideal choice, for the periodic unit optimization and all further steps, a ratio of 80% was used. This was done to prevent the VO_2 length from being excessively short and impractical for fabrication. From Figure 7.4c it can be seen that a modulator composed of five, 100 nm long, periodic units is ideal for obtaining an optimal ER per unit length.

The final parameter optimized was the length of the periodic units, denoted as L_R. The periodic element length was swept from 20 nm to 250 nm, and the transmittance and reflectance of the modulator in the metallic and dielectric VO_2 states were determined. In both the dielectric and metallic VO_2 state, there is an overall decrease in the transmittance as the periodic element length increases. This is simply a result of the increasing length of the lossy waveguide. In the dielectric VO_2 state, however, there is additionally a periodic oscillation to the transmittance and reflectance of the modulator. This can be attributed to the resonant length effect described in section 7.2.1, the effective index of the modulator can be approximated as a weighted

average [84] of the dielectric VO_2 coated and Au coated waveguide indices, ($0.8n_{Au}+0.2n_{VO2} = 3.867 + 0.0858j$). Based on this index, and the fact there are 5 periodic elements, we expect reflectance peaks to be separated by a difference in L_R of 40.1 nm. In Figure 7.4d, the separation between reflectance peaks is 45 ± 10 nm, which supports this conclusion. By taking advantage of this resonance, at an optimized length of 70 nm for the periodic elements, it was possible to obtain an ER of 23.98 dB/μm. The insertion loss (IL), which is simply the transmittance of the on state converted to a dB scale, was also exceptionally low at 1.6 dB (4.56 dB/μm). The high amplitude reflectance peak seen at a periodic unit length of 230 nm is a result of the periodic unit no longer being sub-wavelength in size. At this point, each periodic unit is on the order of a wavelength in length, and the modulator behaves as a Bragg reflector.

7.2.3 Pump Wavelength

As a final step to the optimization of the 2D waveguide modulator, a pump light wavelength had to be chosen. Recent theoretical work suggests that the optically induced VO_2 phase transition is caused by a critical density of photo-excited carriers in the VO_2 causing an instantaneous collapse of the VO_2 bandgap, and the onset of metallic behavior [52]. Based on this, the absorption of the pump light in the VO_2 region was used as a metric for determining the ideal pump light wavelength. It was also predicted that because the Au/VO_2 nanostructure consists of many metal-dielectric-metal nanogaps, there should be a resonant wavelength for which light is coupled strongly to this cavity. In order to find this wavelength, the optimized modulator was excited by a varying wavelength, and the absorption in the VO_2 was monitored (Figure 7.5). For a pump light wavelength of 1050 nm, an absorption peak was observed. A pump wavelength of 1064 nm was chosen due to the ready availability of this wavelength. The spatial distribution of the absorption for a 1064 nm pump light is shown in Figure 7.5b.

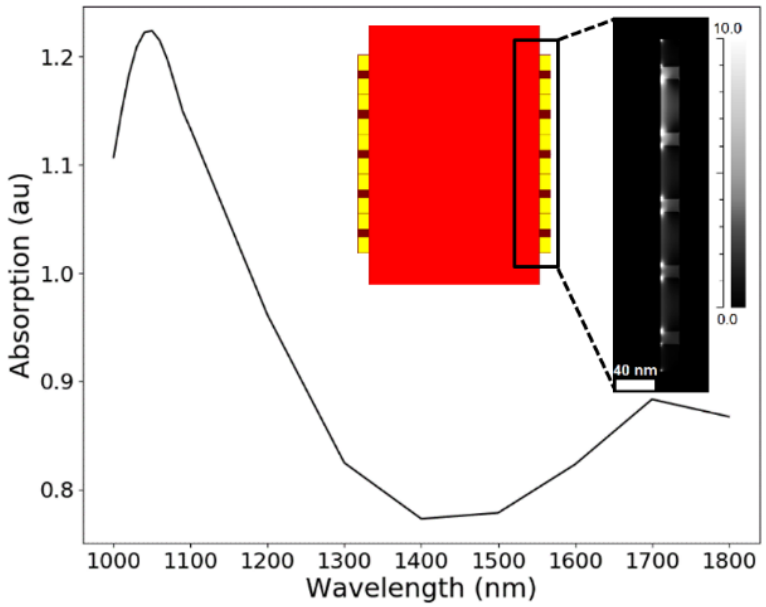

Figure 7.5: Pump light wavelength optimization. a) Total absorption of a pump light in VO_2 as a function of pump wavelength. b) Absorption distribution in the modulator for a pump wavelength of 1064 nm.

7.2.4 3D Optimization

Using the same optimization process used for the 2D slab modulator, the periodic element length, number of periodic elements and periodic element composition of a 3D modulator (Figure 7.1a) were optimized. In this design, the Si waveguide height and width were kept at 300 nm and 320 nm respectively. After optimization, ideal number of periodic elements, and Au/VO_2 ratio was found to be the same as for the 2D modulator (5 and 80% Au). However, after optimizing the periodic element length (Figure 7.6a), an optimal length of 110 nm was found, for which an ER of 26.85 dB/μm, with an IL of only 7.17 dB (13.04 dB/μm), was obtained. When the VO_2 is in its dielectric state, the modulator has a transmittance at 1550 nm of 19.22%, which is changed to 0.64% when the VO_2 is in its metallic state. With a total device length of only 550 nm, this device is comparable to other modulators in the literature [36,39,92,93], [37] and has the added benefit of being optically pumped. In Figure 7.6b and Figure 7.6c, the Poynting vector magnitude of 1550 nm light propagating through a horizontal cross section at the center of the modulator when the VO_2 is in its dielectric state (Figure 7.6b) and metallic state (Figure 7.6c) is shown. The focusing of the signal light into the metallic VO_2 is evident by the strong Poynting vector magnitude in the vicinity of the metallic VO_2. The inset of Figure 7.6c, where the absorption on one side of the modulator is shown, additionally demonstrates that a pump light at 1064 nm is strongly absorbed in the VO_2 and therefore can be used to induce the metal-insulator transition in the VO_2 through the generation of photo-excited carriers.

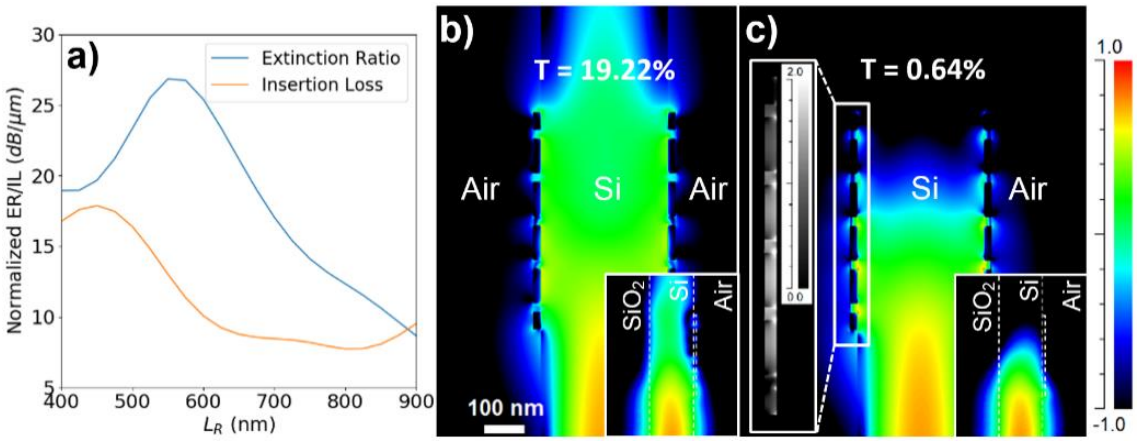

Figure 7.6: 3D modulator performance. a) ER and IL in dB/μm as a function of periodic element length. At the optimal length of 110 nm, ER of 26.85 dB/ μm is achieved. The log scale Poynting vector magnitude for a horizontal cross section through the middle of the Si waveguide is shown in b) for the dielectric VO_2 state and c) for the metallic VO_2 state. Insets in the bottom right of b) and c) show the Poynting vector magnitude in a vertical cross through the center of the waveguide. The inset on the left in c) shows the absorption distribution on the left of the horizontal cross-section of the modulator for a 1064 nm pump light.

7.3 Conclusion

In this chapter, a 2D slab waveguide and a 3D ridge waveguide hybrid photonic-plasmonic all-optical modulator were designed and optimized. Through an in-depth study of the 2D slab waveguide modulator, it was determined that the key factors affecting the performance of the modulators were the ratio of the Au/VO_2 segment length, the number of Au/VO_2 periodic elements in the modulators, and the total length of the modulators. By optimizing these three parameters, a 3D modulator design with an ER of 26.85 dB/μm and an IL of only 7.17 dB was achieved. The design was also found to efficiently concentrate pump light at 1064 nm into the VO_2 regions, thus enabling an optically induced metal-insulator transition in the VO_2.

Chapter 8 : Conclusions and Future Work

The goal of this thesis was to study the photo-induced modulation of IMT materials in thin-films and photonic and plasmonic nanostructures. In particular, the recovery processes that occur after the photo-induced modulation of IMT materials and the timescale of these recovery processes was a major area of focus for this thesis. A definitive answer as to how fast IMT materials could be modulated, how strong their photo-induced modulations could be, and whether or not their photo-induced response could be enhanced was sought after.

In the pursuit of this goal, a high-temporal resolution and low-noise micro pump-probe spectroscopy setup was designed and built. The setup has the capability of studying the time-resolved optical properties of thin-film, nanostructure and waveguide-integrated devices on a femtosecond timescale with high fidelity. A unique pump-repump system was also integrated to study the linearity and maximum modulation speed of all-optical modulator devices.

Through the study of VO_2 and NbO_2 thin-films, a deeper understanding of the photo-induced modulation of both materials was developed. It was determined that the short-lived modulation in the transmittance and reflectance of both materials is primarily the result of photo-excited carrier induced band gap shrinkage for the NIR wavelength range. In the low-fluence regime, the long-lived modulation of both materials was also determined to be a result of photo-thermally induced changes in their lattice temperatures and the associated thermo-optic changes in their refractive indices. As a result, the low-fluence recovery time was determined to be governed by heat-dissipation away from the thin-film materials. A unique mid-fluence region was found for VO_2 where a non-linear increase in the long-lived modulation is observed while fast sub-ns recovery can still be achieved. This mid-fluence region was found to correspond to the recently discovered mid-fluence region where VO_2 undergoes a photo-induced transition to a monoclinic metal phase without undergoing a CPT to its high-temperature rutile phase. Finally, it was found that a full IMT and therefore a saturation of VO_2's optical modulation can be achieved within this mid-fluence region, but it was also found that a structural bottleneck in the recovery of VO2 from the monoclinic metal phase on the order of 10s of ps exists. This demonstrates the separate nature of the IMT and CPT and shows the possibility for strong all-optical modulation at up to GHz speeds using the mid-fluence region of VO_2 if thermal management is sufficient to quickly dissipate heat.

With the realization that the long-lived modulation recovery is limited by heat-dissipation for both VO_2 and NbO_2, the maximum modulation speed of both materials was

investigated through the use of ultra-thin thin-films and nanostructures. Recovery times as fast as approximately 100 ps for VO_2 and 200 ps for NbO_2 were demonstrated. The use of plasmonic nanostructures to reduce the threshold for VO_2 mid-fluence region was also investigated, where it was found that plasmonic nanostructures can effectively concentrate a pump signal into VO_2 and reduce the threshold for the photo-induced IMT to the monoclinic metal phase.

Finally, the potential of VO_2 based all-optical modulators was demonstrated through the design and optimization of a waveguide-integrate all-optical modulator. A sub-wavelength Au/VO_2 nanostructure was used to take advantage of potential for low-threshold modulation using plasmonic modes and enable high-speed modulation. Through the optical simulations, the structure of the all-optical modulator was optimized and a device with a predicted extinction ratio of up to 26.85 dB/μm and a device size as small as 500 nm was designed.

This work clearly demonstrates the potential of IMT based all-optical modulators to not only achieve strong modulations in nanoscale sizes, but also achieve as fast as GHz speeds. Unfortunately, it was determined during this study that the long sought-after sub-ps modulation speeds of VO_2 using the monoclinic metal phase are not possible; however, the demonstration that the IMT can be fully triggered, inducing a strong and saturated modulation, while maintaining sub-ns recovery times is an exciting result. Further studies of the mid-fluence region of VO_2 and recovery from the monoclinic metal phase should be undertaken in order to determine the limitations of the photo-induced monoclinic metal phase.

In particular, heat dissipation was found to be a major limiting factor in the complete recovery of VO_2's modulation after a photo-induced transition to the monoclinic metal phase. As the pump laser used in this experiment has a much higher energy than the bandgap of VO_2, a large amount of heat energy is generated in the VO_2 after the pump laser is absorbed. Using a longer wavelength for the excitation of the VO_2 should significantly reduce the thermal load on the VO_2 and improve the recovery time. This could also help to elucidate whether the monoclinic metal phase is induced by a critical photo-excited carrier concentration, a critical phonon concentration or simply by the VO_2 lattice temperature reaching 67ºC. For all-optical modulator devices, the use of both a telecom wavelength probe and pump would also be highly beneficial.

In addition to continuing the study of the photo-induced modulation of VO_2, devices harnessing the mid-fluence region of VO_2's photo-induced modulation should be explored.

One particularly interesting application is in neuromorphic computing and memristors. The ability to control the lifetime of the monoclinic metal phase through pump fluence is extremely useful in neuromorphic computing, where the ability for individual switches to hold a "memory" of the signals that have passed through them is extremely important. Since the modulation intensity of VO_2 can saturate in the mid-fluence and only the lifetime of the modulation increases after this saturation, fluence can be used as a control over how long a VO_2 based all-optical modulator holds its modulated state, giving a VO_2 based all-optical modulator an effective "memory".

In closing, the study of the photo-induced modulation of VO_2 and NbO_2 thin-films and nanostructures given in this work has the potential to significantly influence not only well established fields such as telecommunications, but also new burgeoning fields such as neuromorphic computing.

References

[1] K. Shailendra and A. G., Int. J. Adv. Res. Artif. Intell. **3**, (2014).

[2] E. Kasper, H. Kibbel, H. J. H. Herzog, and A. Gruhle, Jpn. J. Appl. Phys. **33**, 2415 (1994).

[3] C. N. Ironside, Contemp. Phys. **34**, 1 (1993).

[4] W. Van Heddeghem, S. Lambert, B. Lannoo, D. Colle, M. Pickavet, and P. Demeester, Comput. Commun. **50**, 64 (2014).

[5] M. Chui, M. Loffler, and R. Roberts, McKinsey Co. (2010).

[6] G. I. Stegeman and E. M. Wright, Opt. Quantum Electron. **22**, 95 (1990).

[7] M. Matsumoto, IEEE J. Sel. Top. Quantum Electron. **18**, 738 (2012).

[8] Z. Chai, X. Hu, F. Wang, X. Niu, J. Xie, and Q. Gong, Adv. Opt. Mater. **5**, 1600665 (2017).

[9] A. Yariv, *Quantum Electronics*, 3rd ed. (John Wiley & Sons, New York, 1989).

[10] B. E. A. Saleh and M. C. Teich, *Fundamentals of Photonics* (Wiley, 2007).

[11] V. W. S. Chan, K. L. Hall, E. Modiano, and K. A. Rauschenbach, J. Light. Technol. **16**, 2146 (1998).

[12] J. D. Jackson, *Classical Electrodynamics*, 3rd ed. (Wiley, New York, NY, 1999).

[13] R. W. Boyd, *Nonlinear Optics*, 3rd ed. (Elsevier Ltd., 2008).

[14] B. B R, S. R A, and D. A. J A, IEEE J. Quantum Electron. **26(1)**, 113 (1990).

[15] V. R. Almeida, C. A. Barrios, R. R. Panepucci, and M. Lipson, Nature **431**, 1081 (2004).

[16] K. Nozaki, A. Shinya, S. Matsuo, T. Sato, E. Kuramochi, and M. Notomi, Opt. Express **21**, 11877 (2013).

[17] W. Bogaerts, P. De Heyn, T. Van Vaerenbergh, K. De Vos, and S. Kumar, **73**, 47 (2012).

[18] M. Först, J. Bolten, M. Gottheil, H. Kurz, T. Wahlbrink, T. Plötzing, and M. Waldow, Opt. Express **16**, 7693 (2008).

[19] W. Li, B. Chen, C. Meng, W. Fang, Y. Xiao, X. Li, Z. Hu, Y. Xu, L. Tong, H. Wang, W. Liu, J. Bao, and Y. R. Shen, Nano Lett. **14**, 955 (2014).

[20] M. Silveirinha and A. Alù, URSI Gen. Assem. … (2008).

[21] N. Kinsey, C. DeVault, J. Kim, M. Ferrera, V. M. Shalaev, and A. Boltasseva, Optica **2**, 616 (2015).

[22] N. F. Mott, Rev. Mod. Phys. **40**, 677 (1968).

[23] M. Imada, A. Fujimori, and Y. Tokura, Rev. Mod. Phys. **70**, 1039 (1998).

[24] C. Kittel, *Introduction to Solid State Physics*, 7th ed. (Wiley, 1996).

[25] L. E. Noskin, A. Seidner, and D. G. Schlom, MRS Adv. (2017).

[26] T. C. Koethe, Z. Hu, M. W. Haverkort, C. Schüßler-Langeheine, F. Venturini, N. B. Brookes, O. Tjernberg, W. Reichelt, H. H. Hsieh, H. J. Lin, C. T. Chen, and L. H. Tjeng, Phys. Rev. Lett. **97**, 116402 (2006).

[27] W. Burkhardt, T. Christmann, B. K. Meyer, W. Niessner, D. Schalch, and A. Scharmann, Thin Solid Films **345**, 229 (1999).

[28] J. Du, Y. Gao, H. Luo, L. Kang, Z. Zhang, Z. Chen, and C. Cao, Sol. Energy Mater. Sol. Cells **95**, 469 (2011).

[29] Y. Gao, H. Luo, Z. Zhang, L. Kang, Z. Chen, J. Du, M. Kanehira, and C. Cao, Nano Energy **1**, 221 (2012).

[30] D. Y. Lei, K. Appavoo, F. Ligmajer, Y. Sonnefraud, R. F. Haglund, and S. A. Maier, ACS Photonics **2**, 1306 (2015).

[31] N. A. Butakov, M. W. Knight, T. Lewi, P. P. Iyer, D. Higgs, H. T. Chorsi, J. Trastoy, J. Del Valle Granda, I. Valmianski, C. Urban, Y. Kalcheim, P. Y. Wang, P. W. C. Hon, I. K. Schuller, and J. A. Schuller, ACS Photonics **5**, 4056 (2018).

[32] J. Lee, D. Lee, S. J. Cho, J. Seo, D. Liu, C. Eom, and Z. Ma, **063110**, 8 (2017).

[33] M. R. Beebe, J. M. Klopf, Y. Wang, S. Kittiwatanakul, J. Lu, S. A. Wolf, and R. A. Lukaszew, Opt. Mater. Express **7**, 213 (2017).

[34] R. S. Weis and T. K. Gaylord, Appl. Phys. A Mater. Sci. Process. **37**, 191 (1985).

[35] R. F. Haglund, S. M. Weiss, and K. Appavoo, SPIE Proc. - Quantum Sens. Nanophotonic Devices XII **9370**, 93701C (2015).

[36] R. M. Briggs, I. M. Pryce, and H. A. Atwater, Opt. Express **18**, 11192 (2010).

[37] K. J. Miller, K. A. Hallman, R. F. Haglund, and S. M. Weiss, Opt. Express **25**, 26527 (2017).

[38] A. Joushaghani, J. Jeong, S. Paradis, D. Alain, J. Stewart Aitchison, and J. K. S. Poon, Opt. Express **23**, 3657 (2015).

[39] A. Joushaghani, B. A. Kruger, S. Paradis, D. Alain, J. Stewart Aitchison, and J. K. S. Poon, Appl. Phys. Lett. **102**, (2013).

[40] P. Markov, R. E. Marvel, H. J. Conley, K. J. Miller, R. F. Haglund, and S. M. Weiss, ACS Photonics **2**, 1175 (2015).

[41] A. Joushaghani, J. Jeong, S. Paradis, D. Alain, J. Stewart Aitchison, and J. K. S. Poon, Opt. Express **23**, 3657 (2015).

[42] G. Stefanovich, A. Pergament, and D. Stefanovich, J. Phys. Condens. Matter **12**, 8837 (2000).

[43] M. Liu, H. Y. Hwang, H. Tao, A. C. Strikwerda, K. Fan, G. R. Keiser, A. J. Sternbach, K. G. West, S. Kittiwatanakul, J. Lu, S. a Wolf, F. G. Omenetto, X. Zhang, K. a Nelson, and R. D. Averitt, Nature **487**, 345 (2012).

[44] K. J. Miller, P. Markov, R. E. Marvel, R. F. Haglund, and S. M. Weiss, in (2016), p. 975203.

[45] W. R. Roach and I. Balberg, Solid State Commun. **9**, 551 (1971).

[46] E. Radue, L. Wang, S. Kittiwatanakul, J. Lu, S. A. Wolf, E. Rossi, R. A. Lukaszew, and I. Novikova, J. Opt. **92**, 1 (2015).

[47] E. Radue, L. Wang, S. Kittiwatanakul, J. Lu, S. A. Wolf, E. Rossi, R. A. Novikova, and I. Lukaszew, J. Opt. **17**, 025503 (2015).

[48] M. Hada, K. Okimura, and J. Matsuo, Appl. Phys. Lett. **99**, (2011).

[49] K. Appavoo, B. Wang, N. F. Brady, M. Seo, J. Nag, R. P. Prasankumar, D. J. Hilton, S. T. Pantelides, and R. F. Haglund, Nano Lett. **14**, 1127 (2014).

[50] T. L. Cocker, L. V. Titova, S. Fourmaux, G. Holloway, H. C. Bandulet, D. Brassard, J. C. Kieffer, M. A. El Khakani, and F. A. Hegmann, Phys. Rev. B - Condens. Matter Mater. Phys. **85**, 1 (2012).

[51] Z. Tao, T.-R. T. Han, S. D. Mahanti, P. M. Duxbury, F. Yuan, C.-Y. Ruan, K. Wang, and J. Wu, Phys. Rev. Lett. **109**, 166406 (2012).

[52] D. Wegkamp and J. Stähler, Prog. Surf. Sci. **90**, 464 (2015).

[53] V. R. Morrison, R. P. Chatelain, K. L. Tiwari, A. Hendaoui, A. Bruhács, M. Chaker, and B. J. Siwick, Science (80-.). **346**, 445 (2014).

[54] D. Wegkamp, M. Herzog, L. Xian, M. Gatti, P. Cudazzo, C. L. McGahan, R. E. Marvel, R. F. Haglund, A. Rubio, M. Wolf, and J. Stähler, Phys. Rev. Lett. **113**, 216401 (2014).

[55] S. Lysenko, A. Rúa, V. Vikhnin, F. Fernández, and H. Liu, Phys. Rev. B - Condens. Matter Mater. Phys. **76**, 1 (2007).

[56] H. Wen, L. Guo, E. Barnes, J. H. Lee, D. A. Walko, R. D. Schaller, J. A. Moyer, R. Misra, Y. Li, E. M. Dufresne, D. G. Schlom, V. Gopalan, and J. W. Freeland, Phys. Rev. B **88**, 165424 (2013).

[57] R. Rana, J. M. Klopf, J. Grenzer, H. Schneider, M. Helm, and A. Pashkin, Phys. Rev. B **99**, 041102(R) (2019).

[58] J. D. Ryckman, V. Diez-Blanco, J. Nag, R. E. R. E. Marvel, B. K. K. Choi, R. F. Haglund, S. M. S. M. Weiss, R. F. Haglund Jr., S. M. S. M. Weiss, R. F. Haglund, and S. M. S. M. Weiss, Opt. Express **20**, 13215 (2012).

[59] J. Shah, *Ultrafast Spectroscopy of Semiconductors and Semiconductor Nanostructures*, 2nd Enlarg (Springer-Verlag, New York, 1999).

[60] Hamamatsu Photonics K.K. (2008).

[61] T. P. H. Sidiropoulos, R. Röder, S. Geburt, O. Hess, S. a. Maier, C. Ronning, and R. F. Oulton, Nat. Phys. **10**, 870 (2014).

[62] J. Mendialdua, R. Casanova, and Y. Barbaux, J. Electron Spectros. Relat. Phenomena **71**, 249 (1995).

[63] Z. Weibin, W. Weidong, W. Xueming, C. Xinlu, Y. Dawei, S. Changle, P. Liping, W. Yuying, and B. Li, Surf. Interface Anal. **45**, 1206 (2013).

[64] K. Shibuya and A. Sawa, AIP Adv. **5**, (2015).

[65] S. Lysenko, N. Kumar, A. Rúa, J. Figueroa, J. Lu, and F. Fernández, Phys. Rev. B **96**, 1 (2017).

[66] B. R. King, H. C. Patel, D. A. Gulino, and B. J. Tatarchuk, Thin Solid Films **192**, 351 (1990).

[67] Rigaku, (n.d.).

[68] G. Grosso and G. P. Parravicini, *Solid State Physics* (Elsevier Ltd., 2014).

[69] W. B. Joyce and R. W. Dixon, Appl. Phys. Lett. **31**, 354 (1977).

[70] P. A. Wolff, Phys. Rev. **126**, (1962).

[71] P. A. Danilov, A. A. Ionin, S. I. Kudryashov, S. V. Makarov, A. A. Rudenko, P. N.

Saltuganov, L. V. Seleznev, V. I. Yurovskikh, D. A. Zayarny, and T. Apostolova, J. Exp. Theor. Phys. **120**, 946 (2015).

[72] G. Stefanovich, A. Pergament, and D. Stefanovich, J. Phys. Condens. Matter **12**, 8837 (2000).

[73] C. N. Berglund and H. J. Guggenheim, Phys. Rev. **185**, 1022 (1969).

[74] M. R. Otto, L. P. R. de Cotret, D. A. Valverde-Chavez, K. L. Tiwari, N. Émond, M. Chaker, D. G. Cooke, and B. J. Siwick, PNAS **116**, 450 (2019).

[75] Y. Sakai, N. Tsuda, and T. Sakata, J. Phys. Soc. Japan **54**, 1514 (1985).

[76] K. Feng, W. Streyer, S. M. Islam, J. Verma, D. Jena, D. Wasserman, and A. J. Hoffman, Appl. Phys. Lett. **107**, 081108 (2015).

[77] A. O'Hara, T. N. Nunley, A. B. Posadas, S. Zollner, and A. A. Demkov, J. Appl. Phys. **116**, (2014).

[78] T. W. Ebbesen, H. J. Lezec, H. F. Ghaemi, T. Thio, and P. A. Wolff, **391**, 667 (1998).

[79] H. Liu and P. Lalanne, Nature **452**, 728 (2008).

[80] R. GORDON, D. SINTON, K. L. KAVANAGH, and A. G. BROLO, **41**, 1049 (2008).

[81] S. A. Ramakrishna, Reports Prog. Phys. **68**, 449 (2005).

[82] H. Gao, J. K. Hyun, M. H. Lee, J. C. Yang, L. J. Lauhon, and T. W. Odom, Nano Lett. **10**, 4111 (2010).

[83] S. A. Maier, *Plasmonics: Fundamentals and Application* (Springer US, 2007).

[84] P. J. Bock, P. Cheben, J. H. Schmid, J. Lapointe, A. Delâge, S. Janz, G. C. Aers, D.-X. Xu, A. Densmore, and T. J. Hall, Opt. Express **18**, 20251 (2010).

[85] N. F. Brady, K. Appavoo, M. Seo, J. Nag, R. P. Prasankumar, R. F. Haglund, and D. J. Hilton, J. Phys. Condens. Matter **28**, 125603 (2016).

[86] Y. L. Ho, L. C. Huang, and J. J. Delaunay, Nano Lett. **16**, 3094 (2016).

[87] H. Matsui, Y. L. Ho, T. Kanki, H. Tanaka, J. J. Delaunay, and H. Tabata, Adv. Opt. Mater. **3**, 1759 (2015).

[88] a D. Rakic, A. B. Djurisic, J. M. Elazar, and M. L. Majewski, Appl. Opt. **37**, 5271 (1998).

[89] E. D. Palik, *Handbook of Optical Constants of Solids* (Academic Press, 1998).

[90] I. H. Malitson, J. Opt. Soc. Am. **55**, 1205 (1965).

[91] P. Berini, Adv. Opt. Photonics **1**, 484 (2009).

[92] P. Markov, K. Appavoo, R. F. Haglund, and S. M. Weiss, Opt. Express **23**, 6878 (2015).

[93] J. D. Ryckman, K. A. Hallman, R. E. Marvel, R. F. Haglund, and S. M. Weiss, Opt. Express **21**, 10753 (2013).

[94] D. Fu, K. Liu, T. Tao, K. Lo, C. Cheng, B. Liu, R. Zhang, H. A. Bechtel, and J. Wu, J. Appl. Phys. **113**, 1 (2013).

[95] K. T. Jacob, C. Shekhar, and M. Vinay, 4854 (2010).

[96] M. Born and E. Wolf, *Principles of Optics*, 5th ed. (1975).

Appendix A: Material Parameters

VO_2 Parameters

Parameter	Value	Source
m_e^*	$65m_0$	Extracted by fitting theoretical band structure of Fu et al. [94]
m_h^*	$65m_0$	Extracted by fitting theoretical band structure of Fu et al. [94]
R_{766nm}	21.0%	Measured using optical spectrometer
T_{766nm}	49.4%	Measured using optical spectrometer
ρ_{VO2}	4.34 g/cm^3	Obtained from Jacob et al. [42]
C_p	0.69 J/gK	Obtained from Jacob et al. [42]

NbO_2 Parameters

Parameter	Value	Source
m_e^*	$8.8m_0$	Extracted by fitting theoretical band structure of O'hara et al. [77]
m_h^*	$5.7m_0$	Extracted by fitting theoretical band structure of O'hara et al. [77]
R_{766nm}	27.6%	Measured using optical spectrometer
T_{766nm}	32.3%	Measured using optical spectrometer
M_u	124.9 g/mol	
ρ_{NbO2}	6.10 g/cm^3	Measured with XRR
C_p	57.35 J/molK	Obtained from Jacob et al. [95]

Appendix B: Transfer Matrix Calculations

In order to calculate the theoretical modulation in the transmittance and reflectance of the NbO_2 thin-film resulting from the photo-excited carrier induced changes in the refractive index of the NbO_2, the transfer matrix method was used.

The transmittance of a multi-layer thin-film structure can be calculated analytically using a technique known as the transfer matrix method [96]. In this method, each layer and interface of a multilayer structure is given a characteristic matrix.

$$M_{layer} = \begin{bmatrix} e^{-in_1 k_0 cos\theta_1 d} & 0 \\ 0 & e^{in_1 k_0 cos\theta_1 d} \end{bmatrix} \quad \text{and} \quad M_{interface} = \frac{1}{t_{12}} \begin{bmatrix} 1 & r_{12} \\ r_{12} & 1 \end{bmatrix}$$

where n_1 is the refractive index of layer 1, k_0 is the free space propagation constant, and θ_1 is the angle of light propagation in layer 1 (relative to the normal), d is the thickness of layer 1, and t_{12} and r_{12} are the Fresnel transmission and reflection coefficients for an interface between layers 1 and 2. The characteristic matrix for a multilayer is calculated by multiplying the matrices of all the layers in the multilayer in reverse order. For example, the characteristic matrix of a thin-film (such as the NbO_2 layer in this paper) is

$$M_{tot} = \frac{1}{t_{12}} \begin{bmatrix} 1 & r_{12} \\ r_{12} & 1 \end{bmatrix} \begin{bmatrix} e^{-in_2 k_0 cos\theta_2 d} & 0 \\ 0 & e^{in_2 k_0 cos\theta_2 d} \end{bmatrix} \frac{1}{t_{23}} \begin{bmatrix} 1 & r_{23} \\ r_{23} & 1 \end{bmatrix}.$$

Here layers 1, 2 and 3 are the ambient material, thin-film and substrate respectively. The final characteristic matrix is a 2x2 matrix,

$$M_{tot} = \begin{bmatrix} M_{1,1} & M_{1,2} \\ M_{2,1} & M_{2,2} \end{bmatrix}$$

The transmittance and reflectance of the multilayer described by the characteristic matrix can be calculated according to

$$T = \frac{n_{final} cos\theta_{final}}{n_{initial} cos\theta_{initial}} \left| \frac{1}{M_{1,1}} \right|^2 \quad \text{and} \quad R = \left| \frac{M_{2,1}}{M_{1,1}} \right|^2$$

The initial transmittance and reflectance of the NbO_2 thin-film was first calculated using this method for normal incidence with the refractive index of NbO_2 measured using ellipsometry being used. The transmittance and reflectance were then recalculated using after shifting the refractive index of NbO_2 by the Δn_{net} shown in FIG 4a. The differential

transmittance/reflectance was simply calculated by dividing the change in transmittance/reflectance by the initial transmittance/reflectance.